

④

FILE COPY

AD-A211 256

AFGL-TR-89-0076

Direct Statistical Thermal
Wind Estimation Procedure

Charles L. Medler

Analytic Sciences Corporation
55 Walkers Brook Drive
Reading, MA 01867

10 March 1989


Final Report
Period Covered 17 Sep 87 - 16 Sep 88


Approved for public release; distribution unlimited

DTIC
ELECTE
AUG 14 1989
S a D

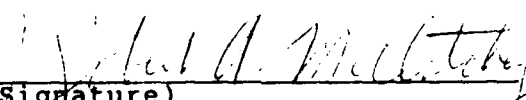
AIR FORCE GEOPHYSICS LABORATORY
AIR FORCE SYSTEMS COMMAND
UNITED STATES AIR FORCE
HANSOM AIR FORCE BASE, MASSACHUSETTS 01731-5000

"This technical report has been reviewed and is approved for publication"


(Signature)
THOMAS J. KLEESPIES
Contract Manager


(Signature)
KENNETH R. HARDY
Branch Chief, Satellite Meteorology

FOR THE COMMANDER


(Signature)
Robert A. McClatchey
Division Director, Atmospheric Sciences

This report has been reviewed by the ESD Public Affairs Office (PA) and is releasable to the National Technical Information Service (NTIS).

Qualified requestors may obtain additional copies from the Defense Technical Information Center. All others should apply to the National Technical Information Service.

If your address has changed, or if you wish to be removed from the mailing list, or if the addressee is no longer employed by your organization, please notify AFGL/DAA, Hanscom AFB, MA 01731. This will assist us in maintaining a current mailing list.

Do not return copies of this report unless contractual obligations or notices on a specific document requires that it be returned.

Unclassified

SECURITY CLASSIFICATION OF THIS PAGE

REPORT DOCUMENTATION PAGE

1a REPORT SECURITY CLASSIFICATION Unclassified			1b RESTRICTIVE MARKINGS		
2a SECURITY CLASSIFICATION AUTHORITY			3 DISTRIBUTION / AVAILABILITY OF REPORT approved for public release; distribution unlimited		
2b DECLASSIFICATION / DOWNGRADING SCHEDULE					
4 PERFORMING ORGANIZATION REPORT NUMBER(S) TR-5547-1			5 MONITORING ORGANIZATION REPORT NUMBER(S) AFGL-TR-89-0076		
6a NAME OF PERFORMING ORGANIZATION Analytic Sciences Corp.		6b OFFICE SYMBOL (If applicable)	7a NAME OF MONITORING ORGANIZATION Air Force Geophysics Laboratory		
6c ADDRESS (City, State, and ZIP Code) 55 Walkers Brook Drive Reading, MA 01867			7b ADDRESS (City, State, and ZIP Code) Hanscom AFB Massachusetts 01731-5000		
8a NAME OF FUNDING / SPONSORING ORGANIZATION		8b OFFICE SYMBOL (If applicable)	9 PROCUREMENT INSTRUMENT IDENTIFICATION NUMBER F19628-87-C-0248		
8c ADDRESS (City, State, and ZIP Code)			10 SOURCE OF FUNDING NUMBERS		
			PROGRAM ELEMENT NO 61101F	PROJECT NO ILIR	TASK NO 7K
					WORK UNIT ACCESSION NO AA
11 TITLE (Include Security Classification) Direct Statistical Thermal Wind Estimation Procedure					
12 PERSONAL AUTHOR(S) Charles L. Medler					
13a TYPE OF REPORT Final Report		13b TIME COVERED FROM 9/17/87 to 9/16/88		14 DATE OF REPORT (Year, Month, Day) March 10, 1989	
15 PAGE COUNT 134					
16 SUPPLEMENTARY NOTATION					
17 COSATI CODES			18 SUBJECT TERMS (Continue on reverse if necessary and identify by block number)		
FIELD	GROUP	SUB-GROUP	Thermal Wind, Wind Profiles, Radiance Data Processing, Remote Sensing		
19 ABSTRACT (Continue on reverse if necessary and identify by block number) A procedure to estimate thermal wind profiles directly from multispectral satellite radiance data has been specified and implemented. A previous interim report which presented the theoretical formulation and statistical models for a baseline algorithm is included as Appendix G of this Final Report. Sensitivity of the estimates and numerical evaluations of the baseline algorithm using NOAA-7 radiance data are the major topics of this Final Report, serving to demonstrate the procedure developed. Thermal winds derived independently from NMC temperature analyses provide a benchmark for verification. Results using a method from which this work was motivated are included for comparison.					
20 DISTRIBUTION / AVAILABILITY OF ABSTRACT <input type="checkbox"/> UNCLASSIFIED/UNLIMITED <input checked="" type="checkbox"/> SAME AS RPT <input type="checkbox"/> DTIC USERS			21 ABSTRACT SECURITY CLASSIFICATION Unclassified		
22a NAME OF RESPONSIBLE INDIVIDUAL Thomas Kleespies			22b TELEPHONE (Include Area Code) (617) 377-3136		22c OFFICE SYMBOL AFGL/LYS

FOREWORD

The attractive prospect of estimating wind profiles directly from satellite radiance data is motivated by three factors:

- the abundance of satellite data over areas such as the oceans which lack conventional data sources
- the cost-effective advantages of obtaining representative winds in data-sparse regions without additional instrumentation, and
- the avoidance of errors associated with an indirect approach based on collections of temperature profiles obtained from satellite radiance data by solving the inversion problem.

Several attempts to develop a direct approach have been discussed in the open literature but have yielded disappointing results. The most important of these efforts are reviewed in the proposal which led to this project (Ref. 2) which is funded by The Satellite Meteorology Branch of the Air Force Geophysics Laboratory. As discussed in Appendix G, an interim technical report, this project extends previous work by minimizing a specified error criterion to obtain statistically optimal thermal wind estimates. The framework established for incorporating statistical error models of relevant data sources and algorithm components is also a significant contribution of the project.

Accession For	
NTIS GRA&I	<input checked="" type="checkbox"/>
DTIC TAB	<input type="checkbox"/>
Unannounced	<input type="checkbox"/>
Justification	
By	
Distribution/	
Availability Codes	
Dist	Avail and/or Special
A-1	

ACKNOWLEDGMENTS

The research described in this report was supported by several members of TASC's Atmospheric Sciences Department. Steven M. Koenig, Barbara A. Chance and Steven R. Finch all participated in data pre-processing and interpretation and Mr. Finch made significant contributions to the algorithm development. Kenneth B. MacNichol provided project leadership, developed the baseline software and, assisted by Mr. Koenig, did the initial data processing.

TABLE OF CONTENTS

	Page
FOREWORD	iii
ACKNOWLEDGMENTS	iv
LIST OF FIGURES	vi
LIST OF TABLES	viii
EXECUTIVE SUMMARY	ES-1
1. INTRODUCTION	1-1
2. RESULTS	2-1
2.1 Radiance Gradient Vectors	2-1
2.2 Optimal Estimation Method	2-6
2.2.1 Optimal Estimation Algorithm Interpretation	2-6
2.2.2 Temperature Data and Approximations	2-7
2.2.3 Baseline Optimal Estimation Results	2-10
2.3 Ohring's Method	2-15
2.4 Sensitivity Evaluations	2-22
2.4.1 Perturbations of Data and Parameters	2-23
2.4.2 Analytic Sensitivity Results	2-35
3. SUMMARY AND RECOMMENDATIONS	3-1
3.1 Conclusions from the Demonstration	3-1
3.2 Recommendations	3-3
APPENDIX A RADIANCE DATA	A-1
APPENDIX B RADIANCE GRADIENT ESTIMATES	B-1
APPENDIX C KERNEL FUNCTIONS	C-1
APPENDIX D RADIANCE GRADIENTS FROM PLANAR FITS	D-1
APPENDIX E PROOF OF ALGORITHM VALIDITY	E-1
APPENDIX F SENSITIVITY EQUATIONS	F-1
APPENDIX G THE INTERIM REPORT	G-1
REFERENCES	R-1

LIST OF FIGURES

Figure	Page
ES-1 Overview of Optimal Thermal Wind Profile Estimation	ES-2
ES-2 Thermal Wind Profile Estimates by the Optimal Estimation Algorithm	ES-3
2.1-1 Visible Channel Intensity Contours and Data Region	2-1
2.1-2 Geographical Location of Data Region	2-2
2.1-3 Radiance Gradient Vectors Based on Planar Fits	2-4
2.2-1 Gibraltar Temperature Profile	2-8
2.2-2 NMC Temperature Analysis (850 mb) (deg C)	2-9
2.2-3 Temperature Gradient Profile	2-11
2.2-4 Approximate Temperature Gradient Profiles	2-11
2.3-1 Weighting Function Approximations on 850 mb to 700 mb	2-18
2.3-2 Weighting Function Approximations on 700 mb to 500 mb	2-18
2.3-3 Weighting Function Approximations on 500 mb to 300 mb	2-19
2.3-4 Weighting Function Approximations on 300 mb to 200 mb	2-19
2.3-5 Weighting Function Approximations on 200 mb to 100 mb	2-20
2.4-1 Nominal and Perturbed Meridional Temperature Gradient Profiles	2-24
2.4-2 Sensitivity of Thermal Wind Estimates to a 850 mb Temperature Gradient Additive Perturbation	2-26
2.4-3 Sensitivity of Thermal Wind Estimates to a 500 mb Temperature Gradient Additive Perturbation	2-27
2.4-4 Sensitivity of Thermal Wind Estimates to a 850 mb Temperature Gradient Multiplicative Perturbation	2-28
2.4-5 Sensitivity of Thermal Wind Estimates to Radiance Gradient Error Variance	2-30
2.4-6 Average Sensitivity of the Kernel Functions to the Temperature Profile	2-32
2.4-7 Sensitivity of Thermal Wind Estimates to the Kernel Functions	2-33
A-1 Radiance Data: Channel 3-North	A-2
A-2 Radiance Data: Channel 3-South	A-2
A-3 Radiance Data: Channel 4-North	A-3

LIST OF FIGURES (Continued)

Figure		Page
A-4	Radiance Data: Channel 4-South	A-3
A-5	Radiance Data: Channel 5-North	A-4
A-6	Radiance Data: Channel 5-South	A-4
A-7	Radiance Data: Channel 6-North	A-5
A-8	Radiance Data: Channel 6-South	A-5
A-9	Radiance Data: Channel 15-North	A-6
A-10	Radiance Data: Channel 15-South	A-6
A-11	Radiance Data: Channel 16-North	A-7
A-12	Radiance Data: Channel 16-South	A-7
B-1	Radiance Gradient Vectors: Channel 3	B-1
B-2	Radiance Gradient Vectors: Channel 4	B-2
B-3	Radiance Gradient Vectors: Channel 5	B-2
B-4	Radiance Gradient Vectors: Channel 6	B-3
B-5	Radiance Gradient Vectors: Channel 15	B-3
B-6	Radiance Gradient Vectors: Channel 16	B-4
C-1	Kernel Functions: Channels 3, 4, 5, 6	C-1
C-2	Kernel Functions: Channels 15, 16	C-2

LIST OF TABLES

Table	Page
2.1-1 Summary of HIRS 2 Data used in the Demonstration	2-3
2.1-2 Estimated Radiance Gradient Variability with Location	2-4
2.1-3 Estimated Radiance Gradients at Center of Data Collection Region (7 x 7 Planar Fit)	2-5
2.2-1 Temperature Gradients Based on a 5 x 5 Subgrid (deg C/m)	2-10
2.2-2 Results of the Baseline Case	2-12
2.2-3 Initial Thermal Wind Estimates	2-13
2.2-4 Final Thermal Wind Estimates	2-14
2.2-5 Thermal East Wind Profile Estimate Dependence on Channel Selection	2-15
2.3-1 Ohring's Method Results: East Component of Thermal Wind	2-17
2.3-2 Optimal Coefficients from Ohring's Method (East Component)	2-20
2.3-3 Optimal Ohring's Method Contributions (East Component)	2-21
2.3-4 Comparison of Optimal Estimation and Ohring's Method Estimates (Channels 3, 4, and 15)	2-21
2.4-1 Fractional Changes in Layer Estimates Due to Additive Perturbations	2-25
2.4-2 Sensitivities with Respect to Radiance Gradient Components	2-29
2.4-3 Sensitivity of Kernel Functions to Temperature	2-31
2.4-4 Fractional Changes in Thermal Wind Estimates (All Parameters Perturbed)	2-34
2.4-5 Kernel Function Sensitivity Matrix: Optimal Estimate of East Thermal Wind Component	2-35
2.4-6 Kernel Function Sensitivity Matrix: Ohring Estimate of East Thermal Wind Component	2-36

EXECUTIVE SUMMARY

This report summarizes a research project conducted by TASC during GFY88, with approximately one person-year level of effort. The central idea behind the project was to use statistical models of error sources and an optimal estimation theory approach to estimate *thermal wind profiles* directly from multi-spectral satellite sounder radiance data. (We refer to the procedure as the optimal estimation algorithm in this report.) Thermal wind profiles contain estimates of the vector difference between the geostrophic wind at each of several altitudes and that at a single reference altitude. The reference altitude would typically be at the lower end of the profile, e.g., that of a surface wind measurement by a ship-based instrument. The project was motivated by a need for improved wind measurements in data sparse regions such as cloud-free areas over the ocean. If successfully implemented, the resulting algorithm would provide a complement to cloud-drift wind estimation procedures. Figure ES-1 contains a schematic representation of how an operational optimal estimation algorithm might function.

Section 2 of this Final Report demonstrates clearly that the algorithm generates reasonable thermal wind profile estimates using only approximate first-guess information typical of what would exist in an open ocean region. Figure ES-2 presents results for two initial data conditions along with rawinsonde-measured values of *total* wind shear near the estimate location. The two initial data conditions are: 1) using a temperature derivative profile derived from an analysis field based on rawinsonde data and 2) using a crude approximation to the analyzed profile typical of what a forecast or analysis field might provide at an open-ocean location. For each case, initial profiles (dashed curves) and final estimates (solid curves) are shown. The important point demonstrated by this figure is that even though the initial data provided much different first-guess wind profiles (calculated from the temperature derivative profiles via the thermal wind equation), the algorithm produced *very similar* final estimates from the satellite radiance data.

The total shear data plotted in Fig. ES-2 are rawinsonde-measured east wind differences between each pressure level and 850 mb. Although the shape of the total shear profile is similar to that of the other curves, it is clear that a significant non-geostrophic wind component existed in the region. This is clearly a limitation of any wind estimation approach relying solely on radiance measurements.

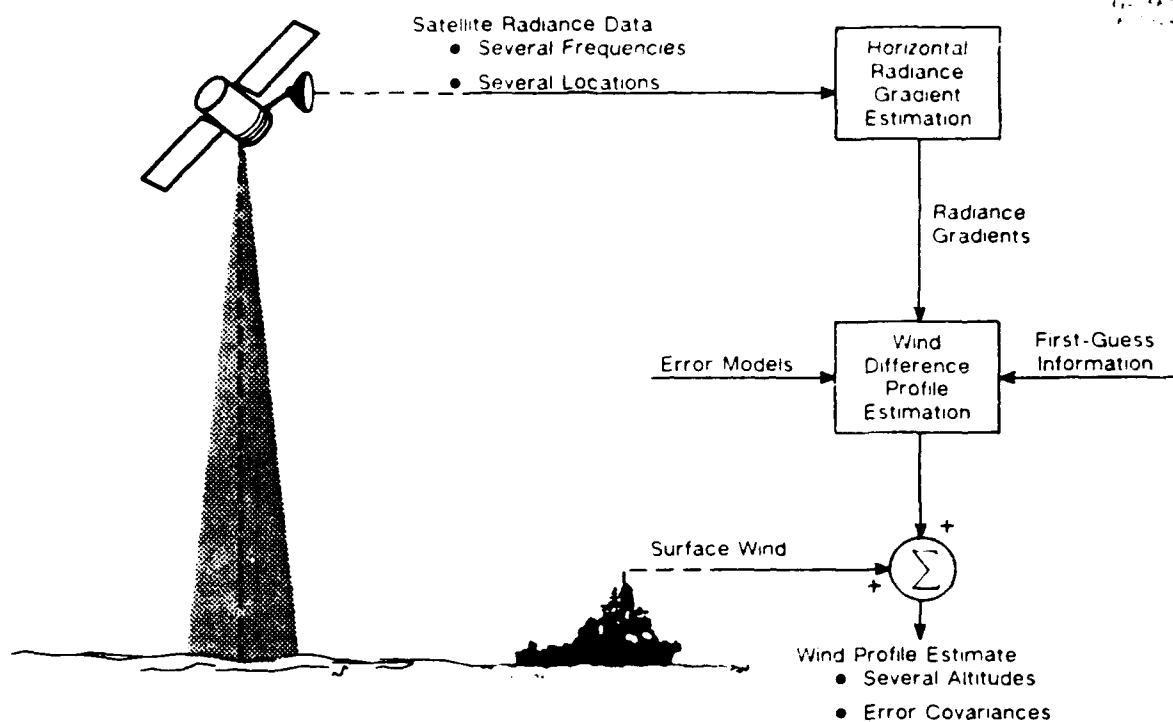


Figure ES-1 Overview of Optimal Thermal Wind Profile Estimation

Analyses described in this report show that significant data sensitivities *may* exist which could make superiority of the optimal estimation approach over alternate approaches unclear. For example, a primary alternate approach is to develop (i.e., estimate) a 3-D temperature field from a grid of satellite soundings by "temperature inversion" applied to each sounding. Then the thermal wind equation can be used to estimate the thermal wind profile from the layer-averaged, horizontal gradients of the temperature field. The computational burden of this *indirect* approach is significantly larger than that of *direct* optimal estimation, due primarily to the requirement for N^2 temperature inversions (for an $N \times N$ grid of radiance data), and is clearly susceptible to inversion errors through the numerical derivatives required to define horizontal temperature gradients.

However, the optimal estimation approach also requires *gradient* data, in this case the horizontal gradients of the radiances at each sounder wavelength. Experience with the sounder data used in the demonstration showed that these gradient estimates can be more sensitive to the size and location of the data grid than is predicted by error models derived from straight-

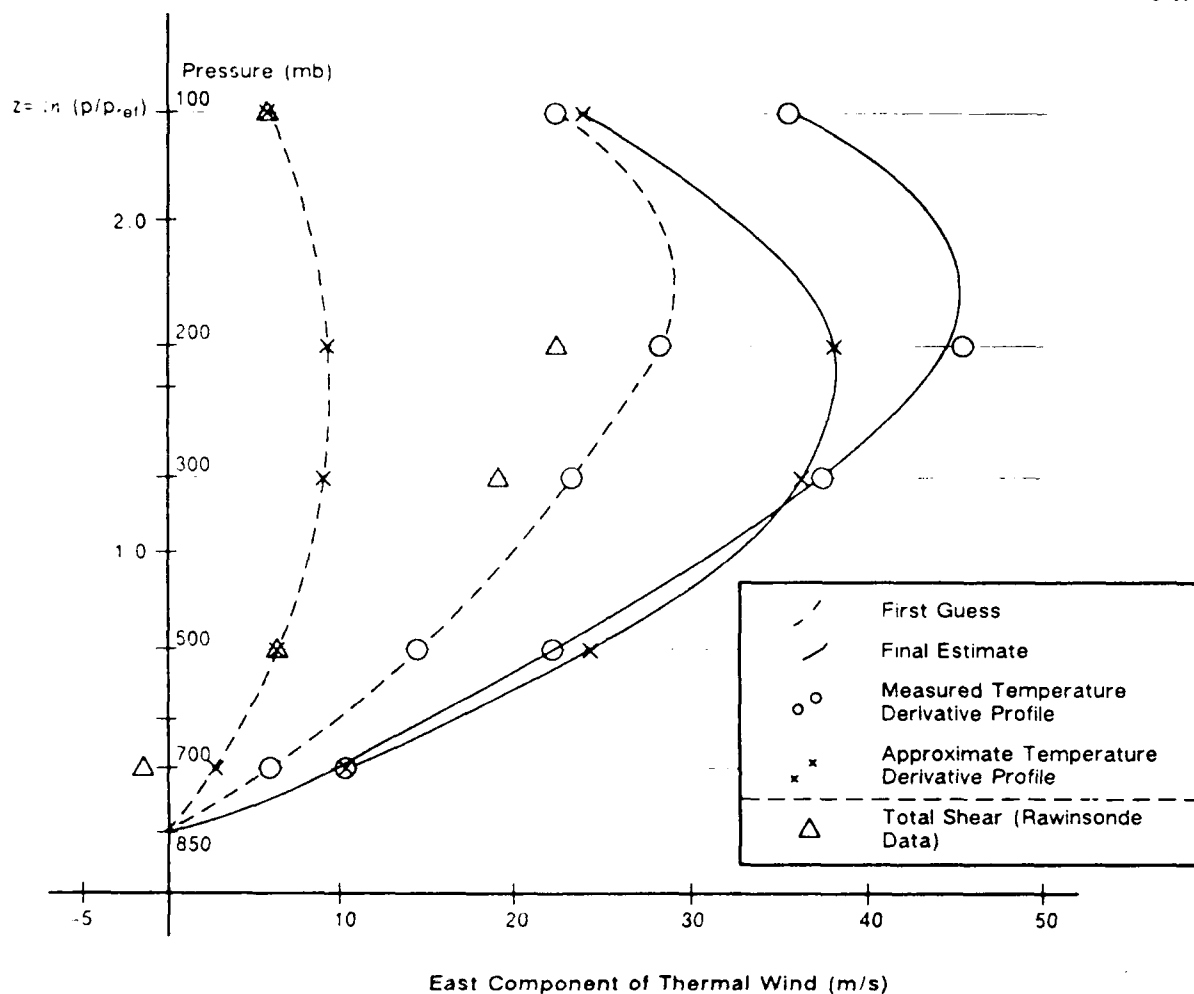


Figure ES-2 Thermal Wind Profile Estimates by the Optimal Estimation Algorithm

forward radiance data models. Recommendations in Section 3.2 focus on examining further, and reducing sensitivity to, the data variability through additional error model development. If these reductions in sensitivity are achieved, then the optimal estimation algorithm will provide a superior approach to thermal wind profile estimation relative to both the indirect approach described above and to alternate direct approaches discussed in Refs. 1 and 2.

1.

INTRODUCTION

This Final Report of TASC's Wind Profile Estimation project provides a summary of theoretical and numerical results obtained since delivery of the Interim Report (the complete interim report is included in this volume as Appendix G). At an interim project review meeting held at AFGL in April 1988, much discussion focused on the importance of determining the sensitivity of estimates to various model elements. Accordingly, project emphasis was shifted from model development to sensitivity analysis to identify those model components most strongly influencing estimation accuracy. In this way, future efforts can focus on the dominant error contributors.

Most activity since the Interim Report and meeting has been in three areas: evaluating the new wind profile estimation algorithm using the sample data set; conducting sensitivity analyses of the algorithms; and comparing the new algorithm with Ohring's method (Ref. 1), both as to implementation and numerical properties and to parameter sensitivity. Results in all of these areas are contained in this technical report.

Section 2 of the report contains four subsections which present the most important results of the project. The first subsection describes calculation of radiance gradient vectors from the sample data set. Issues of gradient variability with calculation grid size and location are described in detail (see also Appendices A, B, and D). Results related directly to the new optimal estimation algorithm are presented in the second subsection of Chapter 2 and Appendices C and E. These include an interesting and important theoretical result which shows that the algorithm, as implemented, *scales* the first-guess wind profile so as to best fit the radiance field data. Numerical results (i.e., thermal wind profile estimates) resulting from several initial temperature gradient profile assumptions are presented in this subsection. The third subsection presents results of applying Ohring's method (Ref. 1) to the same data set. Finally, the numerous sensitivity results are collected in the fourth subsection of Chapter 2 and Appendix F.

Delivery of this report constitutes completion of research efforts for this program. A summary of the conclusions which can be drawn is contained in Chapter 3. While all of the tasks outlined in the contract Statement of Work have been completed, additional effort will be required to fully implement a temperature gradient profile error model for the algorithm. That

effort and other tasks leading toward an operational algorithm are discussed briefly in the final subsection. Those tasks should lead to a practical, operational algorithm for producing thermal wind profiles directly from satellite radiance data.

2.

RESULTS

2.1 RADIANCE GRADIENT VECTORS

High Resolution Infrared Radiation Sounder 2 (HIRS 2) data selected for analysis were from the 11 x 11 grid shown in the box in Fig. 2.1-1. Contour lines in the figure are radiance intensities for the visible channel (channel 20); the box is located in a region of relatively low intensity from this channel, indicating a likely cloud-free area. (This is consistent with AVHRR

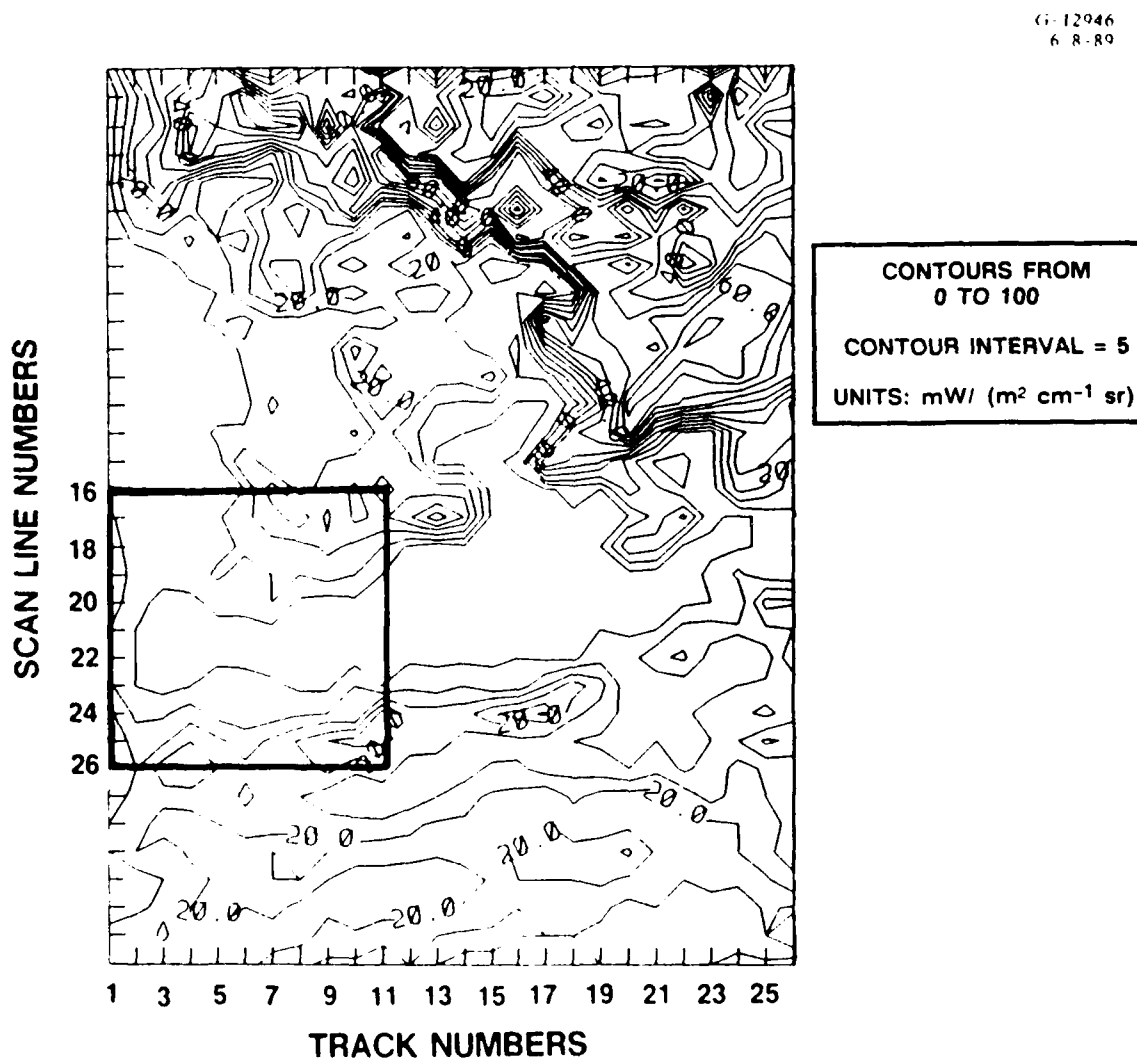


Figure 2.1-1 Visible Channel Intensity Contours and Data Region

images of the region.) Figure 2.1-2 shows the grid location within a geopolitical map of the western Mediterranean region.

In Appendix A, plots of the data from the six channels used in this demonstration are presented. Table 2.1-1 identifies the channels and their center wavelengths. There are two plots in Appendix A for each channel, each containing radiance values along six scan lines (the center of the 11 scan lines is in both plots). Scan lines and track axis distances are identified by local track-scan coordinates (in km) in which (0, 0) is at the northwest corner of the region and (400, 400) at the southeast corner. (Note that the track-scan axes are rotated at $\psi' = 20^\circ$ relative to north-east coordinates.)

Estimates of the radiance gradients for all channels were calculated from local planar fits to the data surface within the region of interest. Appendix D presents details and an error

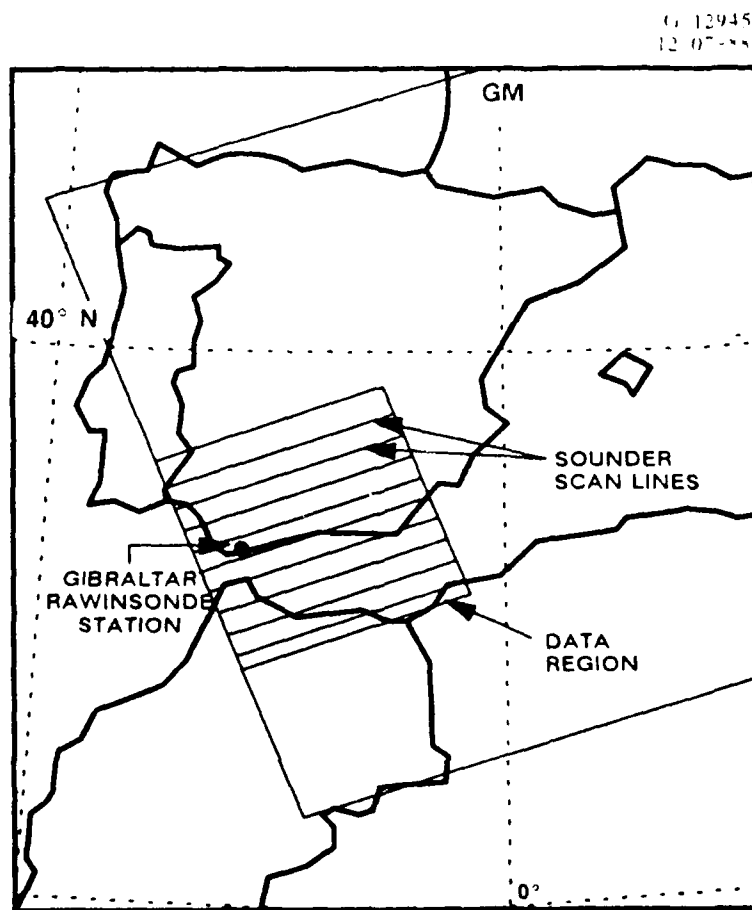


Figure 2.1-2 Geographical Location of Data Region

Table 2.1-1 Summary of HIRS/2 Data used in the Demonstration

HIRS/2 CHANNEL	WAVENUMBER (cm ⁻¹)	CENTRAL WAVELENGTH (μm)	PEAK LEVEL (mb)	ERROR Std.Dev. (mW/(m ² cm ⁻¹ sr))	NOTES
3	691	14.50	100	0.50	15-μm band
4	764	14.20	400	0.31	
5	716	14.00	600	0.21	
6	732	13.70	800	0.24	
15	2249	4.46	700	0.004	4.3-μm band
16	2276	4.40	400	0.002	
20	14367	6.70	(window)	N/A	visible channel (det.)

model for the gradient estimation procedure. Gradient estimates depend critically on the region over which the planar fit is made. Region selection was based on observed variability of the estimated gradients with region size and location.

Figure 2.1-3 contains the radiance gradient vectors computed at the grid center-point using 5 grid sizes for channels 3 and 15. Clearly the apparent slope at the center depends very much on the scale over which the slope is evaluated. Examination of vector plots similar to Fig. 2.1-3 for all six channels reveals the following:

- Using the 3 x 3 grid yields gradients much different than those from the 5 x 5 and larger grids
- Using 5 x 5 and 7 x 7 grids yields similar gradients
- Using 9 x 9 and 11 x 11 grid yields similar gradients
- The 9 x 9 gradients are usually quite different than the 7 x 7 gradients.

These observations indicate that the 9 x 9 (and 11 x 11) grids centered at the center-point of the data region contain data influenced by clouds. Presence of those clouds was also indicated by the relatively higher channel 20 returns near the southeast and northeast corners of the data region (see Fig. 2.1-1).

To quantify the variability of the radiance gradients with position of a 7 x 7 calculation grid, mean values and standard deviations for each channel as the 7 x 7 grid is moved over the 25 possible locations within the 11 x 11 data region are shown in Table 2.1-2, along with the

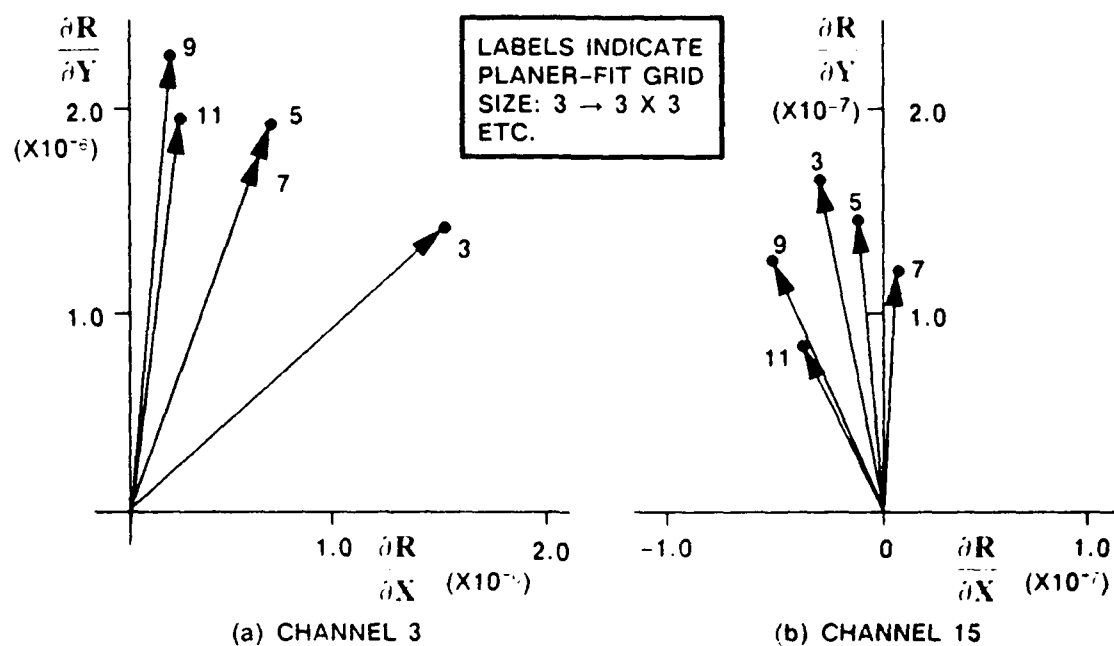


Figure 2.1-3 Radiance Gradient Vectors Based on Planar Fits

Table 2.1-2 Estimated Radiance Gradient Variability with Location⁽¹⁾

HIRS/2 CHANNEL	$\partial R/\partial x$		$\partial R/\partial y$		MODEL Std.Dev.	MULTIPLIER
	Mean	Std.Dev.	Mean	Std.Dev.		
3	0.46	0.86	2.0	3.0	2.21	} 10 ⁻⁶
4	-5.3	8.9	7.0	12.4	1.37	
5	-12.6	21.1	15.3	28.8	0.93	
6	-19.5	32.4	24.4	75.4	1.06	
15	-2.3	7.9	10.7	20.0	1.78	} 10 ⁻⁸
16	-1.1	1.8	0.3	1.4	0.88	

(1) Units are (mW/m) / (m² cm⁻¹ sr)

corresponding model-based standard error for the gradient component estimates. Sample standard deviations in Table 2.1-2 indicate that there is *significant* variability for channels 4, 5, 6 and 15 as the center-point of the 7 x 7 array is moved about the data region. Some of that variability is certainly due to the cloud effects already noted near the northeast and southeast corners of the region. The sample standard deviations are substantially larger than the model-based standard deviations suggesting that presence of the clouds causes non-negligible "model-error" in the planar fit approach to radiance gradient estimations (see the discussion in Appendix D.2).

After some experimentation, and consistent with the idea of using as large an area as possible on which to base the gradients (which are used by the synoptic-scale thermal wind equation), it was decided to use gradients computed using 7 x 7 grids. Unless stated otherwise, all estimation results presented in the rest of this section are based on the radiance gradients estimated at the center of the 11 x 11 data region using a 7 x 7 region for the planar fit. These gradients are tabulated for all six channels in Table 2.1-3 along with the standard deviation of the estimation error for each channel based on the error model presented in Appendix D (see Eq. D.2-8).

Appendix B contains plots showing the normalized gradient vectors based on 7 x 7 planar fits centered at each of 25 grid points for each of the six channels. Although there is still some variability in the gradient direction among the computed values, they do not vary wildly from one grid point to another.

Table 2.1-3 Estimated Radiance Gradients at Center of Data Collection Region (7 x 7 Planar Fit)⁽¹⁾

HIRS/2 CHANNEL	RADIANCE GRADIENT		MODEL Std.Dev.	MULTIPLIER
	ZONAL (EAST)	MERIDIONAL (NORTH)		
3	0.69	1.79	2.21	} 10^{-6}
4	-4.25	5.74	1.37	
5	-9.81	13.8	0.93	
6	-14.3	24.3	1.06	
15	0.67	12.1	1.78	} 10^{-8}
16	-1.01	-0.03	0.88	

(1) Units are (mW/m) / (m² cm⁻¹ sr)

2.2 OPTIMAL ESTIMATION METHOD

2.2.1 Optimal Estimation Algorithm Interpretation

Although no fundamentally new equations have been developed which require modification to the description of the optimal estimation algorithm found in Section 3 of the Interim Report (Appendix G), implementation of the algorithm has led to additional insight regarding its interpretation.

Consider estimation of the east component of the thermal wind shear (relative to a fixed lowest level, z_1) at each of n levels:

$$\underline{u} = \begin{pmatrix} u(z_1) \\ \vdots \\ u(z_n) \end{pmatrix} \quad (2.2-1)$$

(The north component can be treated in a similar fashion.) As shown in Appendix G, this vector of estimates can be computed using

$$\underline{u} = -(R/f) \underline{C} \underline{g} \quad (2.2-2)$$

where \underline{g} is a vector of partial derivatives of the radiances with respect to the y coordinate and R and f are the gas and Coriolis constants respectively. The optimal set of weighting constants is

$$\underline{C} = \underline{a} \underline{\theta}^T \underline{P}^{-1} \quad (2.2-3)$$

where

$$\underline{P} = \underline{\Gamma} + \underline{\theta} \underline{\theta}^T \quad (2.2-4)$$

$$\underline{\theta} = \int_0^{z_1} \underline{K}_z(\zeta) \frac{\partial T}{\partial y}(\zeta) d\zeta \quad (2.2-5)$$

and

$$a_i = \int_{z_i}^{z_1} \frac{\partial T}{\partial y}(\zeta) d\zeta, \quad i = 1, \dots, n \quad (2.2-6)$$

In Eq. 2.2-5, $z = \ln(p_{ref}/P)$ where p is the pressure level and p_{ref} is an arbitrary reference pressure. z_T is the z value at the (approximate) top of the atmosphere (z_T corresponded to the

10 mb level in all computations) and $K(\zeta)$ is the vector of kernel functions defined in Appendix G.

By rearranging the factors in the optimal estimator, Eq. 2.2-2, the vector of estimates can be written:

$$\underline{u} = (g^T P^{-1} \theta) (- (R/f) \underline{a}) \quad (2.2-7)$$

But the second factor is the estimate one would compute directly from the assumed temperature gradient profile using the thermal wind equation.

$$\underline{u}^0 = - (R/f) \underline{a} \quad (2.2-8)$$

So, the optimal wind profile estimate can be written

$$\underline{u} = d \underline{u}^0 \quad (2.2-9)$$

where d is the scalar constant found in the first factor of Eq. 2.2-7 which *does not depend* on the levels at which components of \underline{u} are defined.

Now, examination of Eq. 2.2-9 shows clearly that the optimal estimate, *based on all of the satellite radiance data*, is simply a scaled version of the initial thermal wind estimate. As will be brought out in the discussion of results, the assumed temperature gradient profile establishes the *shape* of the vertical profile; then the optimal estimation procedure uses the radiance gradient data to *scale* that profile (by d) so as to best explain those observed gradients.

Equation 2.2-2 is based on the error model for the temperature gradient estimates but not on the error in the assumed temperature gradient profile. Therefore the above interpretation does not establish an absolute limit on the usefulness of the satellite data for this application. Once a temperature gradient profile error model has been incorporated, provided that those errors (i.e., the variances) change with altitude, some reshaping of the thermal wind-derived profile can be expected.

2.2.2 Temperature Data and Approximations

The optimal estimation algorithm, Eq. 2.2-2, is based on assumed, measured or estimated temperature and temperature gradient profiles. The Gibraltar sounding taken one hour before the satellite radiance measurements were acquired was used for this demonstration.

(Procedures which could be used in an operational implementation are discussed briefly in Section 3.) The Interim Report, Appendix G, described the satellite radiance data set, the rawinsonde data, and the synoptic situation on which this demonstration is based in some detail. Figure 2.2-1 contains the temperature profile generated from the rawinsonde sounding; the Planck functions used in calculating the kernel functions were computed using this profile. Plots of the kernel functions for each channel are contained in Appendix C. Those profiles, and several others shown in this report, are plotted against the z variable defined in the previous subsection with p_{ref} chosen (arbitrarily) to be 1013 mb.

The areal coverage of a temperature analysis on six isobaric surfaces which was used to compute temperature gradients is illustrated in Fig. 2.2-2. The figure contains the 850 mb NMC

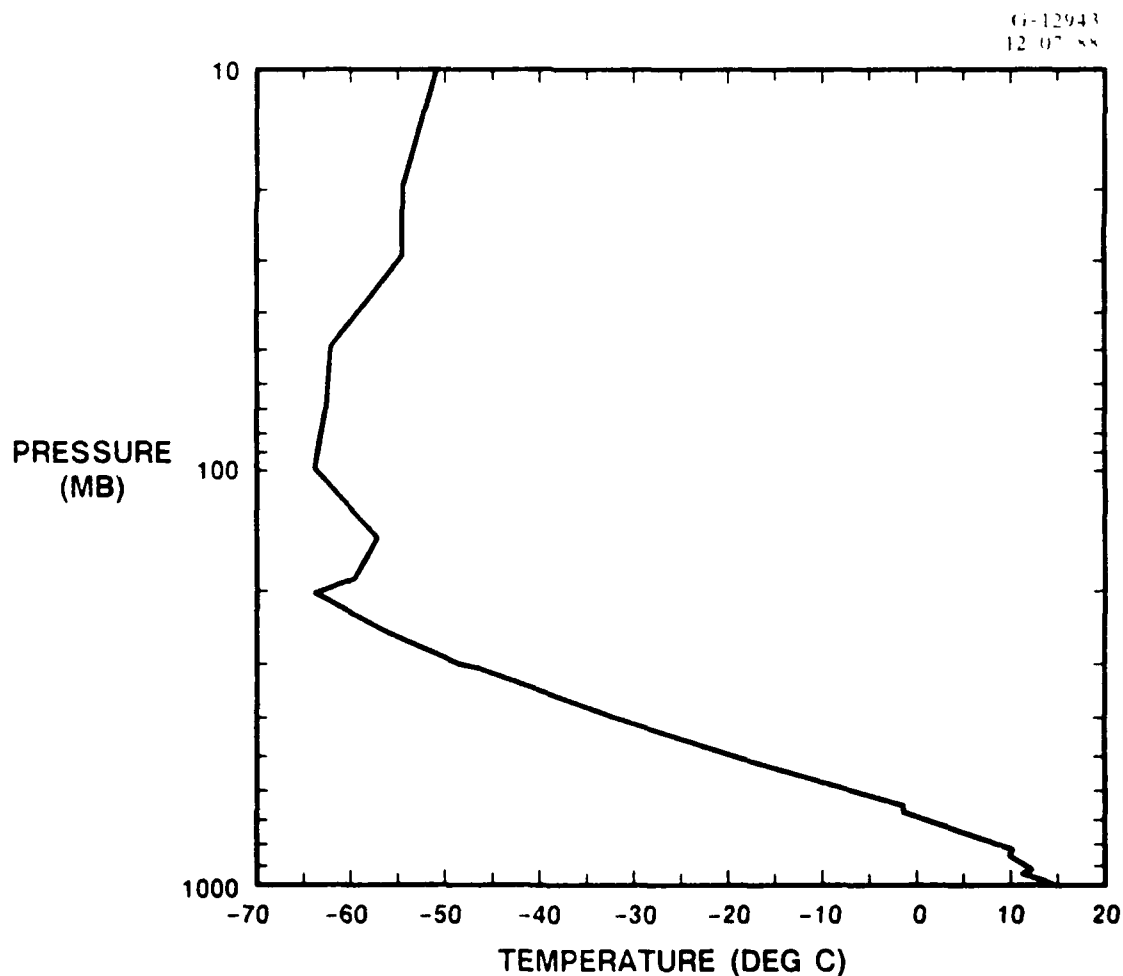


Figure 2.2-1 Gibraltar Temperature Profile

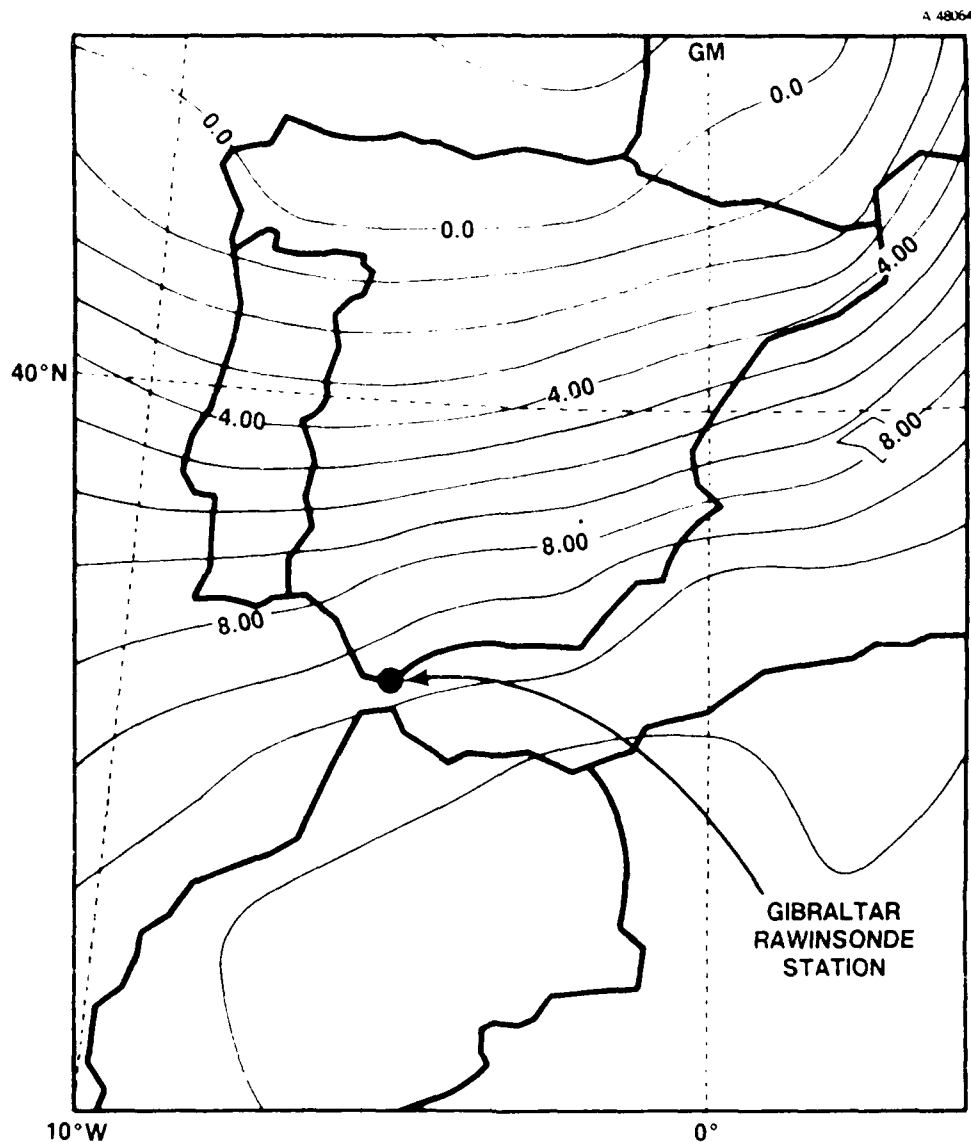


Figure 2.2-2 NMC Temperature Analysis (850 mb) (deg C)

temperature field for 1200 UTC 4 March 1982 interpolated to a 1 deg by 1 deg grid (~ 100 km) and contoured in 2 deg C increments. The horizontal temperature gradient on each surface was computed at every grid point, then values within a 5x5 subgrid centered on Gibraltar were averaged, yielding representative gradients at 850, 700, 500, 300, 200 and 100 mb. (A 3 x 3 subgrid could have been selected, since its area would approximate the size of the area over which radiance gradients were computed. However, it was decided that the 5 x 5 subgrid would provide more information about the atmosphere around and above Gibraltar.) The results of the gradient computation are shown in Table 2.2-1.

Table 2.2-1 Temperature Gradients Based on a 5 x 5 Subgrid (deg C/m)

PRESSURE (mb)	TEMPERATURE GRADIENTS	
	ZONAL (East)	MERIDIONAL (North)
850	2.71×10^{-6}	-1.16×10^{-5}
700	5.87×10^{-7}	8.72×10^{-6}
500	-1.37×10^{-6}	-5.40×10^{-6}
300	3.68×10^{-7}	-4.87×10^{-6}
200	4.22×10^{-7}	-3.23×10^{-6}
100	-2.99×10^{-7}	8.54×10^{-6}

The temperature gradients at six levels were interpolated and extrapolated to produce the profiles shown in Fig. 2.2-3. Note well the significantly larger magnitude of the *north* component which will be reflected throughout the report by the emphasis on the *east* component of the wind profile estimates. Although computations can be, and are, carried out for the north component of the thermal wind profile, the magnitudes are typically within the "noise" of the available data and should not be considered very meaningful.

In order to reflect an operational situation with some realism, the "exact" temperature gradient profiles in Fig. 2.2-3 were not used in most of the following results. Instead, reasonable piecewise linear approximations to the two components were used which are representative of what might be generated from, for example, forecasts of the temperature fields in the region. Figure 2.2-4 shows three different approximations to the (larger) north component and the single approximation used for the (smaller) east component, each superimposed over the corresponding data-derived profile. Sensitivity of the algorithm to the assumed profile will be indicated by results based on these three north-component approximations presented in the next subsection.

2.2.3 Baseline Optimal Estimation Results

The primary purpose of this section is to establish the baseline case on which the sensitivity results presented in the next subsection are based. Of almost equal importance are the

G-12942
1-5-89

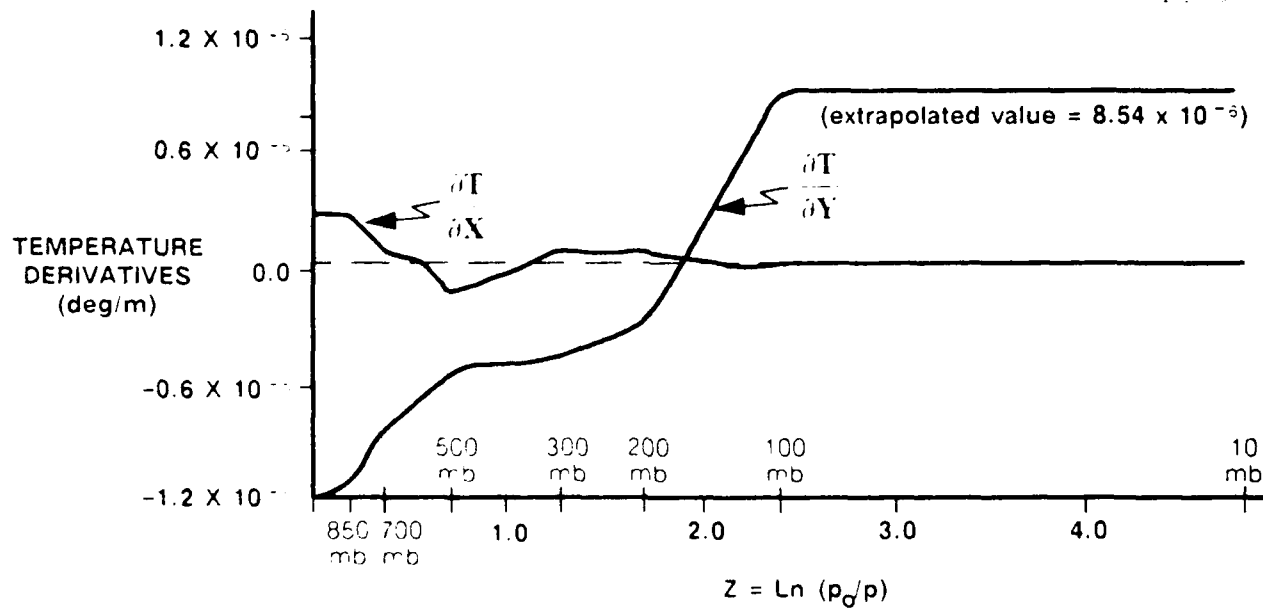


Figure 2.2-3 Temperature Gradient Profile

G-12942
1-5-89

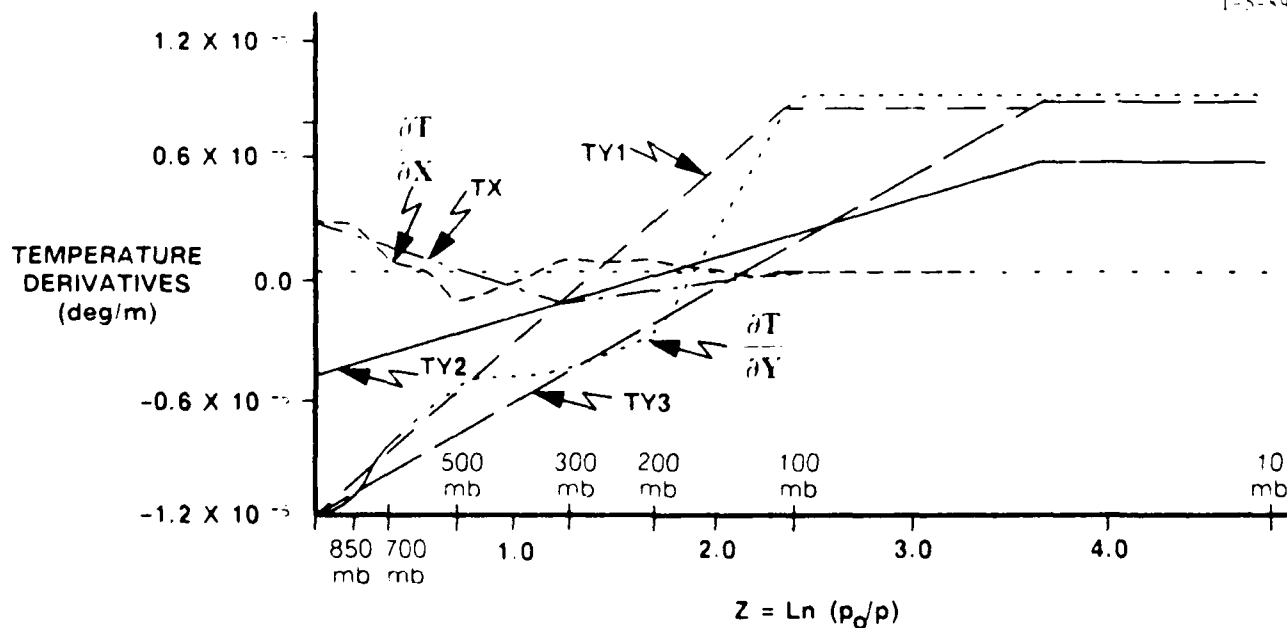


Figure 2.2-4 Approximate Temperature Gradient Profiles

results concerning dependence of the new optimal estimation algorithm on three fundamental selections:

- Choice of the grid from which the radiance gradient data are derived
- Choice of the HIRS 2 channels (i.e., wavelengths) used by the data processor
- Choice of the initial guess of the temperature gradient profile.

Our *baseline case* will be based on the following selections:

- Radiance gradients computed from the 7 x 7 grids (as discussed in Section 2.1)
- Channels 3, 4, 5, 6, 15, and 16
- The interpolated temperature gradient profiles in Fig. 2.2-3.

Selection of the 7 x 7 grid radiance gradient has been discussed in Section 2.1. The six IR channels were chosen because their levels of peak energy contributions appear within the troposphere and are less likely to be influenced by earth surface effects. Finally, while using the interpolated temperature gradient profile may not be realistic operationally, its use here as the baseline permits more accurate evaluation of the algorithm's sensitivity with respect to model parameters. Detailed investigations of the influence of the choice of approximate temperature gradient profiles and of channels are summarized in this subsection.

Results for The Baseline Case are summarized in Table 2.2-2. In all of the tables in this subsection, estimates entered on a line corresponding to a specific pressure are of the *difference* between the geostrophic wind component at that level and that at the reference level (850 mb in all cases). This table displays both the initial thermal wind estimate which is consistent with the

Table 2.2-2 Results of the Baseline Case⁽¹⁾

PRESSURE LEVEL	INITIAL THERMAL WIND ESTIMATE		FINAL THERMAL WIND ESTIMATE	
	EAST	NORTH	EAST	NORTH
700 mb	6.6	1.1	10.5	7.2
500 mb	14.6	0.6	23.1	4.3
300 mb	23.4	-0.2	37.0	-1.5
200 mb	28.9	0.3	45.7	2.1
100 mb	22.7	0.8	35.9	5.2

(1) Wind speeds in m / s

initial temperature gradient profile and the final estimate which results from processing the satellite data. Note the significant difference in the relative magnitude of the two wind components (in both the initial and final estimates): this is consistent with the earlier comments regarding the much smaller temperature derivative in the east-west direction. Note also that there is significant difference between the initial and final thermal wind estimates. This is the first clear indication that the satellite radiance data are, in some sense, inconsistent with the initial temperature analysis field.

Dependence on Temperature Gradient Profile

As noted earlier, an operational algorithm cannot expect to have a complete temperature gradient profile derived from independent soundings available at forecasting times. In order to study the effect of using an approximate profile, the four piecewise-linear approximations to the interpolated profile which were shown in Fig. 2.2-4 are used in the algorithm. (TX in the figure represents an approximation to the east derivative and TY1, TY2 and TY3 are approximations to the north derivative.) Tables 2.2-3 and 2.2-4 respectively contain the *initial and final* thermal wind estimates based on each of these approximations (as well as the baseline results for comparison).

As would be expected, the good piecewise linear approximations to the interpolated measurements (TX and TY3) yield results which are close to those obtained using the exact measured profile at most levels. The sign differences which appear in the north-component estimates do not represent significant deviations because the magnitudes are very small. The other two east-component approximations result in estimated profile \bar{u} , \bar{v} represented by

Table 2.2-3 Initial Thermal Wind Estimates⁽¹⁾

PRESSURE LEVEL	EAST COMPONENT				NORTH COMPONENT	
	BASELINE (MEASURED)	APPROXIMATIONS			BASELINE (MEASURED)	TX
		TY1	TY2	TY3		
700 mb	6.6	6.1	2.7	6.6	1.1	1.2
500 mb	14.6	13.5	6.3	16.1	0.6	1.8
300 mb	23.4	17.6	9.4	25.7	0.2	0.0
200 mb	28.9	14.6	9.7	29.2	0.3	-1.2
100 mb	22.7	1.6	6.1	26.6	0.8	-1.5

(1) Wind speeds in m/s

Table 2.2-4 Final Thermal Wind Estimates⁽¹⁾

PRESSURE LEVEL	EAST COMPONENT				NORTH COMPONENT	
	BASELINE (MEASURED)	APPROXIMATIONS			BASELINE (MEASURED)	TX
		TY1	TY2	TY3		
700 mb	10.5	11.7	10.5	9.7	7.2	6.2
500 mb	23.1	26.1	24.8	23.6	4.3	9.6
300 mb	37.0	34.0	36.9	37.6	1.5	0.1
200 mb	45.7	28.2	38.4	42.7	2.1	6.2
100 mb	35.9	3.1	24.0	38.8	5.2	-8.1

(1) Wind speeds in m/s

values at five distinct levels) which are somewhat farther from the Baseline estimate. *The important point is that although the initial profiles corresponding to these approximations are substantially different than the Baseline initial profile, the final estimates are much closer to those for the Baseline.* That is, there is a convergence toward a common profile as a result of processing the satellite radiance gradient data. (See also the Executive Summary and Fig. ES-2).

Dependence on Choice of Channels

As indicated above, the six IR channels in Table 2.1-1 were chosen because of the location of their peak absorption bands and their (relative) lack of sensitivity to surface radiance. The purpose of this brief section is to present one set of results based on *subsets* of those six channels. Again, only the east-components of the thermal wind estimates are considered. Approximation TY2 was used for the temperature derivative profile in this study to reflect a non-ideal operating condition. Table 2.2-5 contains the five-level profiles for six selections of channel sets along with the six-channel results from Table 2.2-4.

Comparing Case II with the all-channels result indicates that the omitted channel 4 data can be eliminated with little effect *for this case*. On the other hand, while dropping channel 6 (Case I) produces a large change in the estimated profile, dropping both channels 6 and 15 (Case III) again produces a result close to the all-channels result. Case IV, another set of four channels, is significantly poorer than Case III. Cases V and VI, which use only three channels, produce equally poor estimates.

Table 2.2-5 Thermal East Wind Profile Estimate
Dependence on Channel Selection⁽¹⁾

PRESSURE LEVEL	ALL CHANNELS (Table 2.2-4, LY2 result)	CASE NUMBER CHANNELS					
		I	II	III	IV	V	VI
		3,4,5, 15,16	3,5,6, 15,16	3,4,5, 16	3,4, 15,16	3,4, 15	3, 15,16
700 mb	10.5	7.1	10.4	11.7	4.1	4.4	3.9
500 mb	24.8	16.8	24.6	27.7	9.8	10.3	9.2
300 mb	36.9	25.1	36.7	41.2	14.6	15.3	13.8
200 mb	38.4	26.0	38.1	42.8	15.1	15.9	14.3
100 mb	24.0	16.3	23.9	26.8	9.5	9.9	8.9

(1) Wind speeds in m/s

In examining these results, it should be remembered that the underlying idea is to find a linear combination of functions (the kernel functions, K_i) such that the statistical optimization criterion is minimized. Therefore, using fewer of those functions can only increase the expected square error. From the point of view of looking for an operational implementation of the algorithm, using four channels (instead of six) offers an insignificant saving in computer time and data handling requirements, so is not a critical design issue. It would be possible to investigate the contributions of each channel over a statistically significant data set and make recommendations regarding the best choice for channel wavelengths, but such an effort is beyond the scope of this research contract.

2.3 OHRING'S METHOD

The approach to wind shear profile estimation proposed by Ohring, Neeman, and Duncan (Ref. 1) was discussed in Ref. 2 as a point of departure for the new optimal estimation approach under investigation. In order to compare results of the two approaches, the basic algorithm in Ref. 1 (hereafter referred to as Ohring's method) is outlined in this section. These equations will be used again later while discussing sensitivity of the two algorithms.

The estimate of the wind shear (east component) between levels z_i and z_{i+1} is based on a weighted sum of measured (actually, estimated) radiance gradients just as is the optimal estimator developed in this research.

$$u_1(i) = -(R/f) c_i^T R_y \quad (2.3-1)$$

where the subscript L indicates an estimate of wind shear over one specific atmospheric layer, and

$$R_y = \left(\frac{\partial R_1}{\partial y} \quad \dots \quad \frac{\partial R_m}{\partial y} \right)^T \quad (2.3-2)$$

(m = number of radiance measurement channels), and the i subscript in c_i emphasizes that the optimal weights depend on the layer through which the thermal windshear is estimated. The vector of weights, c_i , is calculated to minimize the following function:

$$J(c_i) = \int_0^1 \left[\sum_j c_{ij} K_j(\zeta) - w_i(\zeta) \right]^2 d\zeta \quad (2.3-3)$$

where

$$w_i(\zeta) = \begin{cases} 1 & z_i < \zeta < z_{i+1} \\ 0 & \text{otherwise} \end{cases} \quad (2.3-4)$$

The K_j , $j = 1, \dots, m$, are the same kernel functions used in the new optimal estimation approach. This corresponds to "Method 1" in Ref. 1. Although four other minimization criteria were evaluated in that reference, there was not a sufficient improvement using the more complex criteria which warranted their implementation for this comparison. The optimal weighting vector is calculated using,

$$c_i = M^{-1} b_i \quad (2.3-5)$$

where

$$M = \int_0^1 \underline{K}(\zeta) \underline{K}(\zeta)^T d\zeta \quad (2.3-6)$$

and

$$b_i = \int_{z_i}^{z_{i+1}} \underline{K}(\zeta) d\zeta, \quad i = 1, \dots, n \quad (2.3-7)$$

Two results using Ohring's method are presented, one using all six HIRS/2 channels, and the second using a subset containing channels 3, 4, and 15. While these two cases will be compared with results of the Optimal Estimation Approach presented in the previous subsection, they certainly do not constitute a complete evaluation of Ohring's method for the sample data set. As will be shown, kernel functions for the six HIRS/2 channels are far from ideal for

approximating the pulse-shaped weighting functions (Eq. 2.3-4). This condition leads to severe numerical problems when implementing Ohring's method in a straightforward manner.

Using the radiance gradients computed from 7 x 7 grids (as discussed in Section 2.1) and all six HIRS/2 channels resulted in the extremely poor estimates of the East thermal wind within each layer shown in Table 2.3-1. The reason for this poor result is that the least-squares problem (see Eq. 2.3-3) leads to a minimizing solution vector, \hat{c}_i , for layer i which has a very large norm because of the poorly conditioned M matrix (Eq. 2.3-6). This poor conditioning is a direct result of the *dependence* among the kernel functions (see Appendix C). That is, the kernel functions are too similar so that there exist linear combinations of them which are nearly identically zero on each interval of interest.

That the least-squares problem has been solved correctly is demonstrated in Figs. 2.3-1 through 2.3-5 which show the (ideal) pulse function and the approximating curve defined by the "optimal" linear combination of the six kernel functions (solid curves) for each of the five layers within which the thermal wind is estimated. Clearly, the approximating functions have large non-zero portions outside of the estimated layer, a direct consequence of the enforced minimization of the criterion function.

For the three-channel case, the approximating functions (dashed lines in Figs. 2.3-1 — 2.3-5) while not as "sharp" in the region of the ideal pulses, avoid much of the large side-lobe oscillations. (See, for example, the much smoother curves for the two layers above 300 mb.) But, as shown in the right-hand column of Table 2.3-1, this three-channel case results in more reasonable estimates of the East thermal wind in each layer.

Table 2.3-1 Ohring's Method Results: East Component of Thermal Wind

LAYER	6 CHANNELS	3 CHANNELS
850 — 700 mb	-5.0	3.0
700 — 500 mb	-132.1	8.1
500 — 300 mb	172.1	13.4
300 — 200 mb	109.1	6.9
200 — 100 mb	-431.4	5.4

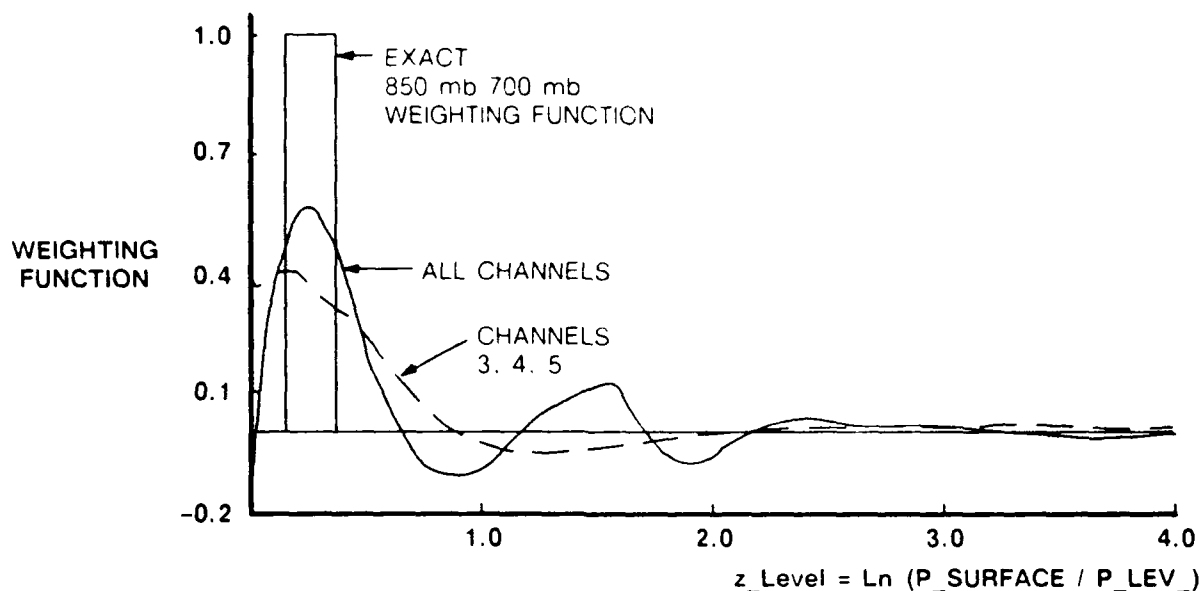


Figure 2.3-1 Weighting Function Approximations on 850 mb to 700 mb

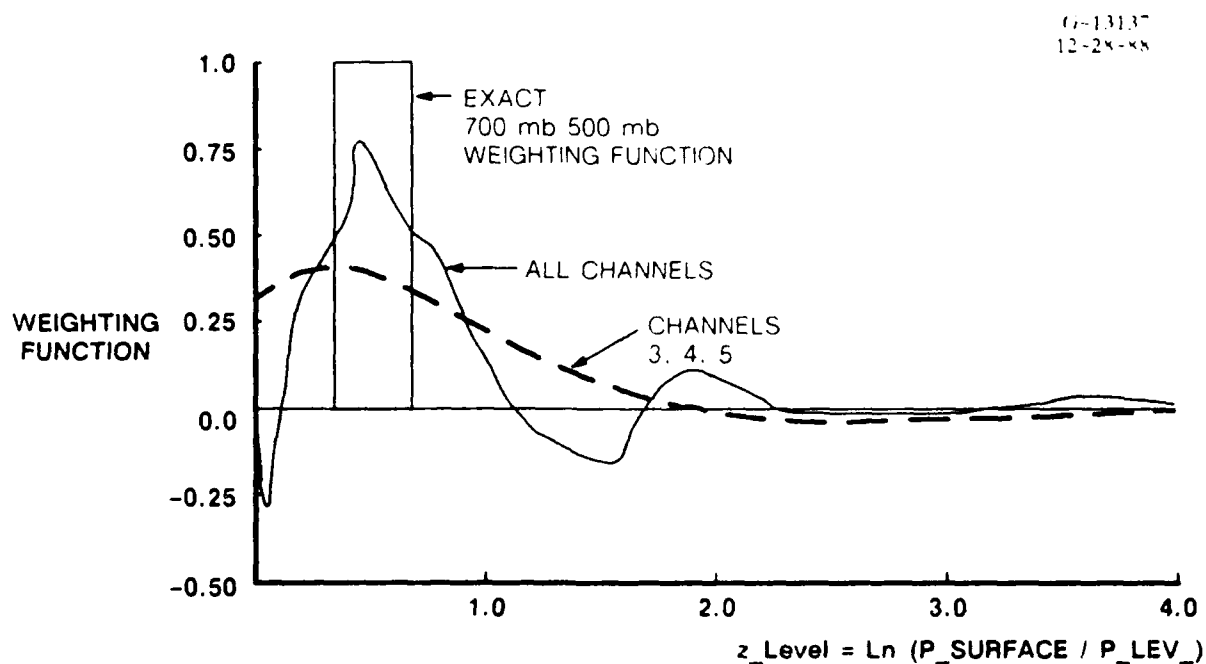


Figure 2.3-2 Weighting Function Approximations on 700 mb to 500 mb

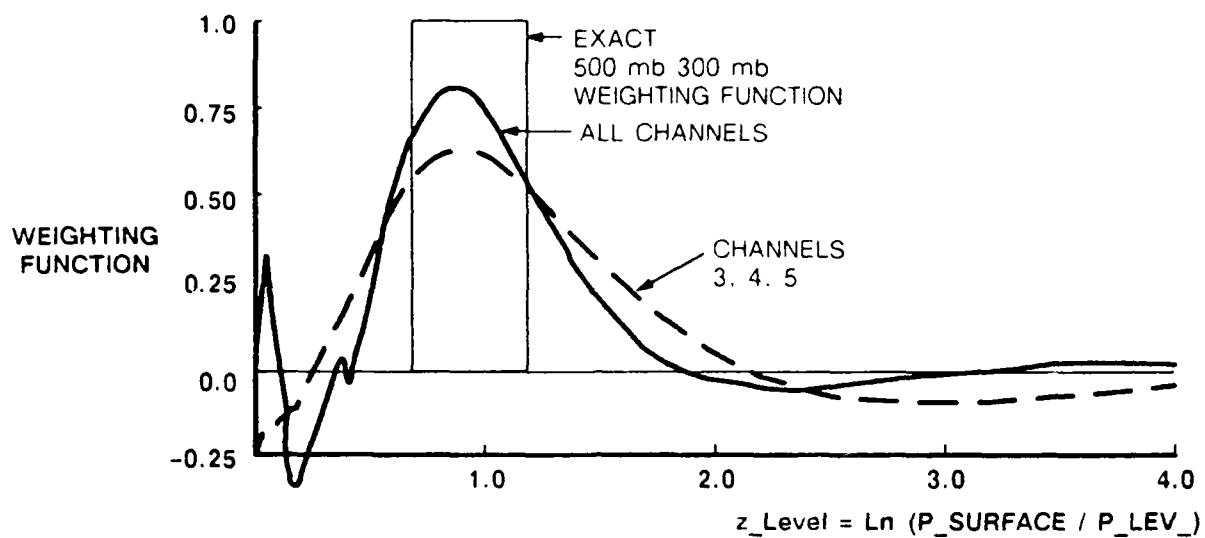


Figure 2.3-3 Weighting Function Approximations on 500 mb to 300 mb

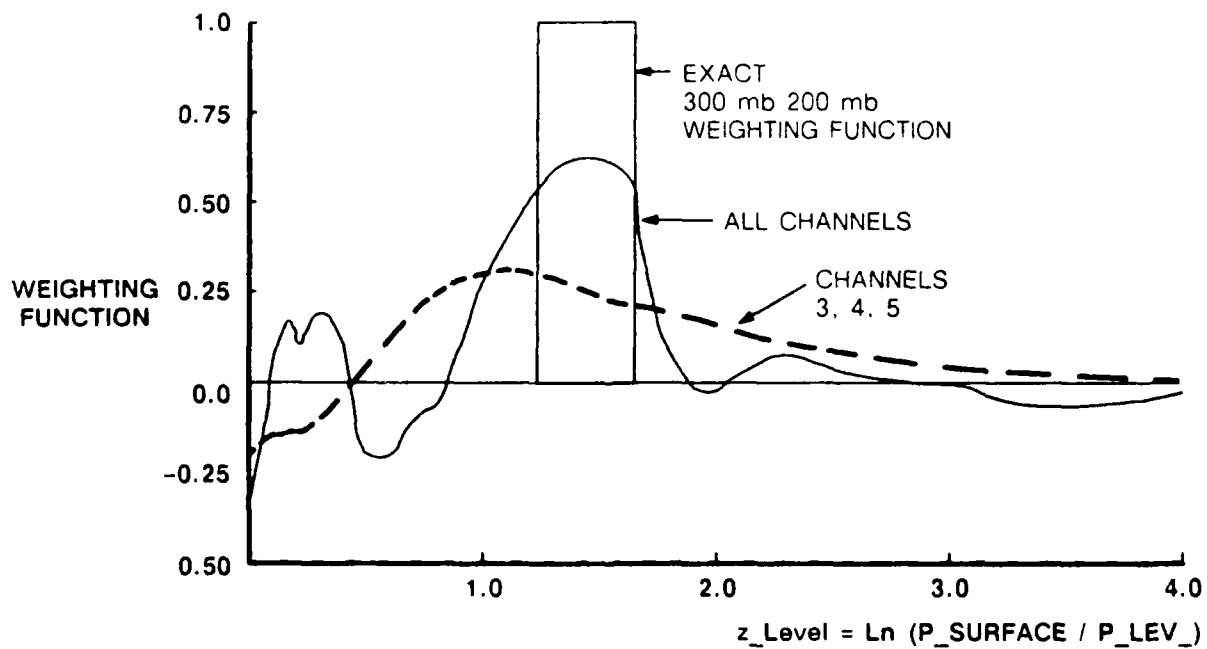


Figure 2.3-4 Weighting Function Approximations on 300 mb to 200 mb

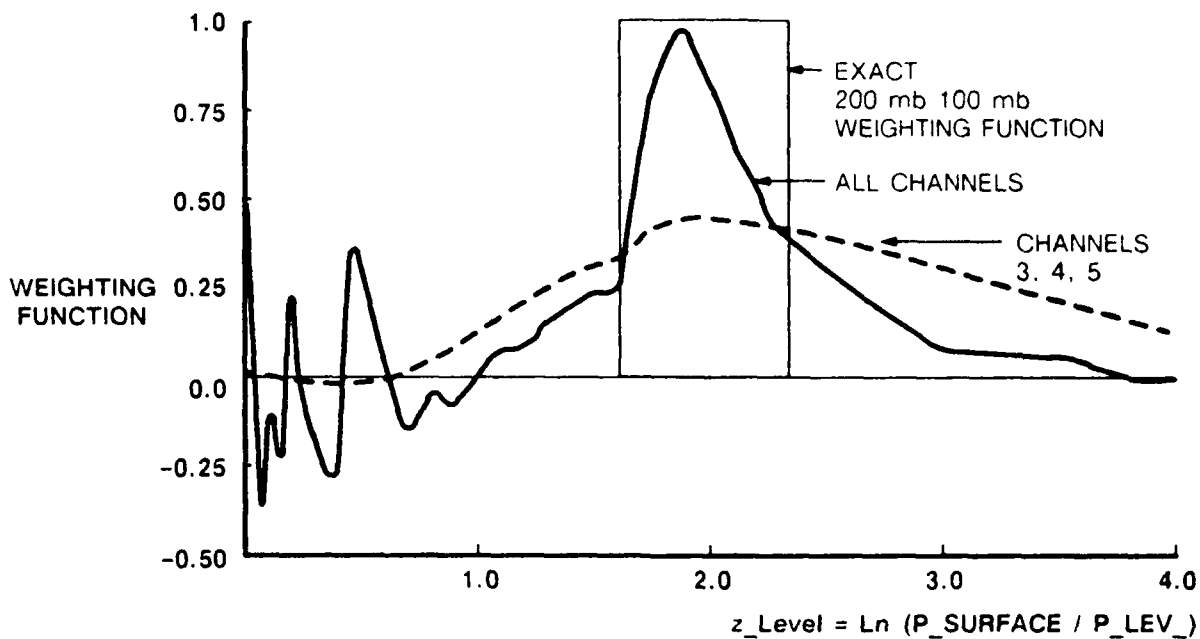


Figure 2.3-5 Weighting Function Approximations on 200 mb to 100 mb

Table 2.3-2 contains the calculated coefficients for two typical layers for the two cases and Table 2.3-3 shows the East component estimate contributions resulting from these coefficients. Clearly, the large coefficients in the six-channel case lead to sums of positive and negative terms whose magnitudes are much larger than the estimated quantities. This effect is especially clear in channels 4, 5 and 6, a direct result of the similar kernel functions for these channels (see Appendix C).

Table 2.3-2 Optimal Coefficients from Ohring's Method (East Component)

CHANNEL	LAYER			
	850 mb — 700 mb		200 mb — 100 mb	
	6 channels	3 channels	6 channels	3 channels
3	-557	-213	4951	-1381
4	3963	301	-4.05×10^4	193
5	-9730	-----	6.56×10^4	-----
6	4986	-----	-2.04×10^4	-----
15	-5.50×10^4	-1.85×10^4	-4.94×10^5	-1987
16	4.37×10^5	-----	-8.19×10^5	-----

Table 2.3-3 Optimal Ohring's Method Contributions (East Component)

CHANNEL	LAYER			
	850 mb — 700 mb		200 mb — 100 mb	
	6 channels	3 channels	6 channels	3 channels
3	3.4	1.3	-29.7	8.3
4	-76.3	-5.8	780.9	-3.7
5	451.5	---	-3044.8	---
6	-406.2	---	1662.2	---
15	22.4	---	200.7	---
16	0.4	7.5	-0.7	0.8
TOTAL	-5.0	3.0	-431.4	5.4

Finally, Table 2.3-4 lists the estimates for both components of the thermal wind profile produced by Ohring's method (using only channels 3, 4 and 15) along with those generated by the Optimal Estimation Technique. (The East component of this profile was presented earlier in Table 2.2-5, case V.) Note that the values in Table 2.3-4 are the estimated thermal wind between the indicated level and the reference, 850 mb, level; the east component values, for example, are obtained from the results in Table 2.3-1 by summing the layer estimates up to the indicated pressure level. It should be emphasized that there is no fundamental difference between

Table 2.3-4 Comparison of Optimal Estimation and Ohring's Method Estimates (Channels 3, 4, and 15)

LEVEL	WIND PROFILE (m/s)			
	East		North	
	Ohring	Opt. Est.	Ohring	Opt. Est.
700 mb	3.0	4.4	-5.2	-0.4
500 mb	11.0	10.3	1.0	-0.6
300 mb	24.5	15.3	27.7	-0.0
200 mb	31.4	15.9	39.0	0.4
100 mb	36.8	9.9	33.0	0.5

the two formulations (i.e., layer-by-layer estimates vs. summed-layers); Ohring's method and the Optimal Estimation approach have much different characteristics, but *not* because of this feature of their formulation.

To summarize, although Ohring's method is susceptible to numerical difficulties due to dependent kernel functions, it could be stabilized by using a singular value decomposition procedure or any similarly robust algorithm for ill-conditioned least-squares problems (Ref. 3). The important difference between Ohring's method and the Optimal Estimation approach is that because the former method is based on obtaining a least-squares fit to the pulse functions (Eq. 2.3-4), its estimated profiles can never achieve a smaller mean-square estimation error than those of the latter approach over a representative sample of cases.

2.4 SENSITIVITY EVALUATIONS

The objective of this sensitivity evaluation is to demonstrate the dependence of thermal wind profile estimates on algorithm data and parameters. The first subsection deals only with the new optimal estimation algorithm and uses direct perturbation of the data and parameters to evaluate sensitivity. In the second subsection, analytical expressions derived in Appendix F for logarithmic derivatives of the estimates of both the optimal estimation and Ohring algorithms will be used. These local results describe sensitivity with respect to small changes in the kernel functions and provide a basis for two interesting comparisons: first, with the large-scale perturbation results for kernel functions presented in the first subsection, and second, between the local sensitivities of the optimal estimation and Ohring algorithms.

Results in this section augment the investigations reported in Section 2.2.2 into dependence of the optimal estimation algorithm on the assumed temperature gradient profile and on the choice of HIRS/2 channels. Emphasis in this section is on perturbation of scalar parameters instead of those more complex algorithm variations. The kernel function sensitivities reported here are, in fact, also based on functional perturbations although those perturbations are defined by scalar parameters.

2.4.1 Perturbations of Data and Parameters

All perturbations presented in this section are departures from the data and parameters used in the *baseline case* described in Section 2.2.2 for the optimal estimation algorithm. Sensitivities with respect to the following data and parameters have been investigated:

- Temperature gradient profile
- Radiance gradients
- Radiance gradient error covariance matrix
- Kernel functions.

Sensitivities were evaluated separately for each item, then a single run was made with all of these items perturbed to assess the combined effects in at least one case. Each of the investigations required a slightly different perturbation technique; these are discussed individually along with each result in the remainder of this subsection.

Results are expressed in normalized form; fractional (or percentage) change in the estimate is plotted against fractional change in the parameter. One can define a scalar sensitivity, based on a *linear* model by

$$S_{ij} = [\Delta u_i / u_i^0] / [\Delta p_j / p_j^0] \quad (2.4-1)$$

where the superscript ⁰ represents baseline values. Values of S_{ij} will be used in the following discussion when comparing sensitivities with respect to different parameters. Finally, results are presented only for the effect of perturbations on the zonal (i.e., east) component of the thermal wind estimate. This choice was made because the meridional (north) component of the thermal wind estimate was too small to be significant.

i) Temperature Gradient Profile Errors

Zonal wind estimates depend on the meridional component of the temperature gradient profile (Eqs. 2.2-5 and 6). Perturbations were first applied to the temperature gradients developed from the NMC analysis fields (see Section 2.2.2) at two individual levels (850 mb and 500 mb) and then simultaneously at all six levels. For each case, a continuous profile was generated by linear interpolation between the six levels, just as was done to develop the baseline profile in Fig. 2.2-3. Because of this procedure, perturbations at one level cause profile perturbations only between adjacent levels: from 1013 mb (surface) to 700 mb for the 850 mb perturbation and from 700 mb to 300 mb for the 500 mb perturbation.

Two types of perturbations were used: additive and multiplicative. Additive perturbations are of the form

$$T_y(z_i) = T_y^0(z_i) + \alpha |T_y^0(z_i)| \quad (2.4-2)$$

where T_y represents the partial derivative of temperature with respect to y (the north coordinate). The perturbation term in Eq. 2.4-2 is *always positive* and equal to the selected fraction, α , of $T_y(z_i)$. Additive perturbations are characteristic of bias or "drift" instrumentation errors or data processing algorithm effects. Multiplicative perturbations are given by

$$T_y(z_i) = (1 + \alpha) T_y^0(z_i) \quad (2.4-3)$$

where α is the selected fractional perturbation. Multiplicative perturbations are characteristic of scale-factor instrumentation errors or data processing algorithm effects. That these two forms lead to significantly different temperature profiles is illustrated in Fig. 2.4-1 which shows the nominal and both perturbations of the meridional temperature gradient profile based on a 40% perturbation at all levels.

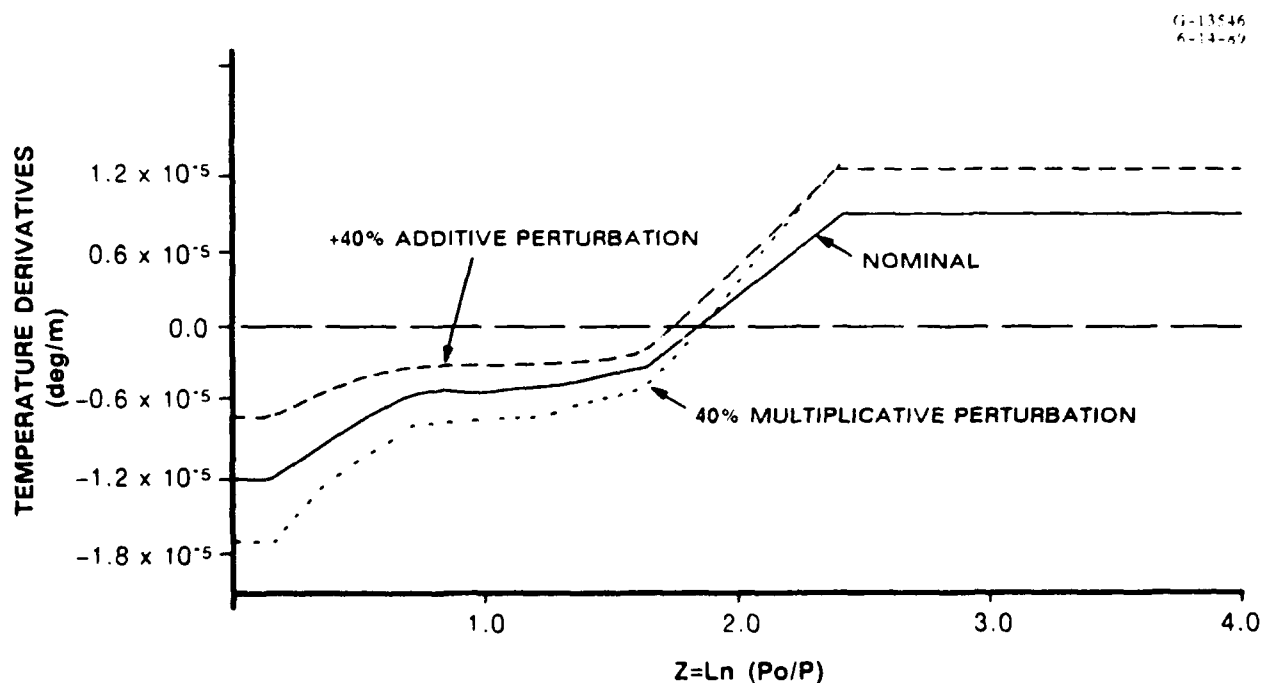


Figure 2.4-1 Nominal and Perturbed Meridional Temperature Gradient Profiles

Results for additive perturbations of 10%, 20% and 40% in the entire meridional temperature derivative profile on thermal wind estimates within three layers are summarized in Table 2.4-1. The radical difference between sensitivities of estimates in layers below 200 mb and that in the 200 mb to 100 mb layer can be understood through careful examination of the estimation equations. Fig. 2.2-3 reveals that the nominal temperature gradient profile reverses sign within the highly sensitive layer, and that sign reversal leads to a perturbation term which does not exist in other layers. Within the other layers sensitivity actually decreases with increasing perturbation, almost surely due to numerical effects.

Additive perturbations of the meridional temperature gradient at only one level produced the results shown in Fig. 2.4-2. (perturbing the gradient at 850 mb) and Fig. 2.4-3. (for the gradient at 500 mb). The positive perturbations decreased the thermal wind estimates in adjacent layers, but increased estimates within other layers in every case. Values of the sensitivity coefficient, S , range between 0.20 and 0.56 for these perturbations. That is, the fractional change in the estimates were smaller than the fractional changes in the data by 44% to 80%.

Multiplicative perturbations produced different sensitivity characteristics, but similar sensitivity coefficient values. Perturbing the temperature gradient values at *all levels* has almost no effect on the estimates. This is a direct consequence of the approximate linearity of the estimates in the temperature gradient profile for the radiance gradient sensitivity model used during this demonstration. The linearity is due to the fact that, in Eq. 2.2-4, the diagonal elements of the second matrix (dependent on θ) dominate the gamma matrix diagonals.

When multiplicative perturbations are applied to values at only selected levels, larger, but still rather small sensitivity is evidenced. Figure 2.4-4 summarizes the results for perturbations in the meridional temperature derivative at 850 mb. The S values for this case, 0.1 and 0.39, are typical of those for multiplicative perturbations at other levels.

**Table 2.4-1 Fractional Changes in Layer Estimates
Due to Additive Perturbations**

ADDITIVE FRACTIONAL CHANGE	LAYER 2 700-500 mb	LAYER 5 300-200 mb	LAYER 6 200-100 mb
0.10	-0.042	-0.042	0.30
0.20	-0.032	-0.032	0.75
0.40	-0.002	-0.003	2.14

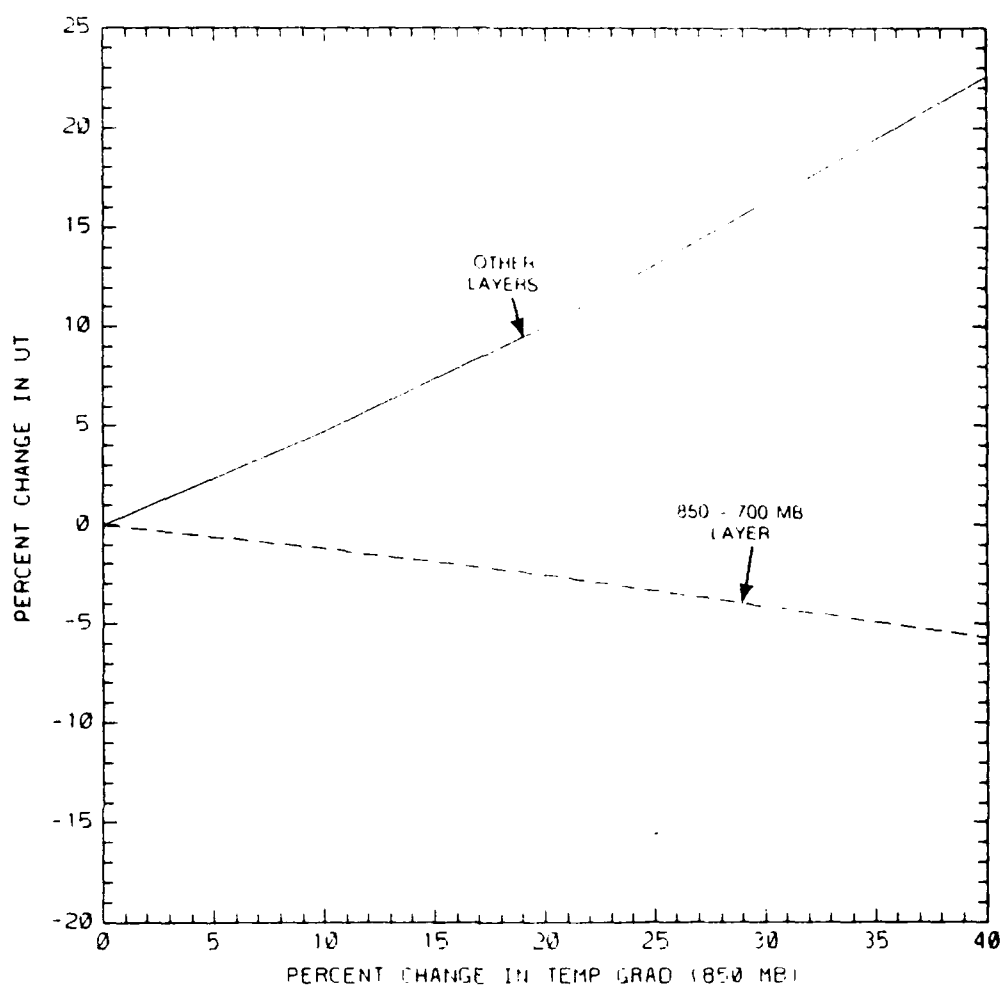


Figure 2.4-2 Sensitivity of Thermal Wind Estimates to a 850 mb Temperature Gradient Additive Perturbation

ii) Radiance Gradient Perturbations

The optimal thermal wind estimation algorithm is a linear mapping of the measured radiance gradients into thermal wind estimates. Therefore, perturbation of all radiance gradient channels according to

$$\nabla \underline{R} = (\nabla \underline{R})_0 (1 + \alpha) \quad (2.4-4)$$

for any α yields a thermal wind estimate scaled by the same $(1 + \alpha)$ factor. (In effect, $S = 1$ for this case.)

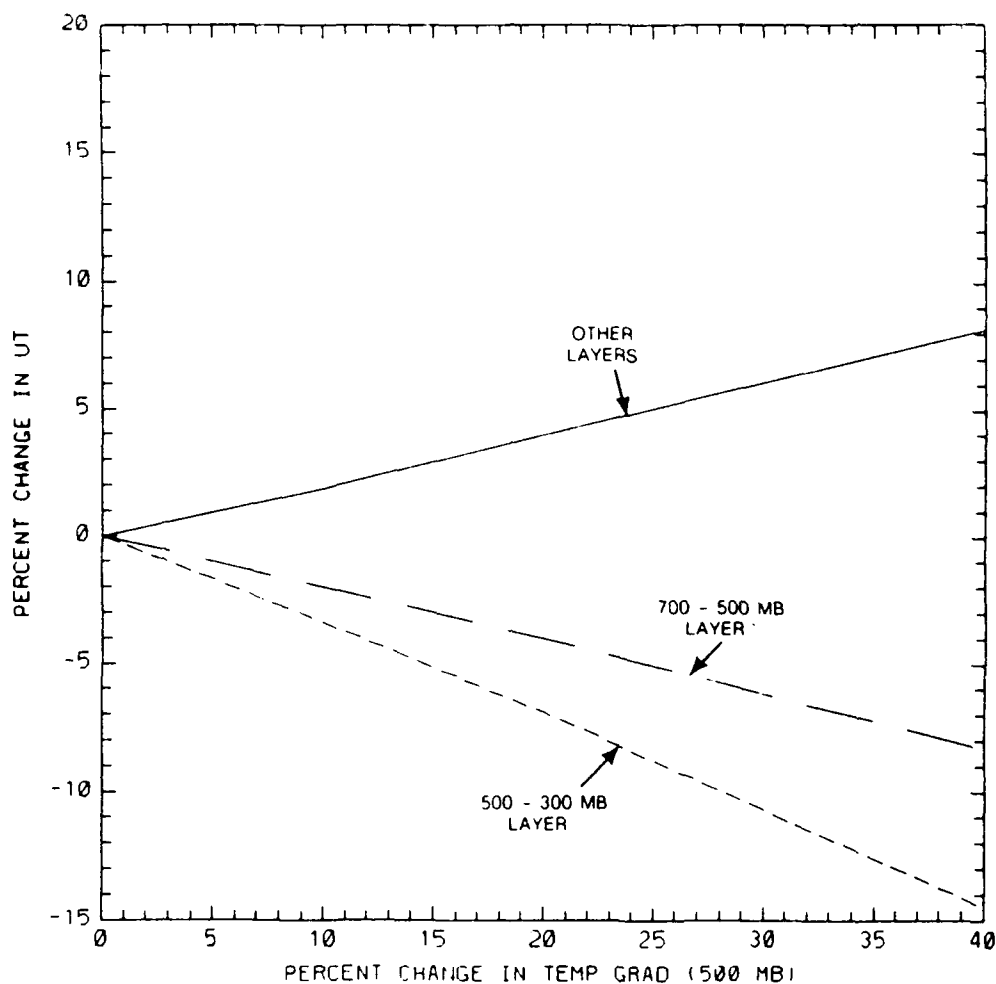


Figure 2.4-3 Sensitivity of Thermal Wind Estimates to a 500 mb Temperature Gradient Additive Perturbation

More interesting results are obtained by considering perturbations in each channel separately. In fact, it is easy to show that, for the thermal wind estimate within any layer resulting from perturbing the j^{th} radiance gradient,

$$\frac{\Delta u}{u^0} = \alpha (a_j/u^0) \quad (2.4-5)$$

where a_j is the contribution to the unperturbed estimate, u^0 , by $\partial R_j/\partial y$. Table 2.4-2 lists the factor $S_j = a_j/u^0$ in Eq 2.4-5 for each of the six channels used in the demonstration. Channels 5,

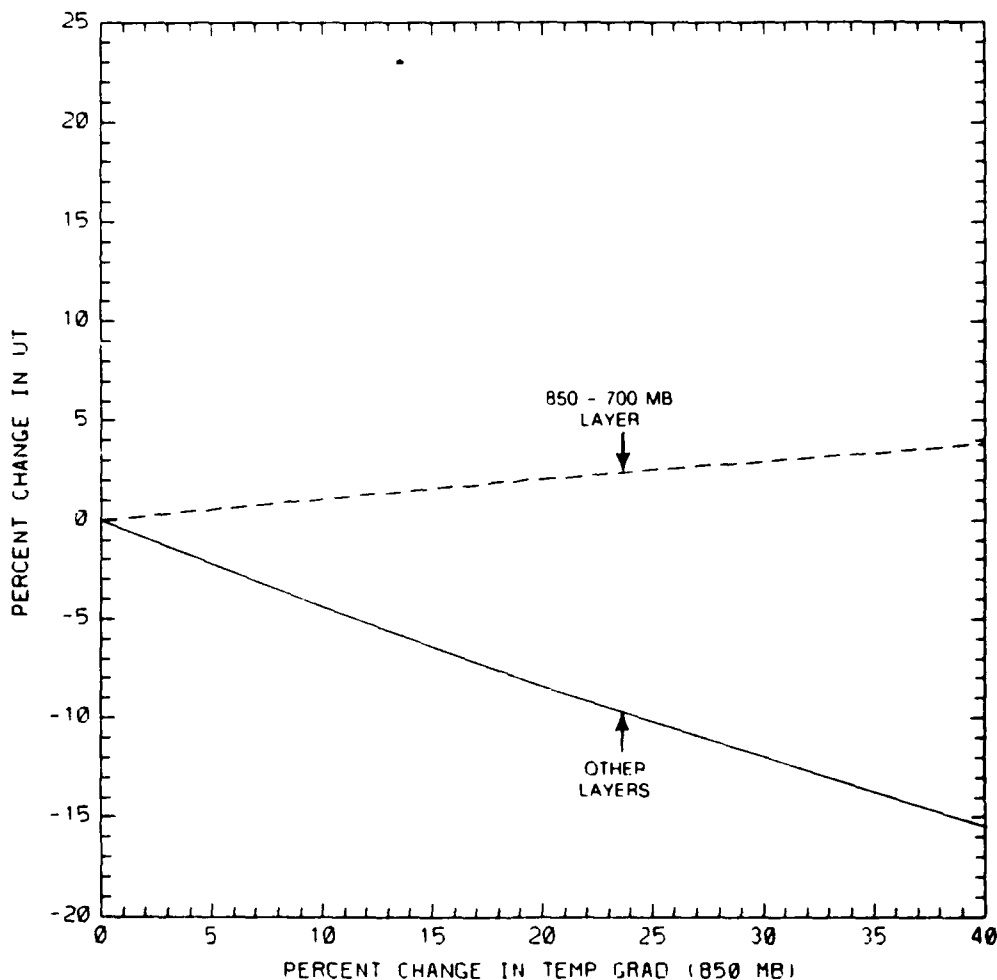


Figure 2.4-4 Sensitivity of Thermal Wind Estimates to a 850 mb Temperature Gradient Multiplicative Perturbation

6 and 15 are clearly the major contributors to the estimates, therefore exhibiting the highest sensitivity.

iii) Radiance Gradient Error Variance Perturbations

These parameters, the diagonal elements of the radiance gradient estimation error covariance matrix, Γ in Eq. 2.2-4, were included in the perturbation analysis because their "correct" values would vary considerably in an operational system due to variations in the radiance-measuring instrument, the geometry of radiance measurements, and possibly atmospheric conditions. If these variations were modeled accurately, significant changes in the error variances could result. (Of course, an implementation of the algorithm could ignore the

Table 2.4-2 Sensitivities with Respect to Radiance Gradient Components

CHANNEL	S
3	0.0029
4	0.0216
5	0.2948
6	0.5220
15	0.1645
16	0.0000

variations and use a conservative, but incorrect, large variance in all conditions. Consideration of this alternative is beyond the scope of the current study.)

For simplicity, all diagonal components were perturbed by an identical scale factor. This is representative of the effects of altered radiance data location geometry, but with the individual channel error variances either remaining fixed or scaling equally. Results for this investigation are presented in Fig. 2.4-5. The relatively small sensitivity of estimates to these parameters is dramatically indicated by the *logarithmic* scale on the abscissa. Note that for scaling by factors less than 1.0, the sensitivity remains zero. The extremely small sensitivity for factors less than 100 is a consequence of the P matrix (Eq. 2.2-4) being dominated by the $\theta\theta^T$ term rather than the Γ matrix.

iv) Kernel Function Perturbations

Kernel function perturbations are the most critical of those considered because of the known sensitivity of the kernel functions themselves to variations in the temperature profile on which they are based. Because an operational implementation would, of necessity, use at best a forecast of the temperature profile at the time of data collection, this known sensitivity could lead to significant thermal wind estimation error.

Kernel function sensitivity to temperature variation was investigated analytically by differentiation and numerically by making finite perturbations in the temperature data. From the kernel function formulas found in Appendix G, one can show that (approximately):

$$S_{T_j}(z) = \frac{T(z)}{K_j(z)} \frac{\partial K_j}{\partial T}(z) = \frac{c_2 v_j}{T(z)} - 2 \quad (2.4-6)$$

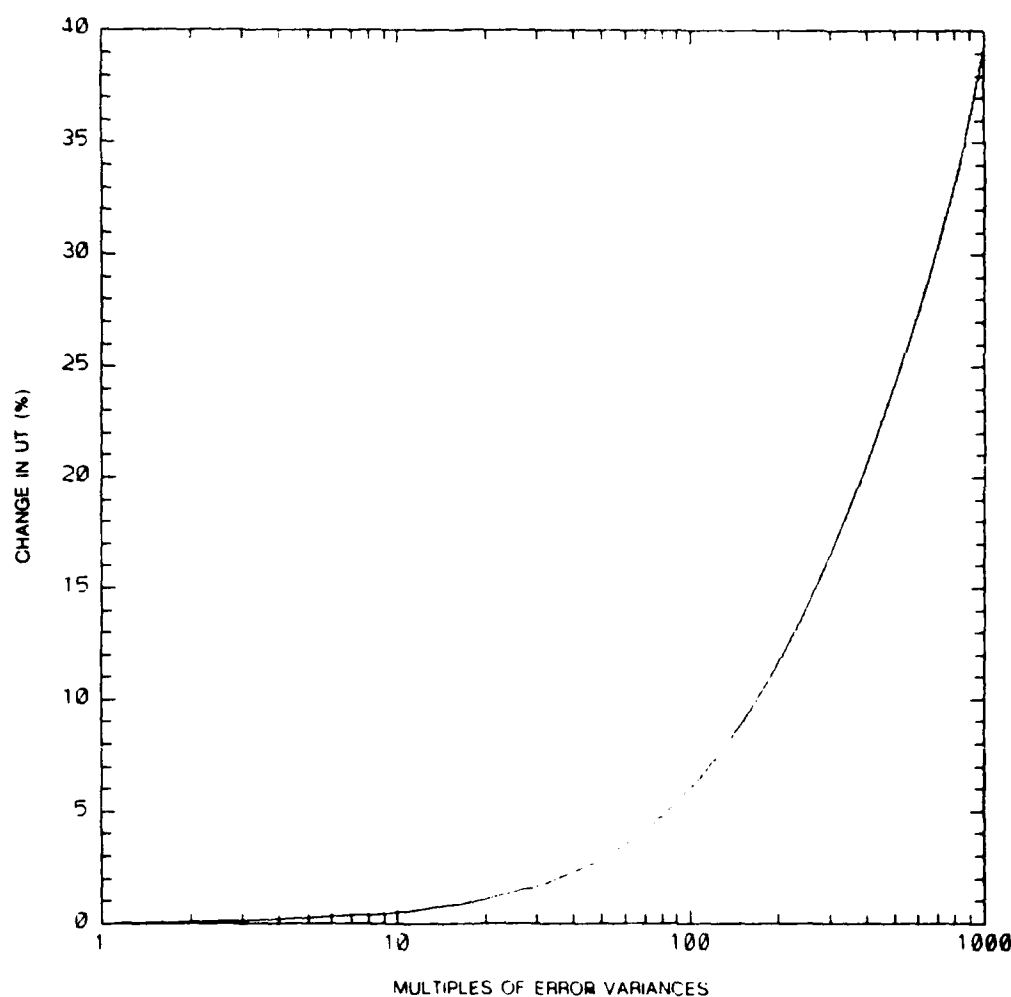


Figure 2.4-5 Sensitivity of Thermal Wind Estimates to Radiance Gradient Error Variance

where

$$c_2 = hc/k = 1.439 \text{ cm deg} \quad (2.4-7)$$

(h and k are the Planck and Boltzman constants and c is the speed of light), and $T(z)$ is the actual temperature at the level, $p(z)$, of interest and ν_j is the wave number (in cm^{-1}) of channel j . The maximum error in Eq. 2.4-6 is under 6% and occurs at that z for which the temperature is a minimum and for the minimum wave number channel ($j = 3$). Applying Eq. 2.4-6 yields the (infinitesimal) sensitivities summarized in Table 2.4-3. Recall that $S_{Tj} = 2.0$, for example, means that a 1% change in $T(z)$ would cause a 2% change in $K_j(z)$. Thus, the sensitivities in

Table 2.4-3 Sensitivity of Kernel Functions to Temperature

CHANNELS	SENSITIVITY (S_{Tj}) RANGE
3, 4, 5, 6 (small wavenumbers)	$1.5 < S_{Tj} < 3.0$
15, 16 (large wavenumbers)	$9.0 < S_{Tj} < 13.5$

Table 2.4-3 are indeed large. However, a 1% change in temperature is, in fact, quite large relative to typical temperature uncertainties for nominal temperatures between 210° K and 289° K. If a profile were in error by 1° K over its entire length (i.e., less than 0.5%), the percentage change in $K_j(z)$ would be on the order of 0.8% and 4% for the low and high wave-number channels, respectively.

For the numerical investigation of kernel function sensitivity to temperature, equal (positive) percentage changes were made to the entire temperature profile, the resulting perturbed kernel functions computed, and the *average* percentage deviation of $K_j(z)$ from its nominal values between $z = 0$ (the reference pressure level, $p = 1013$ mb) and the top of the atmosphere was calculated. Figure 2.4-6 contains plots of this average sensitivity for channels typical of the smaller wave numbers (channel 3) and larger wave numbers (channel 15). The dramatic difference in the behavior of these two cases is due to the effects of the exponential, $\exp\{c_2\nu_j/T(z)\}$, which appears in the Planck function factor of the kernel function formulas (see Appendix F). Clearly, the extreme sensitivity of the higher wave number channels already apparent in the infinitesimal sensitivities in Table 2.4-3 is even more evident in the finite perturbation results. As a result, an operational implementation of the optimal estimation algorithm examined in this project should attempt to use relatively smaller wave number (i.e., longer wave length) channels.

Finally, the impact of uniform percentage changes in the kernel functions on the thermal wind estimates is shown in Fig. 2.4-7. Estimates are *most* sensitive to channel 15 for which $S_T = 0.5$ for up to a 26% change in the kernel function (at all values of z). Perturbations in all channels, which would be the case when perturbations were due to a temperature profile error, lead to $S_T = 0.8$.

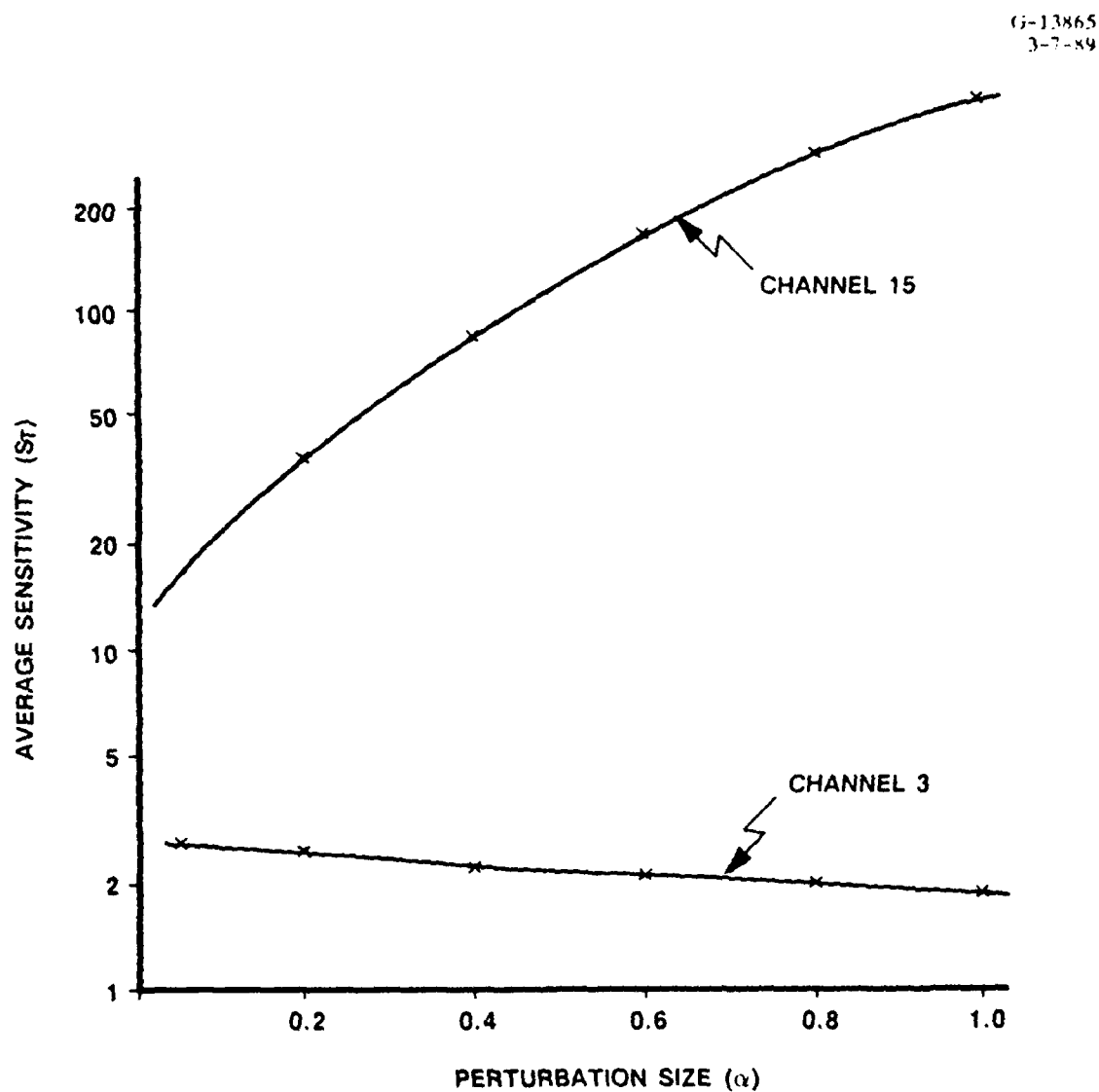


Figure 2.4-6 Average Sensitivity of the Kernel Functions to the Temperature Profile

The investigation presented here did not pursue the obvious next step, calculating estimate sensitivity due directly to temperature profile perturbation, because realistic perturbation profiles were not available during conduct of this study. Because of the relatively large sensitivity of the higher wave number channels, it is extremely important to assess this sensitivity. Realistic temperature profile perturbations, rather than arbitrary constant percentage perturbations, should be used in the study to avoid raising unrealistic concerns due to improbable or impossible parameter perturbations.

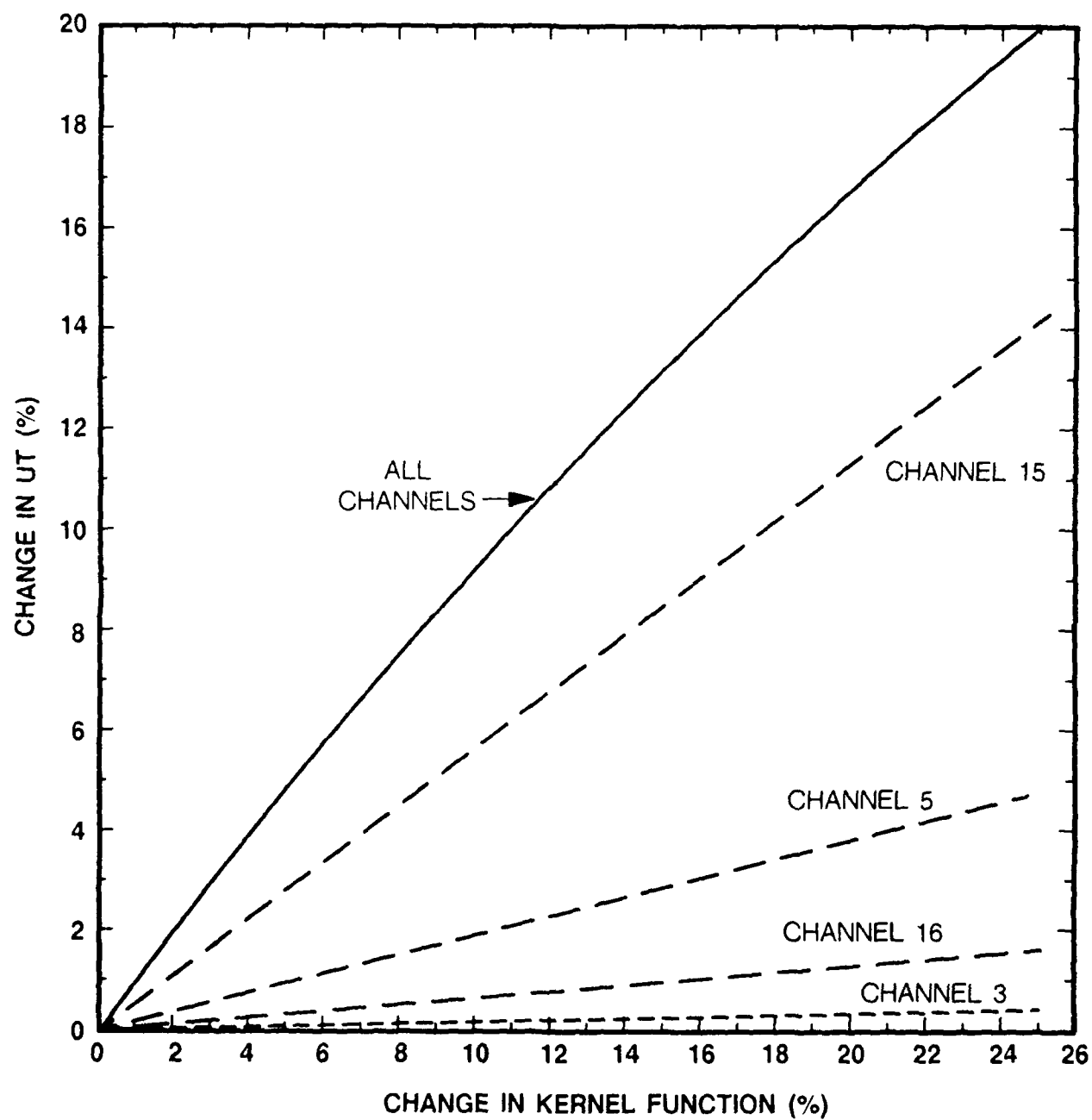


Figure 2.4-7 Sensitivity of Thermal Wind Estimates to the Kernel Functions

v) All-Parameter Perturbations

To evaluate the effect of all parameters being perturbed together in one simple way, additive perturbations of the complete collection of parameters discussed in this section were made simultaneously. Consistent with previous results, the percentage changes in thermal wind estimates across the lower four layers were different than that in the topmost (200 mb - 100 mb) layer. Table 2.4-4 summarizes results for perturbations up to 20%. Note that the fractional change for the sum over all layers is less than that over the first four. This occurred because the estimate in the top layer becomes more negative by 30%, therefore countering much of the positive (11.2%) perturbation over the lower layers. The sensitivity (S) values are included in the table to demonstrate the non-linear nature of the perturbation effects. That is, as the perturbation magnitude increased from 5% to 20%, the ratio of the estimate changes (over all layers) to the perturbation magnitude actually decreased slightly.

It should be emphasized that although the above simple experiment does provide some useful insight into the effects of multiple parameter perturbations, global conclusions regarding sensitivity cannot be drawn from these results. To obtain a more general description of parameter sensitivity, at least two steps should be taken. First, the uniform perturbation of the kernel functions should be replaced by a model of typical temperature profile uncertainties. This should be a statistical model which represents correctly the correlation between temperature perturbations at different levels in the profile. Second, a Monte-Carlo procedure should be used

**Table 2.4-4 Fractional Changes in Thermal Wind Estimates
(All Parameters Perturbed)**

LAYERS	PARAMETER PERTURBATION		
	5%	10%	20%
2 - 5			
Per-Layer	0.11	0.24	0.53
Summed	0.11	0.24	0.53
Sensitivity (S)	2.2	2.4	2.65
6			
Per-Layer	0.30	0.68	1.76
Summed	0.06	0.12	0.20
Sensitivity (S)	1.2	1.2	1.0

to sample perturbations from assumed, reasonable distributions of parameter uncertainties, and the distribution of the resulting estimates examined. Parametric models of those distributions would then provide a convenient way of expressing the optimal estimation algorithm's sensitivity to parameter perturbations as a function of assumed models of the uncertainties in those parameters.

2.4.2 Analytic Sensitivity Results

i) Optimal Algorithm Sensitivity

Equations F.1-3 – F.1-9 which define the logarithmic or fractional sensitivity of each component of the thermal wind estimation vector, \hat{u} , with respect to each of the kernel functions, K_j , were evaluated for the Baseline Case defined in Section 2.2.3. The results contained one surprising but, on reflection, reasonable result and provided valuable insight into interpretation of the perturbation results.

The surprising result is that all rows of the sensitivity matrix are identical, implying that the sensitivity of the estimate is independent of the (upper) level, z . Table 2.4-5 shows the calculated sensitivities. Since these numbers represent *logarithmic* derivatives, they should be interpreted as ratios of fractional changes. For example,

$$\left(\frac{\Delta \hat{u}_1}{\hat{u}_1} \right) = 0.011 \left(\frac{\Delta K_3(z)}{K_3(z)} \right) \quad (2.4-8)$$

Table 2.4-5 Kernel Function Sensitivity Matrix: Optimal Estimate of East Thermal Wind Component

LEVELS	KERNEL FUNCTION COMPONENT (CHANNEL)					
	3	4	5	6	15	16
700 mb } 500 mb } 300 mb } 200 mb } 100 mb }	0.011	-0.013	-0.072	-0.056	-0.18	-0.036

where, on the right-hand side, the ratio is constant for all values of z and the subscript indicates the kernel function for channel 3. Lack of dependence of the sensitivity on the level is due to the normalization in Eq. 2.4-8 and is consistent with Eq. 2.2-9 which showed that the kernel functions affect the estimates only through the scalar, d , which is independent of level.

The sign pattern (channel 3, +, all others, -) of the sensitivities is consistent with the signs of the weights, c_i , used to form the optimal thermal wind estimate. The relative magnitudes of the terms are consistent with the relative magnitudes of the sensitivities displayed in Fig. 2.4-7. The absolute magnitudes of the sensitivities are much lower in Table 2.4-5 (by a factor of two to three). This is due to nonlinear effects which drove the earlier perturbation results but is not important in the infinitesimal case.

ii) Ohring Method Sensitivity

The sensitivity matrix for Ohring's method is computed using Eqs. F.2-3 - F.2-9. Table 2.4-6 contains this sensitivity matrix for the three channel estimation case (see Tables 2.3-2, 3, and 4). The contrast with the preceding case is clear. The sensitivity varies with the upper limit of the layer over which the estimate was formed (the lower limit was 850 mb in each case). More importantly, the magnitude of the sensitivities are much larger in the Ohring method sensitivity matrix. This is a significant result, provided it can be shown to hold over a variety of cases (i.e., data collection geometries and channel frequencies).

Table 2.4-6 Kernel Function Sensitivity Matrix: Ohring Estimate of East Thermal Wind Component

LEVELS	KERNEL FUNCTION COMPONENT (CHANNEL)		
	3	4	15
700 mb	-0.35	0.97	-0.33
500 mb	-0.16	0.55	-0.16
300 mb	-0.087	0.36	-0.056
200 mb	-0.11	0.38	-0.040
100 mb	-0.22	0.54	-0.059

3.

SUMMARY AND RECOMMENDATIONS

This Final Report has presented theoretical results and summarized a demonstration and sensitivity analysis of an optimal estimation approach to thermal wind profile estimation. The most important features of this approach are:

- Direct estimation of the thermal winds from radiance data without intermediate temperature profile estimation

- Thermal wind estimates which are based on error models for all data used by the algorithm

- Thermal wind estimates which minimize the mean squared estimation error.

The demonstration was based on a single set of radiance data and therefore did not support assessment of the mean-square error properties of the optimal estimation algorithm. Important conclusions which can be drawn from the demonstration are described in the following subsection. Recommendations regarding further work are presented in the concluding subsection.

3.1 CONCLUSIONS FROM THE DEMONSTRATION

Radiance gradient calculations — Since the optimal estimation approach requires radiance gradients for each channel as input data, a preprocessing step is required to estimate these gradients from radiance measurements over a grid. During the development and demonstration, more time and effort was spent than expected on radiance gradient computation issues due to the observed spatial variability of calculated radiance gradients. Our conclusion was that additional effort would be needed to develop a robust algorithm for radiance gradient calculations. A planer fit approach was adopted for radiance gradient estimation which can be adaptable to an operational environment. That adaptation will not be trivial, however, since it must deal with arbitrary data-array shapes, missing data points and quality control to avoid cloud-contaminated data.

Temperature and temperature gradient profiles — The sensitivity results clearly indicate that these are important input data to the algorithm. For an operational system, they would be derived from temperature field forecasts or based on persistence of a previous analysis field.

Whether or not temperature profile uncertainties are critical to successful application of the algorithm depends to a large extent on the form of typical temperature error profiles. As described in Section 2.4.1(iv), kernel functions are quite sensitive to bias-type temperature profile perturbations. That analysis should be extended to realistic profiles of temperature deviation.

The precise nature of the algorithm's dependence on the assumed temperature gradient profile was revealed by the new result summarized in Eq. 2.2-9. For the estimation algorithm implementation used during this investigation, the *form* of the wind profile estimate is completely determined by the initial temperature gradient profile. Processing the satellite data will scale the thermal wind corresponding to that profile so as to best fit the actual thermal wind profile in a mean-square error sense. Note, however, that this conclusion would change if a vertically varying error model for the uncertainty in the temperature gradient profile were included in the implementation (see next paragraph).

Temperature gradient error model — It was originally intended to develop and implement a model of the errors in the assumed temperature gradient profile for use in the algorithm. By the midpoint of the project, however, the extra time spent on radiance gradient calculations and the desire for a thorough sensitivity assessment, necessitated delaying that development. Without that error model, the resulting mean-square error estimates are unrealistically low and have not been discussed in this report. (Typical values are 1 m/s or less).

Preliminary work was conducted on the temperature gradient error model; completing its development requires only selection of specific functional forms for uncertainty variations with altitude and cross-correlations between deviations at different levels. Equations describing the algorithm with this model included have been developed. Their implementation is more difficult than that of the radiance gradient error model, but is a straightforward task. Completing this implementation would be a key part of further work toward operational use of the optimal estimation approach.

Channel and Algorithm Sensitivities — There are two important conclusions which can be drawn from the numerical perturbation and analytical sensitivity results. *First*, it is clear from the kernel function sensitivities that the thermal wind estimates are most sensitive to uncertainties in the kernel functions for the higher wave number channels. Therefore, an operational implementation of the optimal estimation algorithm should use data from channels sensing radiation at the *longer* wavelengths. Of course, this criterion must be balanced against the

requirement to use a sufficient number of channels to provide sensitivity to the horizontal temperature gradients within the altitude bands of interest.

Second, analytical results showed that the optimal estimation algorithm was *much less sensitive* than Ohring's method to kernel function uncertainties. While this result was based on only one case (one data set and one set of channels), it is consistent with the optimal algorithm design which minimizes a functional (Appendix G, Eq. 3.1-19) which is less sensitive to the kernel function than that used by Ohring's method (Eq. 2.3-3).

3.2 RECOMMENDATIONS

The following specific recommendations are made as a result of the experience gained in this project. The ultimate objective toward which these recommendations lead is a prototype of an operational implementation of the optimal estimation algorithm for thermal wind profiles.

- i) Complete development and implementation of an error model for the initial temperature gradient profile uncertainty.
- ii) Investigate algorithm sensitivity to realistic temperature profile uncertainties.
- iii) Use supporting satellite images to evaluate carefully the effect of clouds in the regions surrounding the locations at which the thermal wind is estimated in a representative data set.
- iv) Conduct a statistical evaluation of algorithm performance over a suitable data set.

APPENDIX A

RADIANCE DATA

This appendix contains 12 plots, 2 for each of the 6 HIRS/2 channels used in the demonstration. Each plot shows radiance data along each of 6 scan lines, either the upper (more northerly) or lower (more southerly) 6 scans spaced approximately 40 km. apart. The abscissa (scan axis location) increases in the easterly direction. Recall that the scan lines are rotated approximately 20° to the north of due east (see Fig. 2.1-2).

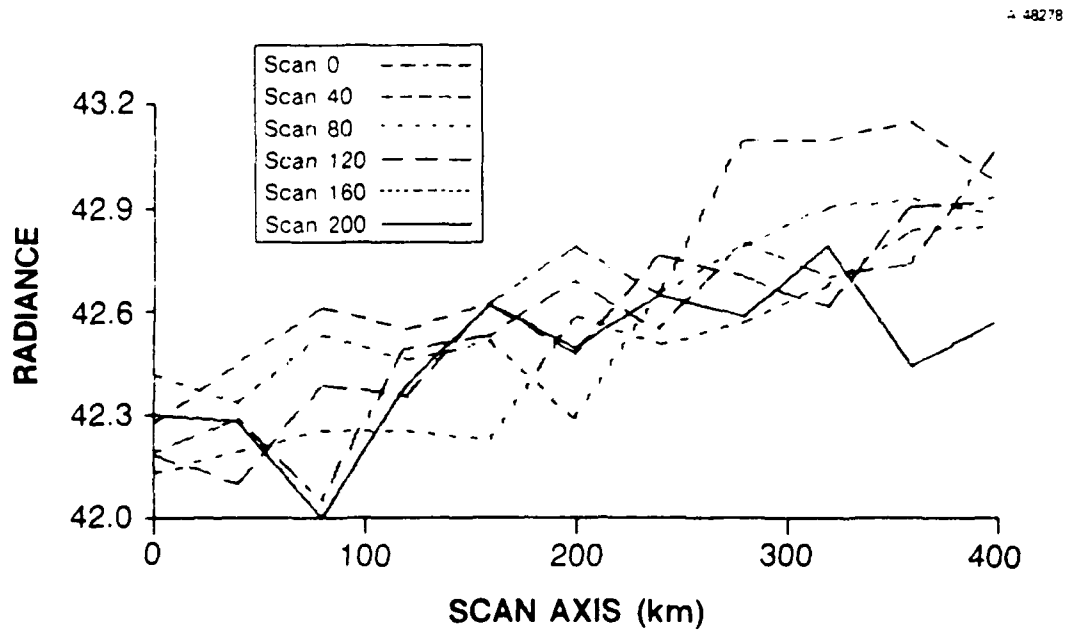


Figure A-1 Radiance Data: Channel 3-North

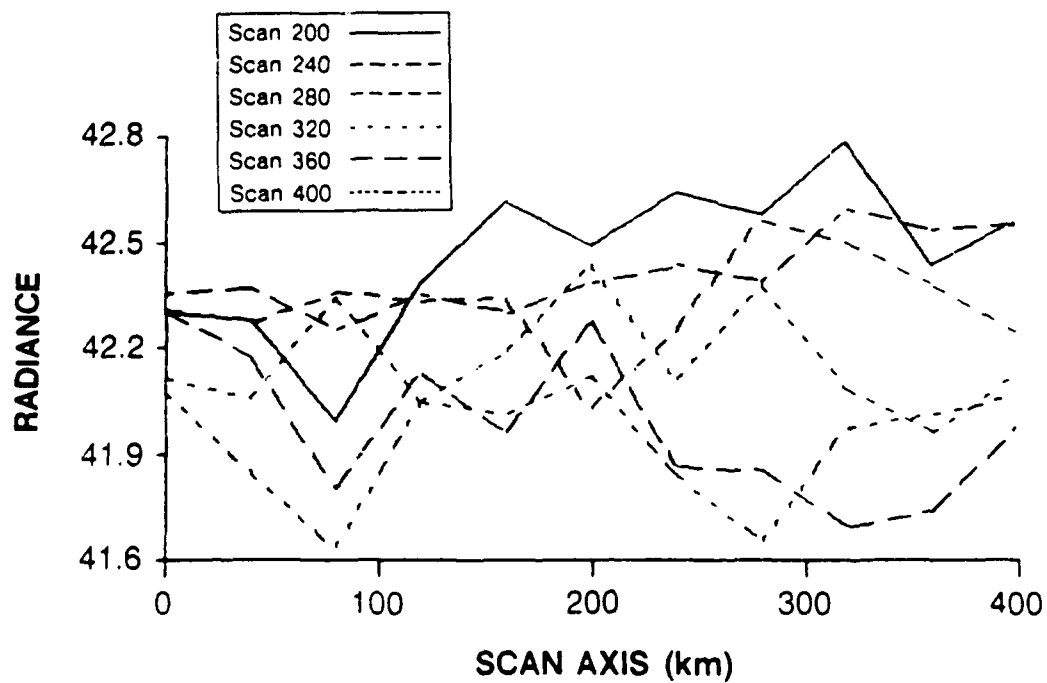


Figure A-2 Radiance Data: Channel 3-South

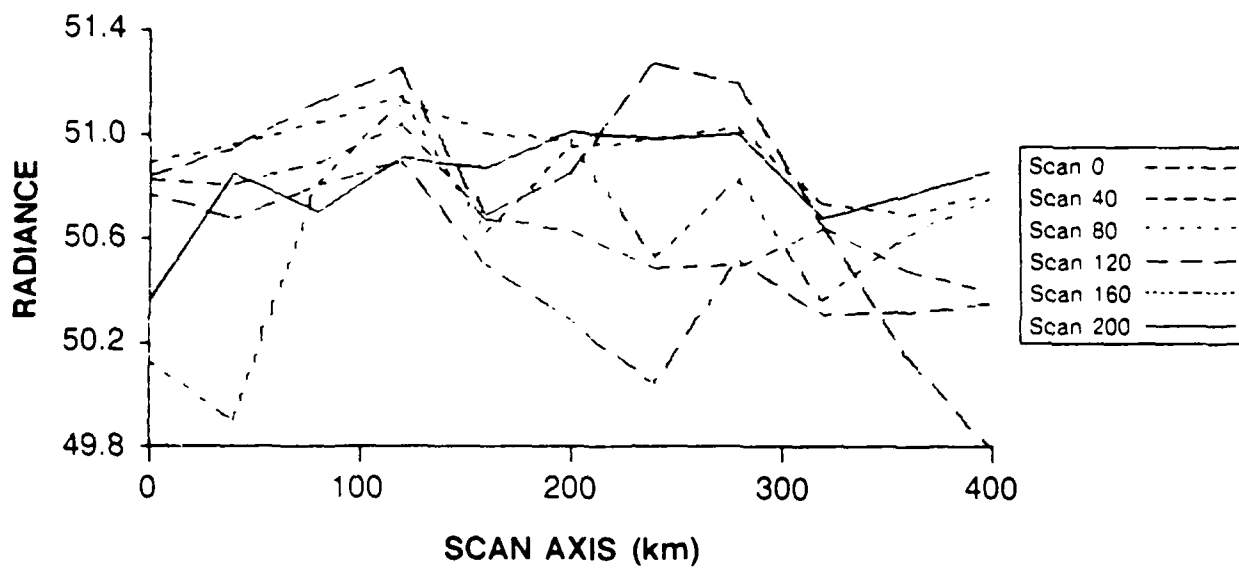


Figure A-3 Radiance Data: Channel 4-North

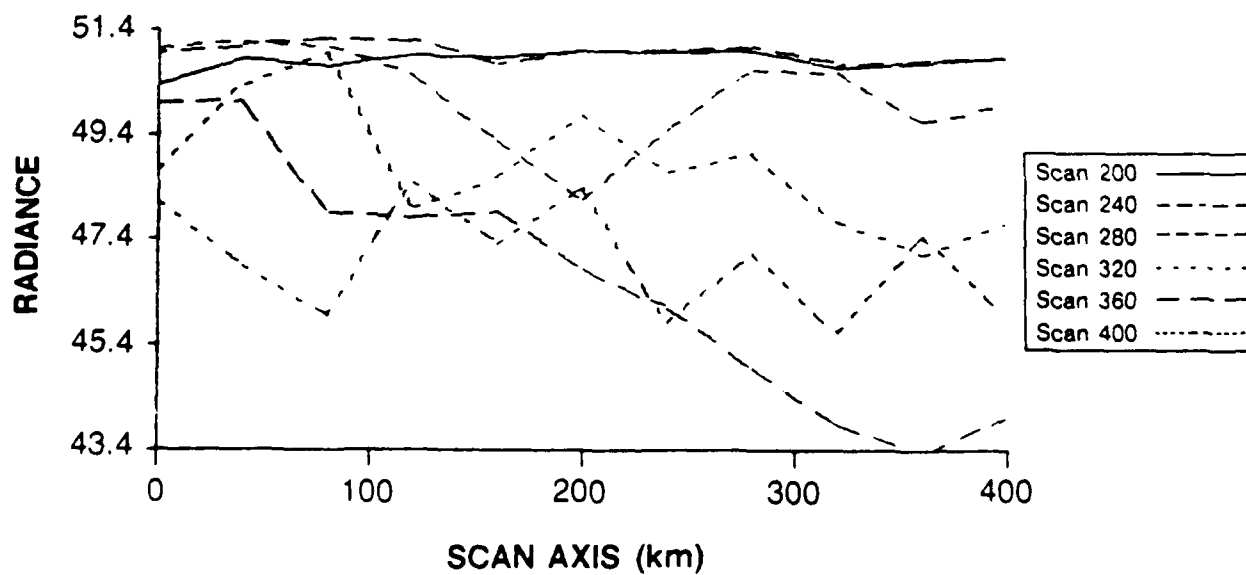


Figure A-4 Radiance Data: Channel 4-South

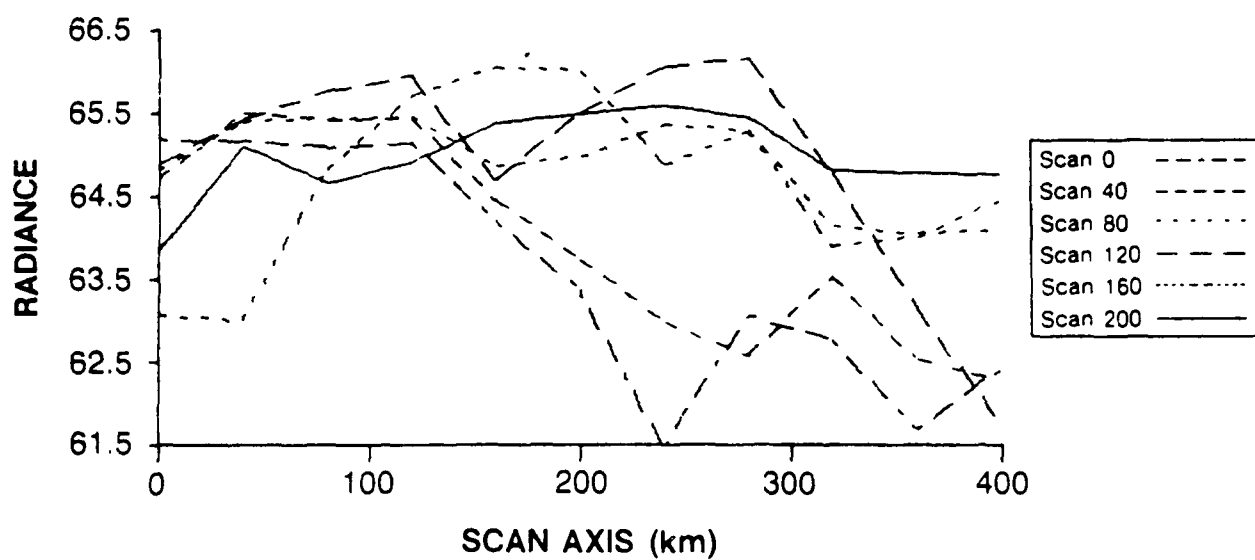


Figure A-5 Radiance Data: Channel 5-North

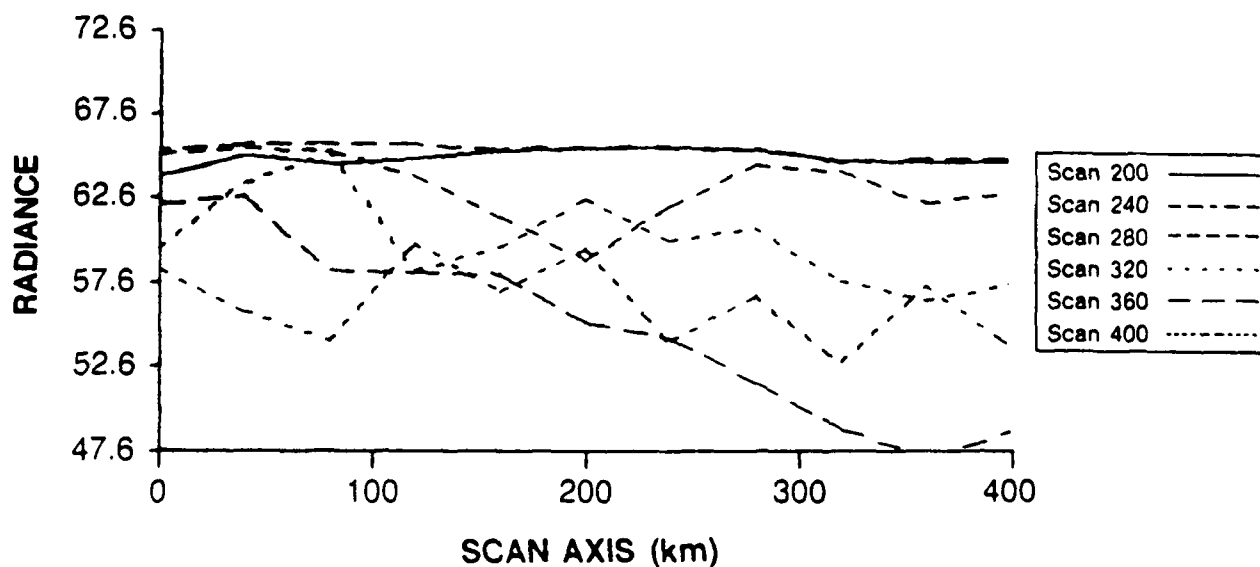


Figure A-6 Radiance Data: Channel 5-South

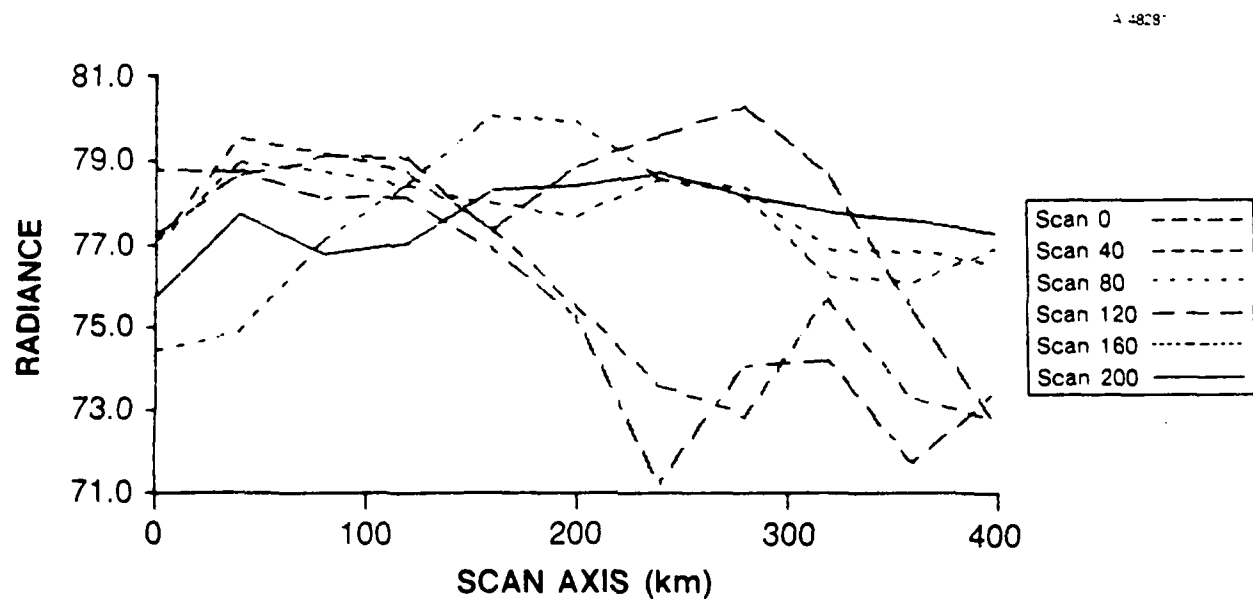


Figure A-7 Radiance Data: Channel 6-North

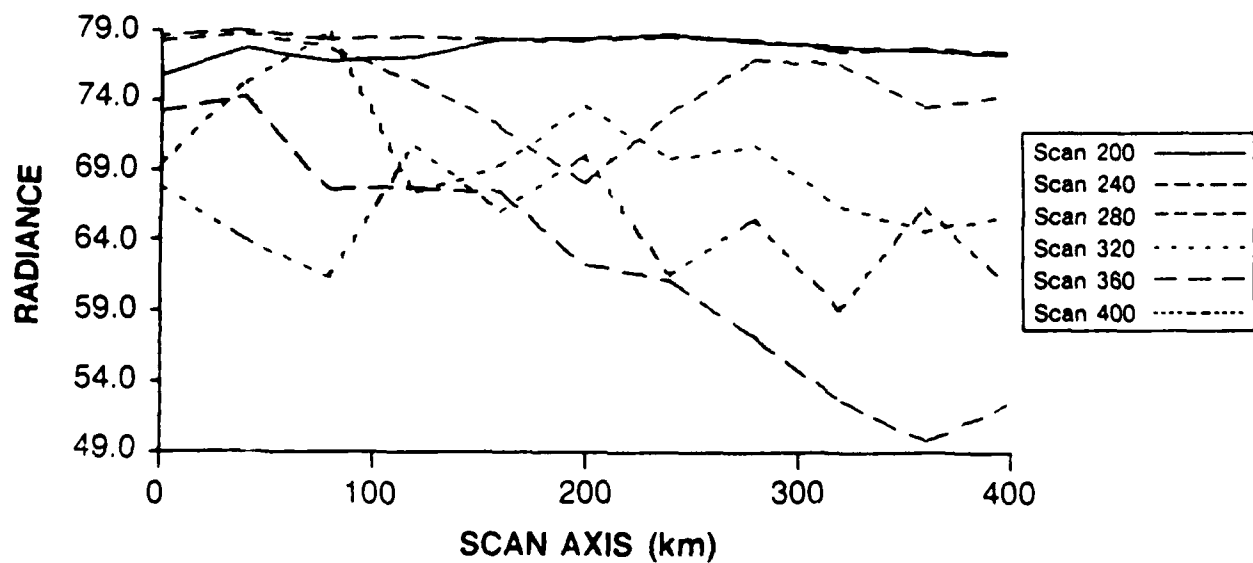


Figure A-8 Radiance Data: Channel 6-South

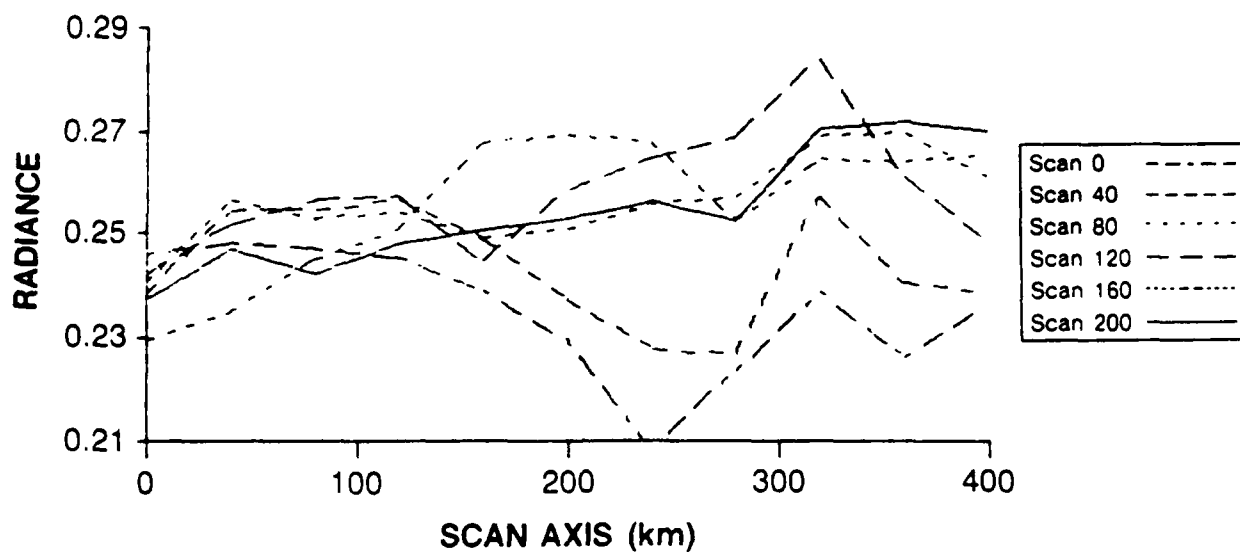


Figure A-9 Radiance Data: Channel 15-North

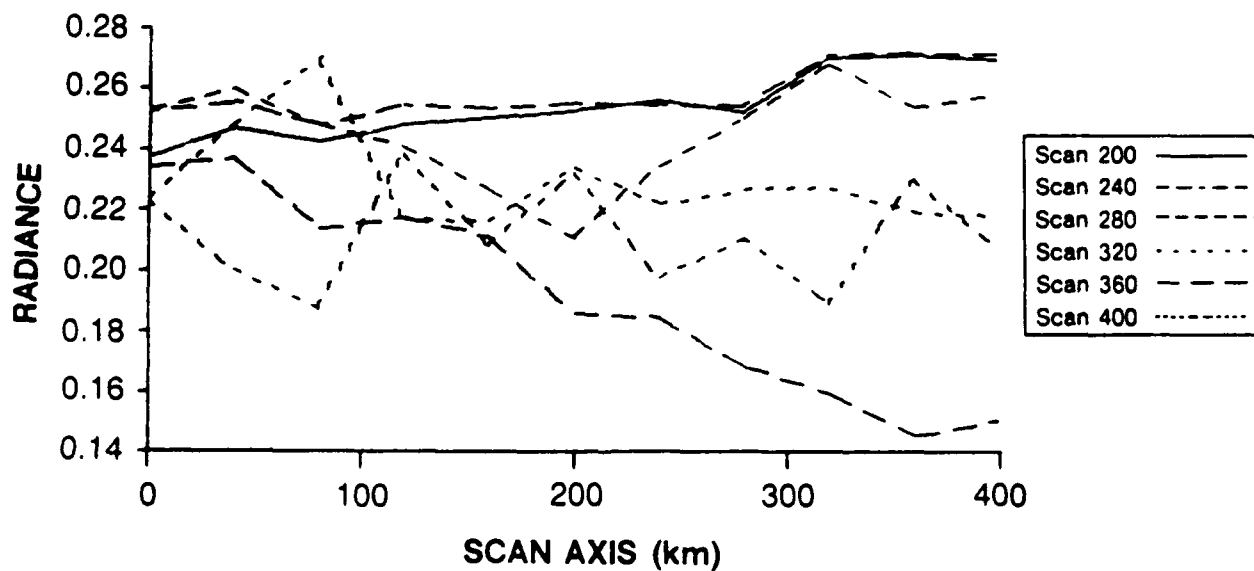


Figure A-10 Radiance Data: Channel 15-South

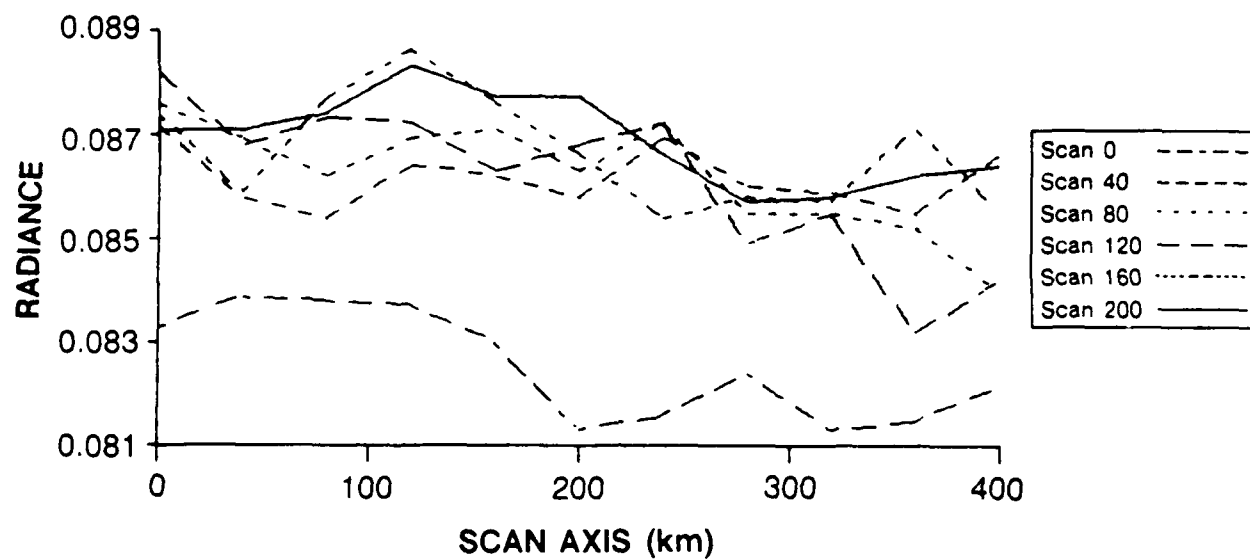


Figure A-11 Radiance Data: Channel 16-North

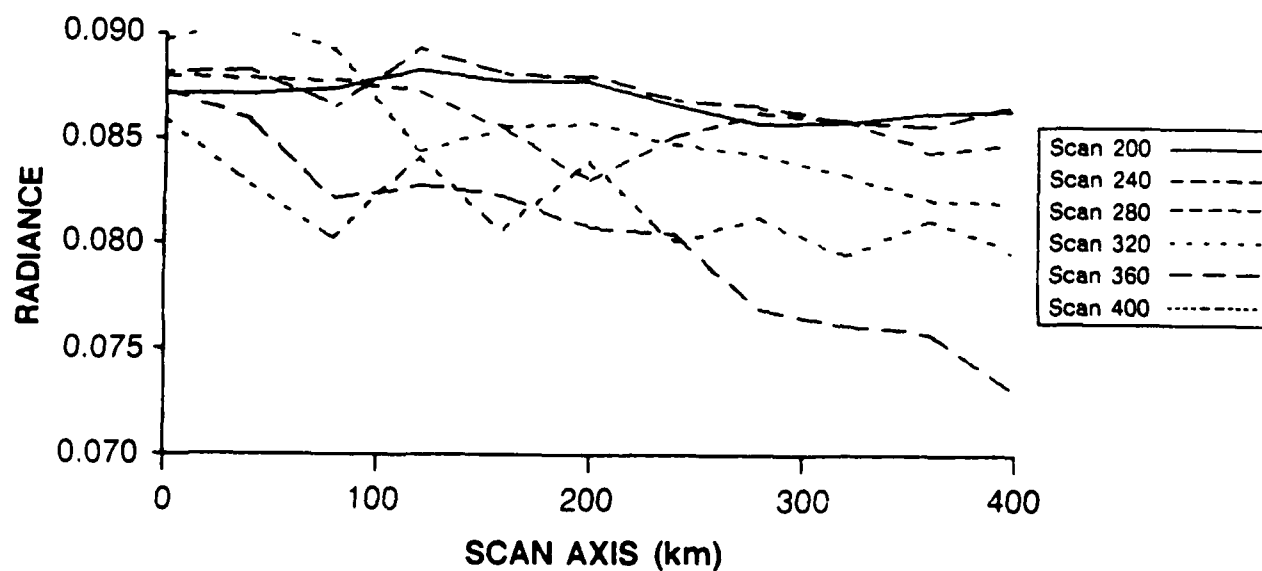


Figure A-12 Radiance Data: Channel 16-South

APPENDIX B

RADIANCE GRADIENT ESTIMATES

The six plots in this appendix show the spatial variability of the radiance gradient vectors computed from the data using a planar fit over a 7 x 7 grid centered at each of the 25 locations in each plot. Thus an adjacent pair of gradient vectors (along the same scan line or the same track) were computed from grids containing 36 common points. The plots contain *qualitative* information only; magnitudes were normalized so that the *longest* vector fit within the rectangle which represents the (approximate) 40 km x 40 km grid. The unequal scales on the north and east axes distort the true angular orientation of each vector.

Clearly, spatial variability varies significantly between channels. Channel 3 gradients show little magnitude variation while Channels 4, 5 and 6 have *about identical* large magnitude variations. Channel 15 varies widely in *both* magnitude and direction.

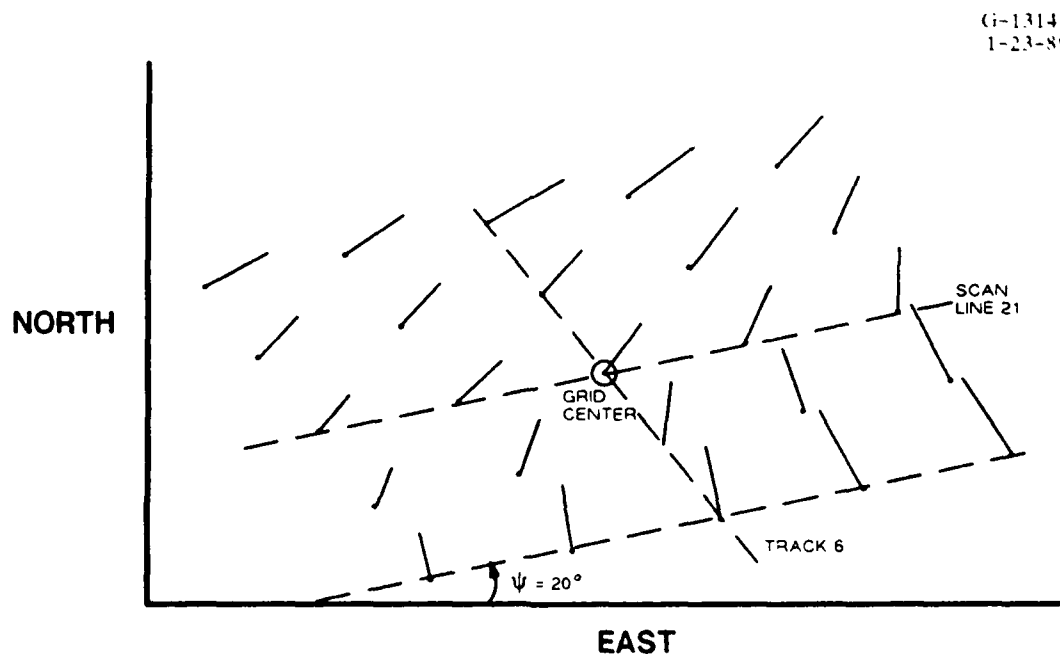


Figure B-1 Radiance Gradient Vectors: Channel 3

Gi-13146
1-23-89

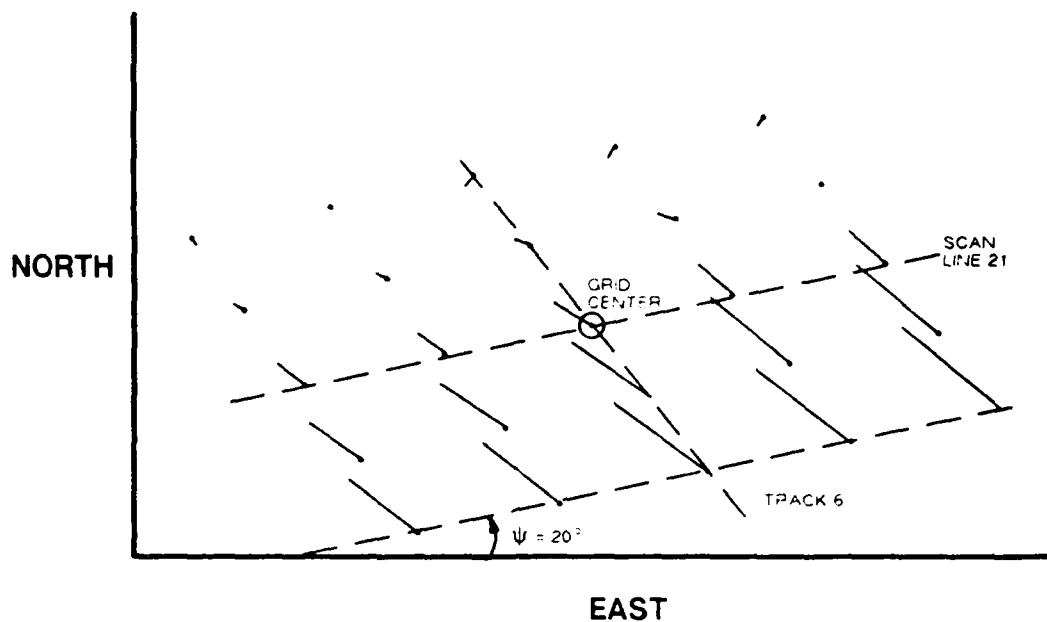


Figure B-2 Radiance Gradient Vectors: Channel 4

Gi-13147
1-23-89

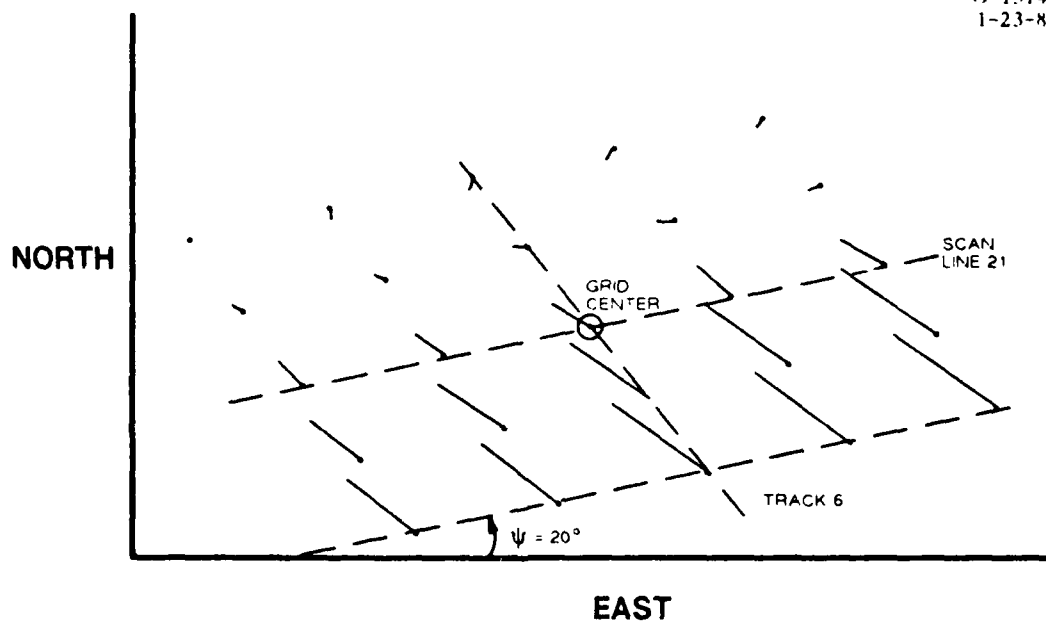


Figure B-3 Radiance Gradient Vectors: Channel 5

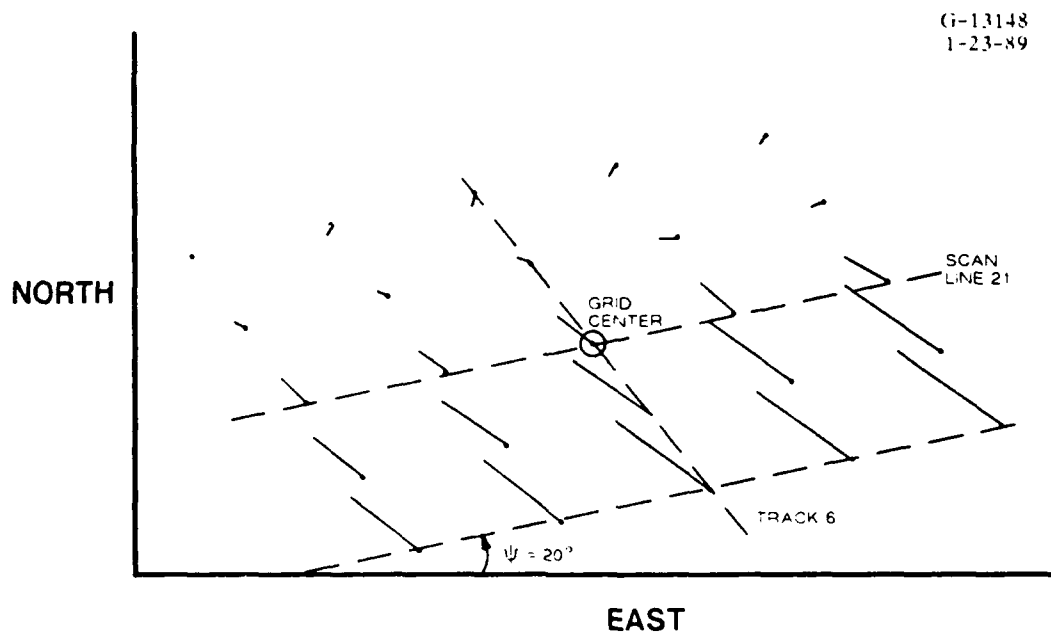


Figure B-4 Radiance Gradient Vectors: Channel 6

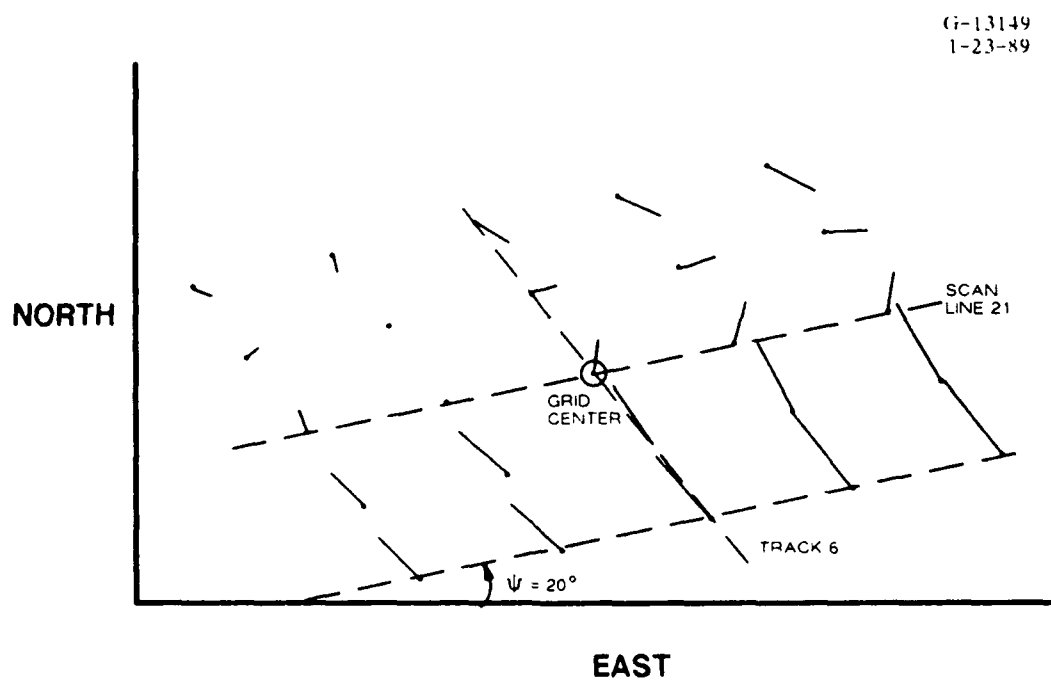


Figure B-5 Radiance Gradient Vectors: Channel 15

G-13150
1-23-89

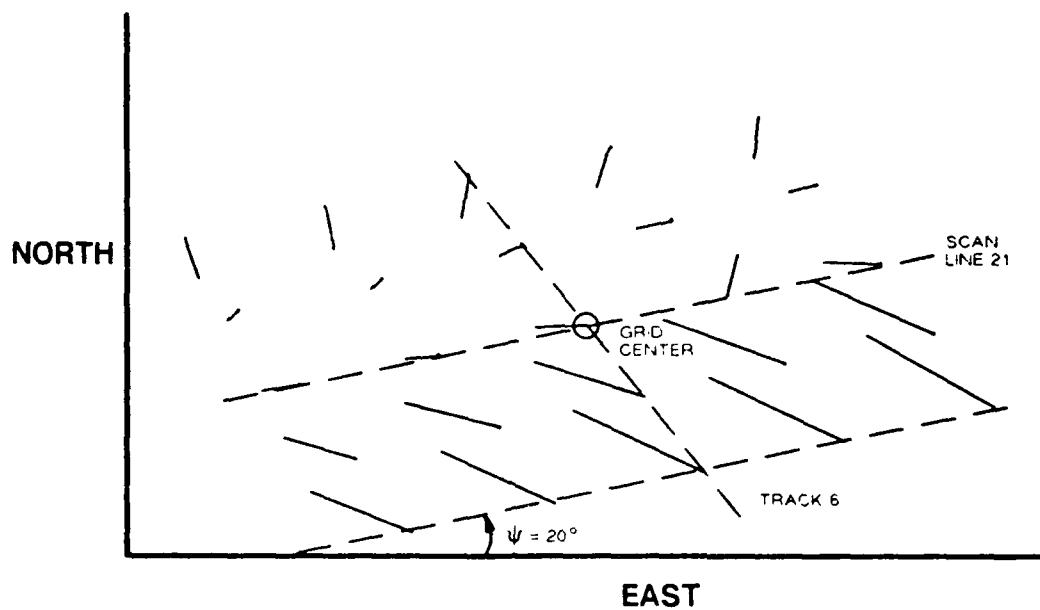


Figure B-6 Radiance Gradient Vectors: Channel 16

APPENDIX C

KERNEL FUNCTIONS

The two plots in this appendix display the kernel functions, $K_i(z)$, used in the demonstration. They were computed from the formulas presented in Appendix G using the Gibraltar measured temperature profile, Fig. 2.2-1.

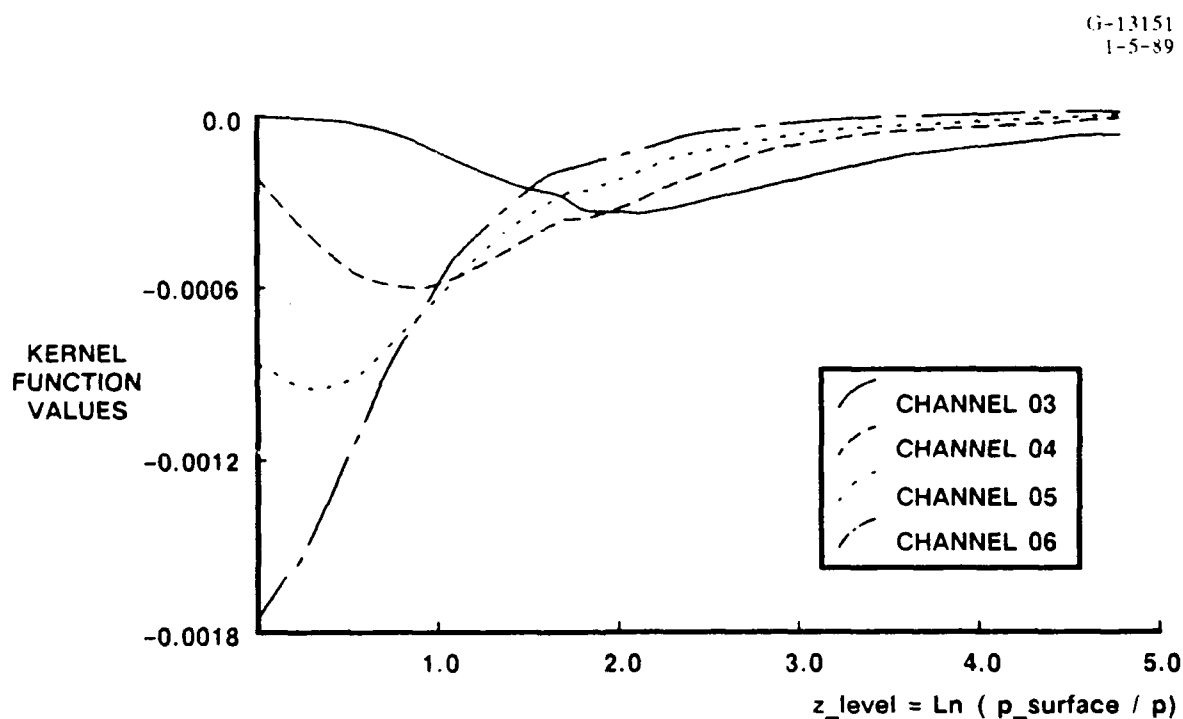


Figure C-1 Kernel Functions: Channels 3, 4, 5, 6

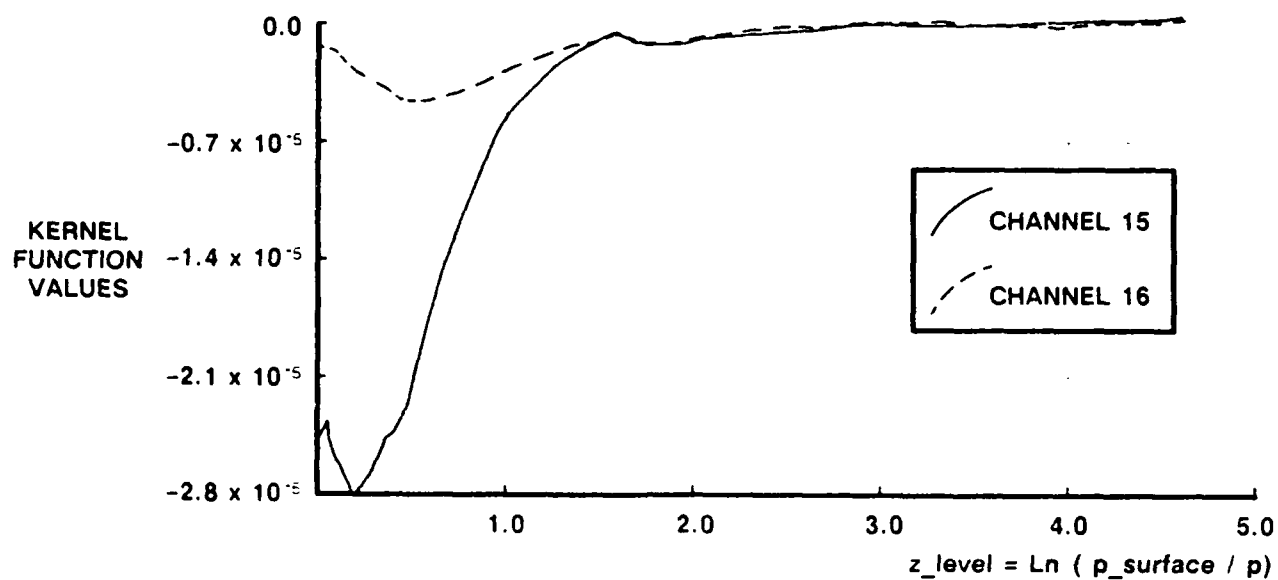


Figure C-2 Kernel Functions: Channels 15, 16

APPENDIX D

RADIANCE GRADIENTS FROM PLANAR FITS

The Interim Report, Appendix G, presented an algorithm for computing radiance gradients from the array of measured radiance values based on a cubic spline fit to the raw data field. Examining results of that algorithm using the supplied data led to concern regarding the variability of the results. In order to reduce the effects of measurement errors and modeling approximations, slopes of those bicubic spline fits were averaged over specified subsections of the complete data grid (e.g., over a 5 x 5, 7 x 7 or 9 x 9 array). Observed variability was unexpectedly large and not consistent with the assumed measurement noise models.

To avoid further loss of time while trying to resolve the issues raised by the cubic-spline results, an alternative, simpler procedure was installed based on *planar fits* to the observed data values over specified subgrids. This appendix presents the equations which implemented this procedure and, most importantly, the corresponding error model for radiance gradient estimation error consistent with that procedure. Results of this procedure, summarized in Section 2, while still showing some variability with sub-grid size and location, are much more consistent with the assumed radiance measurement error model.

D.1 PLANAR FIT ALGORITHM

The planar fit algorithm is based on the following problem formulation:

Given: $R(\underline{x}_i)$, Radiance measurements at one wavelength at position
 \underline{x}_i , $i = 1, \dots, N$, where $\underline{x}_i = (x_1, x_2)$ define a two-
dimensional regular grid

Find a plane:

$$f(\underline{x}) = a + bx_1 + cx_2 = \underline{d}^T \underline{x}' \quad (D.1-1)$$

where:

$$\underline{x}' = (1 \ x_1 \ x_2)^T \text{ and } \underline{d}^T = (a \ b \ c) \quad (\text{D.1-2})$$

Such that:

$$J(\underline{d}) = \sum_i [R(\underline{x}_i) - f(\underline{x}_i)]^2 \quad (\text{D.1-3})$$

is minimized.

This straightforward least-squares problem has the well known solution

$$\underline{d} = A^{-1} \underline{e} \quad (\text{D.1-4})$$

in which the 3x3 matrix A and the vector \underline{e} are as follows.

$$A = \sum_{i=1}^N \begin{pmatrix} 1 & x_{1i} & x_{2i} \\ x_{1i} & x_{1i}^2 & x_{1i}x_{2i} \\ x_{2i} & x_{1i}x_{2i} & x_{2i}^2 \end{pmatrix} \quad (\text{D.1-5})$$

$$\underline{e} = \sum_i R(\underline{x}_i) \underline{x}'_i \quad (\text{D.1-6})$$

Equation D.1-1 defines a plane whose gradient, (b c), is an estimate of the radiance gradient at the center of the data grid expressed in the data grid coordinates. These coordinates were along the track and scan axes (x_1 and x_2 respectively) of the satellite data collection path. Since the wind profile estimation will be conducted in an (East, North) coordinate system, the above gradient vector is rotated by the following transformation:

$$T(\psi) = \begin{pmatrix} \sin \psi & \cos \psi \\ -\cos \psi & \sin \psi \end{pmatrix} \quad (\text{D.1-7})$$

where ψ = counter-clockwise angle from the East axis to the scan axis. In this formulation, it is assumed that the track and scan axes are orthogonal. The actual track and scan axes were slightly non-orthogonal, with deviation up to 2° in some parts of the data collection region. The orthogonal approximation will cause a very slight error in the direction and, to an even smaller

extent, magnitude of calculated radiance gradients. These errors are far below the noise level of the radiance gradient estimates.

Software was written and tested implementing Eqs. D.1-4 - D.1-7 for user-selected square subgrids located anywhere within the complete 11 x 11 grid selected for analysis. Results are presented and discussed in Section 2.1.

D.2 PLANAR FIT ERROR MODEL

The error model for radiance gradient estimates computed by the above procedure is derived from two sources: the measurement error model for the radiance data and the *modeling error* implied by the planar fit. To present the error model in a compact form, the radiance gradient estimates are written

$$\hat{\nabla} \mathbf{R}^T = \mathbf{H} \mathbf{R} \quad (\text{D.2-1})$$

where

$$\mathbf{H} = \begin{pmatrix} 0 \\ 0 \end{pmatrix}^T \mathbf{T}(\psi) \quad (\mathbf{X} \mathbf{X}^T)^{-1} \mathbf{X} \quad (\text{D.2-2})$$

$$\mathbf{R} = [\mathbf{R}(\mathbf{x}_1) \ \mathbf{R}(\mathbf{x}_2) \ \dots \ \mathbf{R}(\mathbf{x}_N)]^T \quad (\text{D.2-3})$$

and

$$\mathbf{X} = [\mathbf{x}'_1 \ \mathbf{x}'_2 \ \dots \ \mathbf{x}'_N] \quad (\text{D.2-4})$$

Now,

$$\mathbf{R} = \mathbf{R}_T + \tilde{\mathbf{R}} \quad (\text{D.2-5})$$

where the subscript T indicates the vector of *true* radiance values and the last term is the measurement error vector. Therefore

$$\hat{\nabla} \mathbf{R}^T = \mathbf{H} \mathbf{R}_T + \mathbf{H} \tilde{\mathbf{R}} \quad (\text{D.2-6})$$

and

$$\hat{\nabla} \mathbf{R}^T = (\hat{\nabla} \mathbf{R}^T)_T + \tilde{\nabla} \mathbf{R}^T \quad (\text{D.2-7})$$

where in Eq. D.2-7 the gradient is expressed as a sum of the *true* gradient vector plus the error term whose covariance will define the error model. If the true radiance values actually do, in fact, lie in a plane, then there is no *modeling error* (referred to earlier) and the first terms on the right hand sides of Eqs. D.2-6 and 7 are equal. In this case, the error model is

$$\Gamma = \text{Cov}(\tilde{\nabla}R) = H \text{Cov}(\tilde{R})H^T \quad (\text{D.2-8})$$

Results presented in this report are based on the assumption that modeling error can be neglected (so that Eq. D.2-8 holds).

The covariance of the radiance data vector error, \tilde{R} , in this equation is exactly the same as the Φ matrix discussed in Section 2 of the Interim report. All analysis results reported in this document used a Φ matrix based on parameter values (measurement error variances and correlation distances) stated in that report.

APPENDIX E

PROOF OF ALGORITHM VALIDITY

The objective of this proof is to demonstrate the *consistency* of wind profile estimates, i.e., that in the absence of noise and numerical error, the algorithm will produce the correct thermal wind estimates. A special case of consistency was shown earlier in the Interim Report (Appendix G). Though the simple linear form assumed for the temperature field in that special case was useful in the simulation-based check of the wind profile estimation algorithm, it was, in fact, *not required* in the analytical proof that wind estimates converge to the true thermal wind in the limit as the radiance gradient error covariance matrix Γ approaches the zero matrix.

The critical step in the proof is recognition that, for any continuously differentiable temperature field, $T(y,z)$ (since we are presently examining only the east component of the thermal wind, the x dependence is not indicated), the following relationship holds:

$$\underline{g} = \underline{\theta} \quad (E-1)$$

where both sides of Eq. E-1 were defined in Section 2.2.1. Note that distinct symbols are required on the two sides of Eq. E-1 because \underline{g} is based on radiance measurements whereas $\underline{\theta}$ is based on the assumed temperature gradient.

To prove that

$$\lim_{\Gamma \rightarrow 0} \underline{\hat{u}} = \underline{\hat{u}}^0 \quad (E-2)$$

it is sufficient, via Eq. 2.2-7 and 2.2-8, to prove that

$$\lim_{\Gamma \rightarrow 0} \underline{g}^T \underline{P}^{-1} \underline{\theta} = 1 \quad (E-3)$$

i.e., that

$$\lim_{\Gamma \rightarrow 0} \underline{\theta}^T \underline{P}^{-1} \underline{\theta} = 1 \quad (E-4)$$

by Eq. E-1.

The remainder of the proof follows verbatim that for the linearly varying temperature field. Applying the Sherman-Morrison formula (Ref. 3) to Eq. 2.2-4, P^{-1} is given by

$$P^{-1} = \Gamma^{-1} - \left(\frac{1}{1 + \underline{\theta}^T \Gamma^{-1} \underline{\theta}} \right) \Gamma^{-1} \underline{\theta} \underline{\theta}^T \Gamma^{-1} \quad (E-5)$$

Now, the left side of Eq. E-4 can be expressed as

$$\lim_{\Gamma \rightarrow 0} (\underline{\theta}^T P^{-1} \underline{\theta}) = \lim_{\Gamma \rightarrow 0} \left\{ \underline{\theta}^T \left[\Gamma^{-1} - \left(\frac{1}{1 + \underline{\theta}^T \Gamma^{-1} \underline{\theta}} \right) \Gamma^{-1} \underline{\theta} \underline{\theta}^T \Gamma^{-1} \right] \underline{\theta} \right\} \quad (E-6)$$

which becomes

$$\lim_{\Gamma \rightarrow 0} (\underline{\theta}^T P^{-1} \underline{\theta}) = \lim_{\Gamma \rightarrow 0} \left\{ \left(1 - \frac{\underline{\theta}^T \Gamma^{-1} \underline{\theta}}{1 + \underline{\theta}^T \Gamma^{-1} \underline{\theta}} \right) \underline{\theta}^T \Gamma^{-1} \underline{\theta} \right\} = 1 \quad (E-7)$$

Thus the thermal wind estimate $\hat{\underline{u}}$ approaches the true value \underline{u}^0 as the radiance gradient error covariance matrix approaches zero. This result not only provides theoretical justification for the algorithm, but also enables a check for vertical discretization and numerical integration errors.

APPENDIX F

SENSITIVITY EQUATIONS

Although the most important results regarding robustness of the new optimal estimation algorithm are based on actual algorithm executions using perturbed parameter values, sensitivity equations based on linearized equations provide important theoretical results in a cost-efficient manner. These linearized sensitivity equations are presented in this appendix for both the optimal estimation approach and for Ohring's method. Numerical results based on these equations are presented in Section 2.4 along with algorithm perturbation results.

F.1 SENSITIVITY OF THE OPTIMAL ESTIMATION ALGORITHM

Sensitivity equations can be derived for any of the algorithm parameters or data values. This section presents equations only for the sensitivity with respect to values of the kernel functions, $K_j(z)$, because those functions depend on the most important input information, namely the nominal temperature profile, the Planck functions, and the absorption profile (see Appendix G). Sensitivity equations with respect to the assumed temperature gradient profile could be derived in a similar manner.

There is one important technical point in the following derivation that should be noted. The kernels, $K_j(z)$ are functions of z , so a functional analysis viewpoint (using a Frechet derivative, for example) should be used to express sensitivity with respect to the "kernel functions". As an alternative, simpler approach, the following derivation is based on an approximately uniform fractional perturbation throughout $[0, z_T]$.

The sensitivity equations are based on a logarithmic derivative of the estimates, \hat{u} , (Eq. 2.2-2) with respect to each of the kernel function components. So, there is a $n \times m$ matrix of sensitivity functions defined by:

$$S = \left[\frac{\partial \ln \hat{u}(z_i)}{\partial \ln K_j} \right] \quad (F.1-1)$$

The ij^{th} element of S is given by

$$S_{ij} = -\frac{R}{f} \frac{K_j}{u_T(z_i)} \frac{\partial c(z_i)^1}{\partial K_j} \underline{g} \quad \begin{matrix} i = 1, \dots, n \\ j = 1, \dots, m \end{matrix} \quad (\text{F.1-2})$$

By extensive but straightforward manipulation, the following formula for the complete sensitivity matrix results:

$$S = -\frac{R}{f} a_T U_D \left(\underline{t}_2 \underline{t}_1^T - \beta C \right) K_D \quad (\text{F.1-3})$$

where

$$a_T = \int_0^{z_T} \frac{\partial T}{\partial y} (\zeta) d\zeta \quad (\text{F.1-4})$$

$$U_D = \text{Diag} \{ (1/\dot{u}(z_i)) \} \quad (\text{F.1-5})$$

$$\underline{t}_1 = P^{-1} \underline{g}, \quad \underline{t}_2 = \underline{a} - C \underline{\theta} \quad (\text{F.1-6})$$

(C is given by Eq. 2.2-3 and a by Eq. 2.2-6),

$$\beta = \underline{\theta}^T \underline{t}_1 \quad (\text{F.1-7})$$

and

$$K_D = \text{Diag} (k_j) \quad (\text{F.1-8})$$

where the diagonal elements are constants,

$$k_j = \frac{1}{z_T} \int_0^{z_T} |K_j(\zeta)| d\zeta \quad (\text{F.1-9})$$

F.2 SENSITIVITY OF OHRING'S METHOD

The approach used to develop a sensitivity equation for Ohring's method parallels that in the previous section, with a few necessary modifications. Since Ohring's method is formulated to yield *layer* estimates (Eq. 2.3-1) we define the vector of summed estimates analogous to that produced by the optimal estimation approach as follows:

$$\hat{\underline{u}}_O = L \hat{\underline{u}}_J \quad (\text{F.2-1})$$

where \hat{u}_I is the vector of estimates calculated using Eq. 2.3-1, and the matrix L has elements

$$\rho_{ij} = \begin{cases} 1 & i \geq j \\ 0 & i < j \end{cases} \quad (F.2-2)$$

So, the sensitivity matrix for Ohring's method is

$$S = -(R/f) U_O L (t_{1O} t_{2O}^T - \beta_O C_O) K_D \quad (F.2-3)$$

where U_O is a diagonal matrix analogous to Eq. F.1-5 but containing Ohring's summed estimates, u_{iO} , and K_D is again given by Eqs. F.1-8 and F.1-9. The other terms are:

$$t_{1O} = \Delta z - C_O \underline{k} \quad (F.2-4)$$

where

$$\Delta z_i = z_{i+1} - z_i, \quad i = 1, \dots, n, \quad (F.2-5)$$

$$\underline{k} = \int_0^{z_T} \underline{K}(\xi) d\xi, \quad (F.2-6)$$

$$t_{2O} = M^{-1} \underline{R}_y \quad (F.2-7)$$

where M is given by Eq. 2.3-6,

$$\beta_O = \underline{k}^T t_{2O}, \quad (F.2-8)$$

and finally,

$$C_O = \begin{pmatrix} \underline{c}_1^T \\ \vdots \\ \underline{c}_n^T \end{pmatrix} \quad (F.2-9)$$

where \underline{c}_i , $i = 1, \dots, n$, are given by Eq. 2.3-5.

The similar *forms* of the Ohring and optimal estimate sensitivity matrices should not be surprising because of the outwardly similar form of the estimators. That their *numerical* values are much different is shown in Section 2.4.

•

•

APPENDIX G

Technical Information Memorandum

TASC
THE ANALYTIC SCIENCES CORPORATION

To: AFGL/LY Hanscom AFB, MA 01731-5320 Attn: Dr. Tom Kleespies	TIM No. 5547-1
	Date: 4 April 1988
	Contract No. F19628-87-C-0248
	From: KBMacNichol SRFinch
Program: Wind Profile Estimation	Approval: CLMedler
Subject: DIRECT STATISTICAL THERMAL WIND ESTIMATION PROCEDURE - INTERIM REPORT	

FOREWORD

Research efforts under the referenced contract have focused on developing a practical approach for estimating thermal wind profiles directly from satellite radiance data. The approach, if successful, can be adapted for operational use with the addition of at least one single level wind measurement to yield an estimate of the vertical wind profile. In this interim report the baseline algorithm, incorporating a statistical model of satellite radiance gradient errors, is reviewed and preliminary simulation results are presented. A final report, due in December 1988, will provide the final algorithm and demonstration results.

TABLE OF CONTENTS

	<u>Page</u>
1. INTRODUCTION	G-1
2. MODEL FORMULATION	G-3
2.1 Specification of the Kernel Functions	G-3
2.2 Radiance Gradient Error Model	G-6
3. ALGORITHM DEVELOPMENT	G-12
3.1 The Baseline Algorithm	G-12
3.2 Iterations and Steady-State	G-18
4. SUPPORTING DATA FOR ALGORITHM DEMONSTRATION	G-25
4.1 Radiance Data	G-25
4.2 Rawinsonde Data	G-28
4.3 Temperature Field Data	G-29
5. BASELINE SIMULATION RESULTS	G-33
6. SUMMARY	G-39
REFERENCES	R-1
APPENDIX A TRANSFORMING RADIANCE MEASUREMENTS INTO RADIANCE GRADIENTS	A-1

INTRODUCTION

The need for determining wind fields in data-sparse regions has prompted several investigations into the use of satellite radiance data for wind profile determination. References 1, 2, and 3 describe methods which compute thermal wind directly from radiance measurements, avoiding the error-prone path of first determining temperature profiles (the inversion problem) and then computing thermal wind via the thermal wind equation. The present effort extends previous work (notably Ref. 1) by formulating an optimal estimation algorithm based on a statistical error minimization criterion. Statistical models of error sources in the data collection and data analysis processes are an integral part of the formulation. In this report, only the radiance gradient error model has been defined. The algorithm structure can accommodate error models for temperature gradients and frequency-dependent weighting functions as well. Descriptions of these models will appear in the final report.

Background, motivation, and discussions of previous work related to this effort are found in Ref. 4. The work tasks, as outlined in Ref. 4, are listed in Figure 1-1. Progress achieved to-date for each task is indicated by shaded bars.

The remainder of this report is organized as follows. Section 2 provides a description of the satellite weighting function models used in this effort. A description of the radiance gradient error model is also provided. Section 3 details the baseline algorithm formulation including all

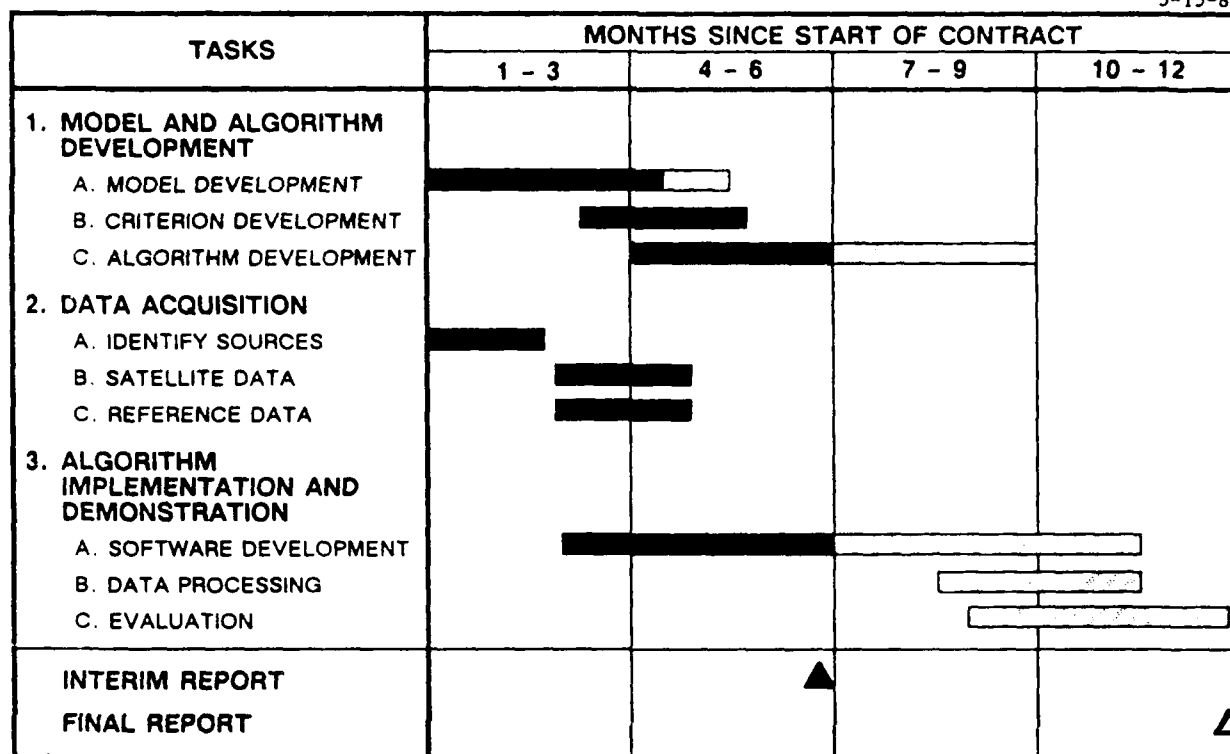


Figure 1-1 Progress in Development of the Statistical Wind Profile Estimator

assumptions and equations. An extension to the baseline algorithm, based on a closed-form iterative approach, is described as well. In Section 4 the data to be used in producing preliminary demonstration results are identified and described, and simulation results for algorithm and software verification are presented and discussed in Section 5. A summary is provided in Section 6.

MODEL FORMULATION

For use during algorithm development and testing, parametric forms for the baseline kernel functions and the radiance gradient error model have been defined. In addition to their utility during algorithm checkout and demonstration, these models provide the means to determine estimate sensitivities to various model components. The parametric models for the kernel functions and the radiance gradient error model are described in Sections 2.1 and 2.2, respectively.

2.1 SPECIFICATION OF THE KERNEL FUNCTIONS

As will be discussed in Section 3 the theoretical radiance measured by the satellite radiometer in each specific channel is computed from the radiative transfer equation involving a vertical integral of a product of temperature and a frequency-dependent kernel function. The kernel or weighting function $K_i(z)$ associated with the i^{th} channel of the satellite radiometer is given in Ref. 4 as

$$K_i(z) = \frac{dB_i}{dT} [T_o(z)] \frac{d\tau_i}{dz}(z) \quad (2.1-1)$$

where B_i is the Planck function at the i^{th} frequency or wave number, T is temperature, z is an altitude variable, $T_o(z)$ is a given nominal temperature profile, and τ_i is the transmittance function at the i^{th} frequency.

The Planck function for a discrete wave number ν_i is given as

$$B_i(T) = \frac{c_1 \nu_i^3}{\exp(c_2 \nu_i / T) - 1} \quad (2.1-2)$$

where B is black body radiance in $\text{W m}^{-2} \text{sr}^{-1} \text{cm}$, T is absolute temperature (deg K), and c_1 and c_2 are constants ($c_1 = 1.1911 \times 10^{-8} \text{ W m}^{-2} \text{sr}^{-1} \text{cm}^4$ and $c_2 = 1.439 \text{ cm deg}$). Differentiating Eq. 2.1-2 with respect to temperature yields

$$\frac{dB_i}{dT} = \frac{c_1 c_2 \nu_i^4 \exp(c_2 \nu_i / T)}{T^2 [\exp(c_2 \nu_i / T) - 1]^2} \quad (2.1-3)$$

Values for this term at each wave number of interest are computed using the nominal temperature profile.

The transmittance $\tau_i(z)$ at wave number ν_i from altitude z to the "top" of the atmosphere is a complex function of atmospheric constituents. In this effort the vertical derivatives of τ_i needed to evaluate the kernel functions (Eq. 2.1-1) are represented by analytic expressions fit to published curves. Plots of the derivative function

$$\tau'_i = \frac{d\tau_i}{dp^{2/7}} \quad (2.1-4)$$

for the HIRS/2 are contained in Figures 2.1-1 and 2.1-2 (see Ref. 5). Parameter values a, b, c at each ν_i for which the following functional form

$$\phi(p) = a p^b \exp(-cp) \quad (2.1-5)$$

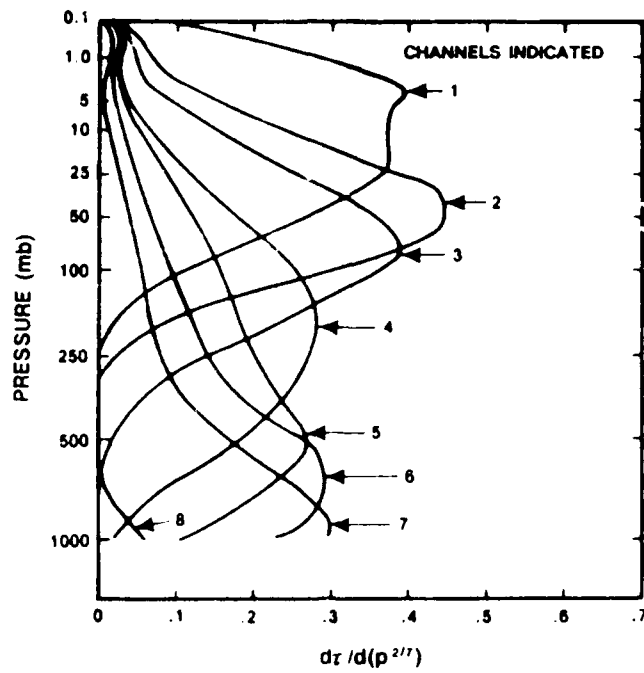


Figure 2.1-1 Vertical Derivatives of Transmittance Functions, Channels 1-8

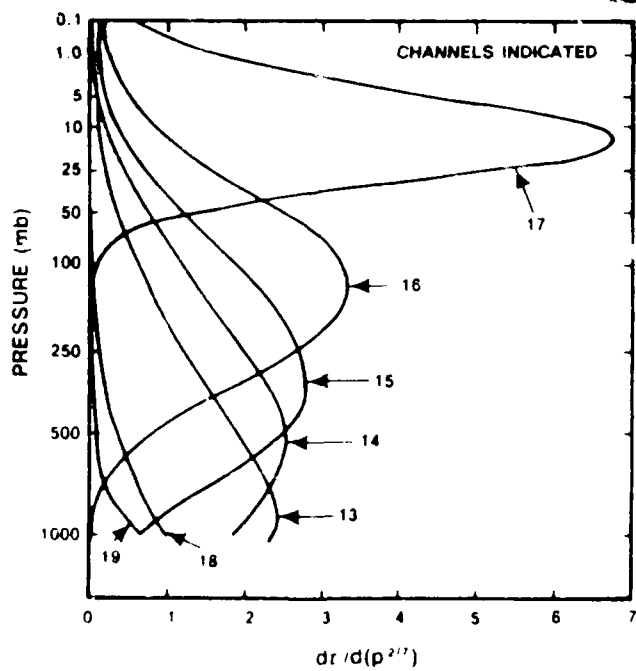


Figure 2.1-2 Vertical Derivatives of Transmittance Functions, Channels 13-19

best fits Eq. 2.1-4 have been determined. The best fit criterion used is the quadratic function

$$\sum_{j=1}^n [\tau_i(p_j) - \phi(p_j)]^2 \quad (2.1-6)$$

where the n pressure levels are preselected. Sample fits are illustrated in Figure 2.1-3. As a rule, the fit is best for roughly bell-shaped curves, e.g. those corresponding to channels 2 and 15. The fit for the curve corresponding to channel 6 is improved by weighting points in the 250-1000 mb range more heavily, as illustrated by the dotted line. From these parametric forms, it follows that

$$\frac{d\tau_i}{dz} = \frac{d\tau_i}{d(\ln p)} = \left(\frac{2}{7} a\right) p^{(b+\frac{2}{7})} \exp(-cp) \quad (2.1-7)$$

The product of Eqs. 2.1-3 and 2.1-7 is, for each frequency, the desired kernel function.

2.2 RADIANCE GRADIENT ERROR MODEL

In this section a matrix expression for the frequency-dependent radiance gradient error model is derived. Published values of HIRS/2 radiance measurement error standard deviations are directly incorporated using a prescribed analytic measurement error covariance model. The geometry of the gradient computation is contained in the gradient error model by modeling the specific bicubic spline derivative operations made on the radiance data. For each frequency, radiance measurements form a scalar-valued function r defined on a planar, N_x by N_y grid as pictured in Figure 2.2-1. A standard

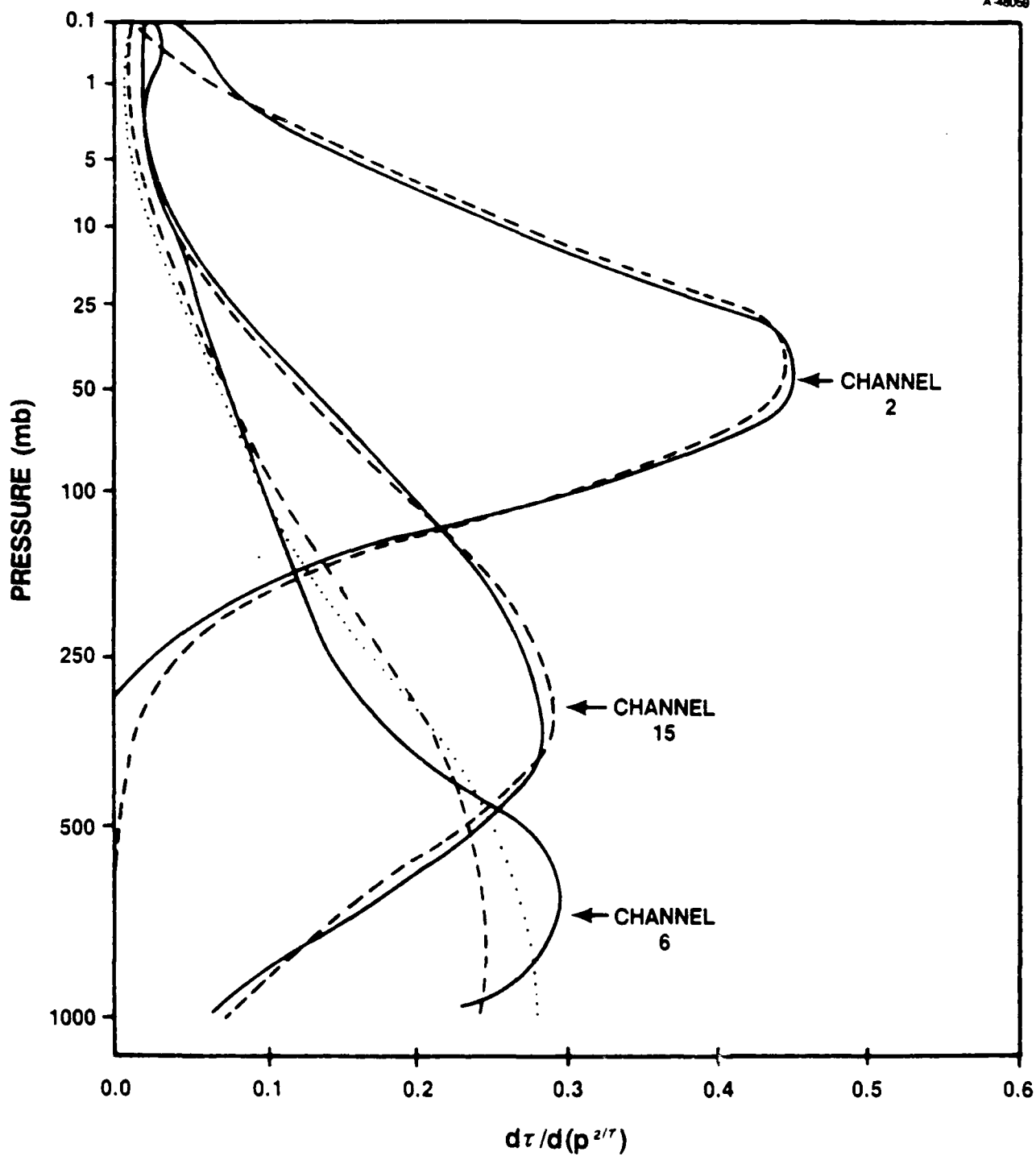


Figure 2.1-3 Vertical Derivatives of Transmittance Functions (Solid Lines) and Parametric Fits (Broken Lines)

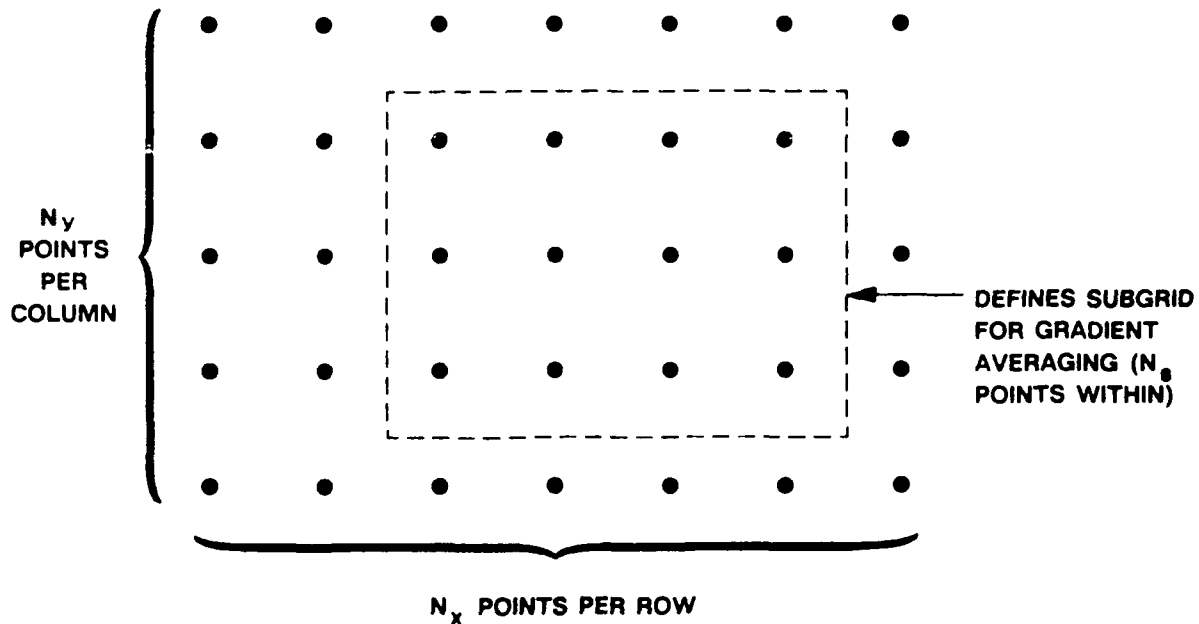


Figure 2.2-1 Radiance Grid

bicubic spline routine yields radiance gradients, for each frequency, at any preselected grid point. It is shown in Appendix A that the radiance gradient at grid point (j,k) is a linear transformation of the vector \underline{r} of all radiance measurements over the grid, i.e.

$$\underline{\nabla r}_{j,k} = F_{j,k} \underline{r} \quad (2.2-1)$$

where

$$\underline{r} = (r_{1,1} \ r_{1,2} \ \dots \ r_{1,N_x} \ r_{2,1} \ r_{2,2} \ \dots \ r_{2,N_x} \ \dots \ r_{N_y,1} \ r_{N_y,2} \ \dots \ r_{N_y,N_x})^T \quad (2.2-2)$$

and $F_{j,k}$ is a certain 2 by $(N_x * N_y)$ matrix which, as indicated notationally, is dependent on the gridpoint. Equation 2.2-1 provides an analytically convenient form for deriving the

radiance gradient error model given a radiance measurement error model, especially in the case in which spatial correlations are modeled. Since Eq. 2.2-1 yields the gradient at one point, an averaging procedure has been defined to reduce data errors and smooth results, if necessary. The average radiance gradient over a prespecified subgrid of N_s points is given by

$$\begin{aligned}\underline{\nabla r}_{ave} &= \frac{1}{N_s} \sum_j \sum_k (F_{j,k} \underline{r}) \\ &= F \underline{r}\end{aligned}\tag{2.2-3}$$

where the summation extends over the subgrid and where

$$F = \frac{1}{N_s} \sum_j \sum_k F_{j,k}\tag{2.2-4}$$

The averaging process yields a more representative radiance gradient in the subgrid region. It follows that the radiance gradient error covariance matrix Γ , defined by

$$\Gamma = E \left\{ \underline{\tilde{\nabla r}}_{ave} \underline{\tilde{\nabla r}}_{ave}^T \right\}\tag{2.2-5}$$

where $\underline{\tilde{\nabla r}}_{ave}$ is the error in the computed gradient, can be written as

$$\Gamma = F \Phi F^T\tag{2.2-6}$$

where Φ denotes the radiance measurement error covariance matrix. The remainder of this section is hence devoted to the specification of Φ .

Under the reasonable assumptions that radiance measurement errors for one frequency are isotropic in space and possess an autocorrelation function that decays exponentially with horizontal distance, it follows that

$$E\left\{\tilde{r}_a \tilde{r}_b\right\} = \sigma^2 \exp\left(\frac{-d_{a,b}}{D}\right) \quad (2.2-7)$$

where

$$\tilde{r} = \hat{r} - r \quad (2.2-8)$$

the difference between measurement and truth, a and b refer to spatial locations, $d_{a,b}$ denotes the Euclidean distance between a and b, D is a correlation distance parameter and σ^2 is the instrument noise variance for the channel. For preliminary algorithm work, the parameter D is taken to be 300 km. Error standard deviations from Ref. 6 are listed in Table 2.2-1.

TABLE 2.2-1
HIRS/2 RADIANCE ERROR STANDARD DEVIATIONS

CHANNEL	CHANNEL WAVE NUMBER (cm^{-1})	ERROR STD. DEV. ($\text{mW/m}^2 \text{sr cm}^{-1}$)
1	669	3.00
2	680	0.67
3	690	0.50
4	703	0.31
5	716	0.21
6	733	0.24
7	749	0.20
8	900	0.10
13	2190	0.006
14	2210	0.003
15	2240	0.004
16	2270	0.002
17	2420	0.002
18	2515	0.002
19	2660	0.001

3.

ALGORITHM DEVELOPMENT

3.1 THE BASELINE ALGORITHM

The radiative transfer equation and the thermal wind equation are the key elements in the derivation of the baseline algorithm. The radiative transfer equation relates the radiance, R_i , measured by a satellite-borne radiometer at wave number ν_i , to the atmospheric temperature profile. The following simple form of the radiative transfer equation, based on a given temperature profile (e.g., from a forecast field), is derived in Ref. 4:

$$R_i = R_i^0 + \int_0^{z_T} K_i(z) T(x, y, z) dz \quad (3.1-1)$$

where,

x, y define zonal and meridional directions, respectively

R_i^0 is a constant

z_T defines the 'top of the atmosphere'

$K_i(z)$ is an approximately known weighting function at wave number ν_i (see Section 2.1)

$T(x, y, z)$ is the temperature profile at location (x, y)

z is the vertical coordinate defined by

$$z = \ln(p_0/p)$$

where p denotes pressure and p_0 denotes surface pressure.

Assuming that horizontal variations of K_i are negligible (following the treatment given in Ref. 4), the radiance gradient is determined from Eq. 3.1-1 as

$$\underline{\nabla R_i}(x, y) = \int_0^{z_T} K_i(z) \underline{\nabla T}(x, y, z) dz \quad (3.1-2)$$

Equation 3.1-2 represents a two-vector with x and y components

$$\frac{\partial R_i}{\partial x} = \int_0^{z_T} K_i(z) \frac{\partial T}{\partial x}(z) dz \quad (3.1-3)$$

$$\frac{\partial R_i}{\partial y} = \int_0^{z_T} K_i(z) \frac{\partial T}{\partial y}(z) dz \quad (3.1-4)$$

where the dependence on horizontal position has been suppressed.

The thermal wind equation relates the thermal wind, \underline{V}_T , i.e., the vector difference between geostrophic winds (\underline{V}_G) at two levels, to the horizontal temperature gradient

$$\underline{V}_T(z_l, z_u) = \underline{V}_G(z_u) - \underline{V}_G(z_l) = \frac{R}{f} \int_{z_l}^{z_u} (\underline{k} \times \underline{\nabla T}) dz \quad (3.1-5)$$

where

R is the gas constant

$f = 2\Omega \sin(\phi)$ is the Coriolis constant at latitude ϕ (Ω is the earth rotation rate)

\underline{k} is a unit vector in the vertical direction.

The horizontal gradient in this expression is within constant pressure surfaces as opposed to a fixed geometric altitude. As discussed in Ref. 4, however, the difference is assumed negligible in this effort. The scalar components of \underline{V}_T are given by

$$u_T(z_l, z_u) = u_G(z_u) - u_G(z_l) = -\frac{R}{f} \int_{z_l}^{z_u} \frac{\partial T}{\partial y} dz \quad (3.1-6)$$

$$v_T(z_l, z_u) = v_G(z_u) - v_G(z_l) = \frac{R}{f} \int_{z_l}^{z_u} \frac{\partial T}{\partial x} dz \quad (3.1-7)$$

where u and v denote the zonal and meridional components, respectively.

The possibility of estimating thermal wind directly from radiance data is suggested by the similarity between Eqs. 3.1-2 and 3.1-5. Both involve vertical integrals of the temperature gradient profile. However, the integral in Eq. 3.1-2 is over the entire atmosphere and is weighted by K_i , while that in Eq. 3.1-5 is unweighted and limited to the layer defined by (z_l, z_u) . In light of this, a function is defined

$$W(z) = \begin{cases} 1 & z_l \leq z \leq z_u \\ 0 & \text{otherwise} \end{cases} \quad (3.1-8)$$

For notational convenience the dependence on the interval (z_l, z_u) is suppressed throughout the remainder of the report. Equation 3.1-5 can now be written as

$$\underline{V}_T = \frac{R}{f} \int_0^{z_T} W(z) [\underline{k} \times \underline{\nabla T}] dz \quad (3.1-9)$$

The zonal and meridional scalar components are given respectively by

$$u_T = -\frac{R}{f} \int_0^{z_T} W(z) \frac{\partial T}{\partial y} dz \quad (3.1-10)$$

$$v_T = \frac{R}{f} \int_0^{z_T} W(z) \frac{\partial T}{\partial x} dz \quad (3.1-11)$$

Now, a linear estimator is defined using computed (that is, estimated) radiance gradients for available frequency channels

$$\hat{u}_T = -\frac{R}{f} \sum_i \frac{\partial \hat{R}_i}{\partial y} c_i \quad (3.1-12)$$

where the c_i are constants to be optimally determined. Henceforth, for simplicity, only the zonal component will be treated here. An analogous procedure for the meridional component is evident using radiance derivatives in the x direction. The computed radiance gradients consist of true plus error quantities (\sim denotes an error quantity)

$$\frac{\partial \hat{R}_i}{\partial y} = \frac{\partial R_i}{\partial y} + \frac{\partial \tilde{R}_i}{\partial y} \quad (3.1-13)$$

For convenience in the algebraic manipulations which follow, the radiance gradient terms and kernel functions for all available frequencies are organized into vectors, i.e.,

$$\underline{\hat{g}} = \begin{bmatrix} \frac{\partial \hat{R}_1}{\partial y} \\ \frac{\partial \hat{R}_2}{\partial y} \\ \vdots \\ \vdots \end{bmatrix} \quad \underline{\tilde{g}} = \begin{bmatrix} \frac{\partial \tilde{R}_1}{\partial y} \\ \frac{\partial \tilde{R}_2}{\partial y} \\ \vdots \\ \vdots \end{bmatrix} \quad \underline{K} = \begin{bmatrix} K_1 \\ K_2 \\ \vdots \\ \vdots \end{bmatrix} \quad (3.1-14)$$

Thus Eq. 3.1-12 is expressed in the form

$$\hat{u}_T = -\frac{R}{f} \underline{\hat{g}}^T \underline{c} \quad (3.1-15)$$

where

$$\underline{c} = \begin{bmatrix} c_1 \\ c_2 \\ \vdots \\ \vdots \end{bmatrix} \quad (3.1-16)$$

The statistical estimation problem consists of determining the coefficients \underline{c} to minimize the estimation error. For the zonal component this is given by the difference between Eqs. 3.1-15 and 3.1-10

$$\tilde{u}_T = -\frac{R}{f} \left[\underline{\hat{g}}^T \underline{c} - \int_0^{z_T} W(z) \frac{\partial T}{\partial y} dz \right] \quad (3.1-17)$$

Using Eqs. 3.1-4 and 3.1-13, Eq. 3.1-17 is expressed as

$$\tilde{u}_T = -\frac{R}{f} \left[\underline{\tilde{g}}^T \underline{c} - \int_0^{z_T} [W(z) - \underline{K}^T \underline{c}] \frac{\partial T}{\partial y} dz \right] \quad (3.1-18)$$

The statistical minimization criterion is represented by

$$J = E \{ \tilde{u}_T^2 \} \quad (3.1-19)$$

and is quadratic in \underline{c} . By differentiating Eq. 3.1-19 with respect to \underline{c} and setting the result equal to zero, the minimizing solution is found to be

$$\underline{c} = P^{-1} \underline{q} \quad (3.1-20)$$

where

$$P = \Gamma + \underline{\theta} \underline{\theta}^T \quad (3.1-21)$$

$$\underline{q} = \alpha \underline{\theta} \quad (3.1-22)$$

In Eq. 3.1-21, the Γ matrix represents the covariance of the radiance gradient errors as described in Section 2.2. The vector $\underline{\theta}$ and the scalar α involve the temperature gradient and the satellite weighting functions and are computed by the following numerical quadratures:

$$\underline{\theta} = \int_{z_l}^{z_T} \underline{K} \frac{\partial T}{\partial y} dz \doteq \frac{1}{2} \sum_{k=1}^{N_L-1} \left(\underline{K}(z_{k+1}) \frac{\partial T}{\partial y}(z_{k+1}) + \underline{K}(z_k) \frac{\partial T}{\partial y}(z_k) \right) (z_{k+1} - z_k) \quad (3.1-23)$$

$$\alpha = \int_{z_l}^{z_u} \frac{\partial T}{\partial y} dz \doteq \frac{1}{2} \sum_{k=1}^{u-1} \left(\frac{\partial T}{\partial y}(z_{k+1}) + \frac{\partial T}{\partial y}(z_k) \right) (z_{k+1} - z_k) \quad (3.1-24)$$

where N_L is the number of vertical levels and the symbol " \approx " denotes approximate equality. The root mean-square-error (rmse) in the thermal wind estimate is given by

$$\text{rmse} = \frac{R}{f} \left(a^2 - \underline{q}^T P^{-1} \underline{q} \right)^{\frac{1}{2}} \quad (3.1-25)$$

It is worth noting that the minimization criterion results in a biased thermal wind estimate. This is seen by taking the expected value of Eq. 3.1-18. The bias is found to be

$$(u_T)_B = \frac{R}{f} \int_0^{z_T} [W(z) - \underline{K}^T \underline{c}] \frac{\partial T}{\partial y} dz \quad (3.1-26)$$

Although an unbiased estimate could be determined, it would not be optimal in the sense of minimum mean-square-error.

3.2 ITERATIONS AND STEADY-STATE

Reference 4 suggested a method for extending the algorithm in Section 3.1. As a consequence of Eq. 3.1-6, it makes sense to update the guess of the temperature derivative profile by

$$\left(\frac{\partial T}{\partial y} \right)_{\text{new}}(z) = -\frac{f}{R} \frac{d}{dz_u} \hat{u}_T(z) \quad (3.2-1)$$

$$= \underline{\hat{g}}^T P^{-1} \underline{\theta} \left(\frac{\partial T}{\partial y} \right)_{\text{old}}(z) \quad (3.2-2)$$

where the second equality follows from Eqs. 3.1-15 and 3.1-20. The new guess of the temperature derivative profile could then, in turn, be used to compute a new thermal wind by

Eq. 3.1-12 and hence another update of the temperature derivative by Eq. 3.2-2. This iterative process could be carried out indefinitely, assuming it converges eventually to a physically meaningful function. The validity of this assumption has been the focal point of a thorough investigation of the iterative approach, of which only conclusions are reported here.

The setting defined in Section 3.1 (considering only the zonal wind component) is a special case of the setting defined in Ref. 4 (considering both zonal and meridional wind components simultaneously and minimizing a sum of squares criterion). For the sake of maximum generality, we discuss iterative investigation conclusions in the latter setting. To define circumstances under which the iterative procedure yields meaningful results requires changing the notation in Section 3.1 to fit the more general vector case. Equation 3.1-15 becomes

$$\hat{\underline{V}}_T = -\frac{R}{f} \hat{G} \underline{c} \quad (3.2-3)$$

where \hat{G} is a $2 \times n$ matrix of radiance gradient terms

$$\hat{G} = \begin{pmatrix} \frac{\partial R_1}{\partial y} & \frac{\partial R_2}{\partial y} & \dots \\ \frac{\partial R_1}{\partial x} & \frac{\partial R_2}{\partial x} & \dots \end{pmatrix} \quad (3.2-4)$$

and \underline{c} is given by Eq. 3.1-20, where

$$P = \Gamma + \Theta_i \Theta_i^T \quad (3.2-5)$$

$$\underline{q} = \Theta \underline{a} \quad (3.2-6)$$

and Θ and a are the matrix and vector generalizations, respectively of θ , a defined by Eqs. 3.1-23 and 3.1-24. The iteration given by Eq. 3.2-2 is now replaced by

$$\nabla \underline{L}_{i+1}(z) = \hat{G} P_i^{-1} \Theta_i \nabla \underline{L}_i(z) \quad (3.2-7)$$

where i is the iteration index.

Many approaches exist in the mathematical literature for determining conditions necessary and/or sufficient for a function sequence

$$\{\nabla \underline{L}_i(z)\}_{i=0}^{\infty} \quad (3.2-8)$$

to converge. In this case, the most promising approach involves looking not directly at the above function sequence, but instead at an associated $n \times n$ matrix sequence

$$\{X_i\}_{i=0}^{\infty} \quad (3.2-9)$$

where

$$X_i = \Theta_i \Theta_i^T \quad (3.2-10)$$

Note that each X_i has rank at most 2 since Θ_i is $n \times 2$. The advantages of a finite-dimensional linear algebraic formulation over an infinite-dimensional functional analytic formulation will become obvious as the discussion progresses. Since combining Eqs. 3.1-23 and 3.2-7 yields

$$\Theta_{i+1}^T = \hat{G} (\Gamma + \Theta_i \Theta_i^T)^{-1} \Theta_i \Theta_i^T, \quad (3.2-11)$$

it follows that

$$X_{i+1} = X_i (\Gamma + X_i)^{-1} \hat{G}^T \hat{G} (\Gamma + X_i)^{-1} X_i, \quad (3.2-12)$$

i.e., the matrix recursion involves no integrations. Note that if

$$\{\nabla T_i\} \xrightarrow{\text{uniformly}} \nabla T \quad (3.2-13)$$

then

$$X = \lim_{i \rightarrow \infty} X_i \quad (3.2-14)$$

exists, i.e., convergence of $\{X_i\}$ is necessary for uniform convergence of $\{\nabla T_i\}$; moreover, the limiting function ∇T must satisfy

$$\nabla T = \hat{G} (\Gamma + X)^{-1} X (\Gamma + X)^{-1} \hat{G}^T \nabla T \quad (3.2-15)$$

i.e., ∇T is a fixed point under the action of a certain 2×2 matrix based on X . In particular, the direction of ∇T is constant (with respect to z) unless

$$\hat{G} (\Gamma + X)^{-1} X (\Gamma + X)^{-1} \hat{G}^T = I \quad (3.2-16)$$

No analogous restrictions on the length of ∇T have yet been found (approximate schemes are under consideration). The importance of obtaining the limit X (in closed form, if possible) is nevertheless evident.

The following Theorem provides conditions sufficient for $\{X_i\}$ to converge.

Theorem Suppose that there exist n-vectors

$$\underline{a}, \underline{b}, \underline{u}, \underline{v}$$

and scalars

$$x_0 \geq 0, y_0 \geq 0$$

satisfying the two decomposability conditions

$$\begin{aligned}\hat{G}^T \hat{G} &= \underline{a} \underline{a}^T + \underline{b} \underline{b}^T \\ X_0 &= x_0 \underline{u} \underline{u}^T + y_0 \underline{v} \underline{v}^T\end{aligned}\tag{3.2-17}$$

and the two orthogonality conditions

$$\begin{aligned}\underline{v}^T \Gamma^{-1} \underline{u} &= 0 \\ a\delta + \beta\gamma &= 0\end{aligned}\tag{3.2-18}$$

where

$$\begin{aligned}a &= \underline{u}^T \Gamma^{-1} \underline{a} & \beta &= \underline{v}^T \Gamma^{-1} \underline{b} \\ \gamma &= \underline{u}^T \Gamma^{-1} \underline{b} & \delta &= \underline{v}^T \Gamma^{-1} \underline{a}\end{aligned}\tag{3.2-18}$$

Then

$$X = \lim_{i \rightarrow \infty} X_i$$

exists. Moreover, there exist $x \geq 0$ and $y \geq 0$ such that

$$X = x \underline{u} \underline{u}^T + y \underline{v} \underline{v}^T .$$

Explicit formulas can be written for x and y under each of four cases.

For convenience, let

$$\lambda = \underline{u}^T \Gamma^{-1} \underline{u}$$

$$\mu = \underline{v}^T \Gamma^{-1} \underline{v}$$

Formulas are written out for x in each case. Similar formulas for y are obtained by replacing a, γ, λ, x_0 by β, δ, μ, y_0 respectively in each expression.

Case i) If

$$0 < 4\lambda < a^2 + \gamma^2$$

and

$$a^2 + \gamma^2 - 2\lambda - \sqrt{a^2 + \gamma^2} \sqrt{a^2 + \gamma^2 - 4\lambda} < 2\lambda^2 x_0,$$

then

$$x = \frac{a^2 + \gamma^2 - 2\lambda + \sqrt{a^2 + \gamma^2} \sqrt{a^2 + \gamma^2 - 4\lambda}}{2\lambda^2}$$

Case ii) If

$$0 < 4\lambda < a^2 + \gamma^2$$

and

$$a^2 + \gamma^2 - 2\lambda - \sqrt{a^2 + \gamma^2} \sqrt{a^2 + \gamma^2 - 4\lambda} = 2\lambda^2 x_0,$$

then

$$x = x_0.$$

Case iii) If

$$0 < 4\lambda = a^2 + \gamma^2$$

and

$$a^2 + \gamma^2 - 2\lambda \leq 2\lambda^2 x_0,$$

then

$$x = \frac{a^2 + \gamma^2 - 2\lambda}{2\lambda^2}.$$

Case iv) Otherwise $x = 0$.

Thus one observes from the Theorem an "upper bound" on the covariance matrix Γ (in terms of the two quantities λ and μ) for which nonzero limits X exist. This upper bound may be thought of as a "reasonableness" bound, beyond which the iteration procedure converges to physically unrealistic profiles.

We wish to emphasize the importance of closed form solutions as presented in the Theorem statement. The iterative procedure for estimating temperature gradient profiles need not be iterative if such formulas are always applicable. The advantage of such formulas is that they would not be subject to possible slow convergence rates which have frequently occurred during computer experimentation using artificial inputs (and which might be hazardous and expensive if programmed into a wind profile estimation procedure).

4. SUPPORTING DATA FOR ALGORITHM DEMONSTRATION

The radiance data, rawinsonde data, and temperature field data described in this section have been acquired for purposes of algorithm evaluation and demonstration. No data processing results have been prepared for this interim report, but demonstration results will be featured in the final report due at the end of the contract period.

4.1 RADIANCE DATA

Radiance data from the High Resolution Infrared Radiation Sounder/2 (HIRS/2) of the NOAA-7 polar orbiting satellite has been obtained for algorithm demonstration purposes. The device is a part of the TIROS Operational Vertical Sounder (TOVS) instrument package and senses radiation in 20 channels in the infrared spectrum. The data set covers the region 10°W - 5°E and 30°N - 43°N (Western Europe and a small part of North Africa) as shown in Fig. 4.1-1; data for 4 March 1982 1300 UTC are included.

The radiance data obtained had been preprocessed to a 'Level 1-B' format. Data in this form are 1) quality controlled, 2) assembled into discrete data sets, and 3) uncalibrated and untransformed. Calibration coefficients and earth locations are included in the data set.

The data contains brightness temperatures which must be adjusted using band-correction coefficients and converted

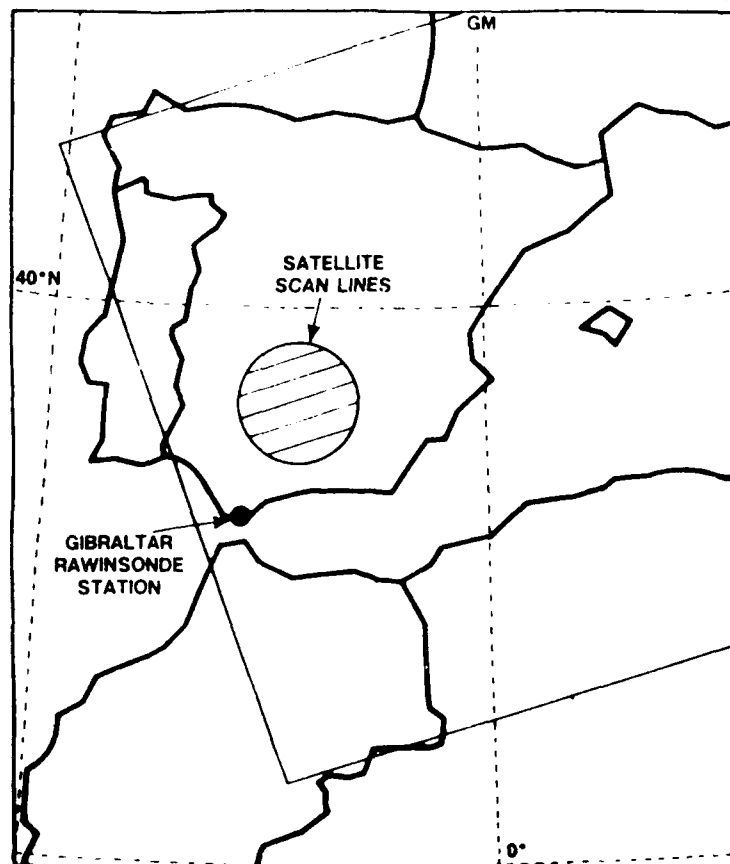


Figure 4.1-1 Coverage of Demonstration Radiance Data Set

to radiances. The required apparent brightness temperature, T^* , is given by

$$T^* = cT_c + b \quad (4.1-1)$$

where T_c is the band-corrected brightness temperature and b and c are coefficients dependent on the sensor and channel. Using T^* , a radiance is computed using the Planck Function (Eq. 2.1-2) at each channel frequency.

With a grid of radiance values established, radiance gradients at each grid point are computed using a bicubic

spline routine. (Routines from the IMSL library were used in this effort.) The grid, however, is aligned with the satellite scan (s) and track (t) directions. The desired gradients in zonal and meridional directions are given respectively by

$$\frac{\partial R}{\partial x} = \frac{\partial R}{\partial t} \frac{\partial t}{\partial x} + \frac{\partial R}{\partial s} \frac{\partial s}{\partial x} \quad (4.1-2a)$$

$$\frac{\partial R}{\partial y} = \frac{\partial R}{\partial t} \frac{\partial t}{\partial y} + \frac{\partial R}{\partial s} \frac{\partial s}{\partial y} \quad (4.1-2b)$$

with

$$\frac{\partial t}{\partial x} = \frac{\partial t}{\partial \psi} \frac{\partial \psi}{\partial x} \quad (4.1-3a)$$

$$\frac{\partial t}{\partial y} = \frac{\partial t}{\partial \phi} \frac{\partial \phi}{\partial y} \quad (4.1-3b)$$

$$\frac{\partial s}{\partial x} = \frac{\partial s}{\partial \psi} \frac{\partial \psi}{\partial x} \quad (4.1-3c)$$

$$\frac{\partial s}{\partial y} = \frac{\partial s}{\partial \phi} \frac{\partial \phi}{\partial y} \quad (4.1-3d)$$

where ψ , ϕ are earth longitude and latitude (in radians) respectively, and, under the assumption of a spherical earth,

$$\frac{\partial \psi}{\partial x} = \frac{1}{R_e \cos \phi} \quad (4.1-4a)$$

$$\frac{\partial \phi}{\partial y} = \frac{1}{R_e} \quad (4.1-4b)$$

where R_e is the radius of the earth in kilometers. The satellite track/scan geometry relative to earth is such that ana-

lytic expressions for the derivatives $\partial t/\partial \psi$, $\partial t/\partial \phi$, $\partial s/\partial \psi$, and $\partial s/\partial \phi$ do not exist. However, earth latitude and longitude for every radiance data point is included in the data set. Therefore these derivatives were computed numerically using finite differences.

Finally, to compute $\partial R/\partial t$ and $\partial R/\partial s$, the radiance data were fit to a surface using a cubic spline routine. The derivatives were evaluated from this surface at every grid point.

4.2 RAWINSONDE DATA

Rawinsonde observation (RAOB) data were ordered from the National Climatic Data Center (NCDC) to provide 'truth' data for comparison with estimation results. Data from several RAOB sites on or near the Iberian Peninsula, an area covered by the radiance data, were ordered. However, for 4 March 1982 1200 UTC (the synoptic time nearly coincident with the collection of the radiance data) upper air data for only one station, Gibraltar (08495) were available. This finding was both disappointing and puzzling since Ref. 7 presents maps of thickness values at various pressure intervals for these Iberian sites.

The Gibraltar u and v wind component profiles are shown in Fig. 4.2-1. A northwesterly flow from 1000 mb to 500 mb is indicated. Above this layer, the flow weakens, and winds become light and variable in direction.

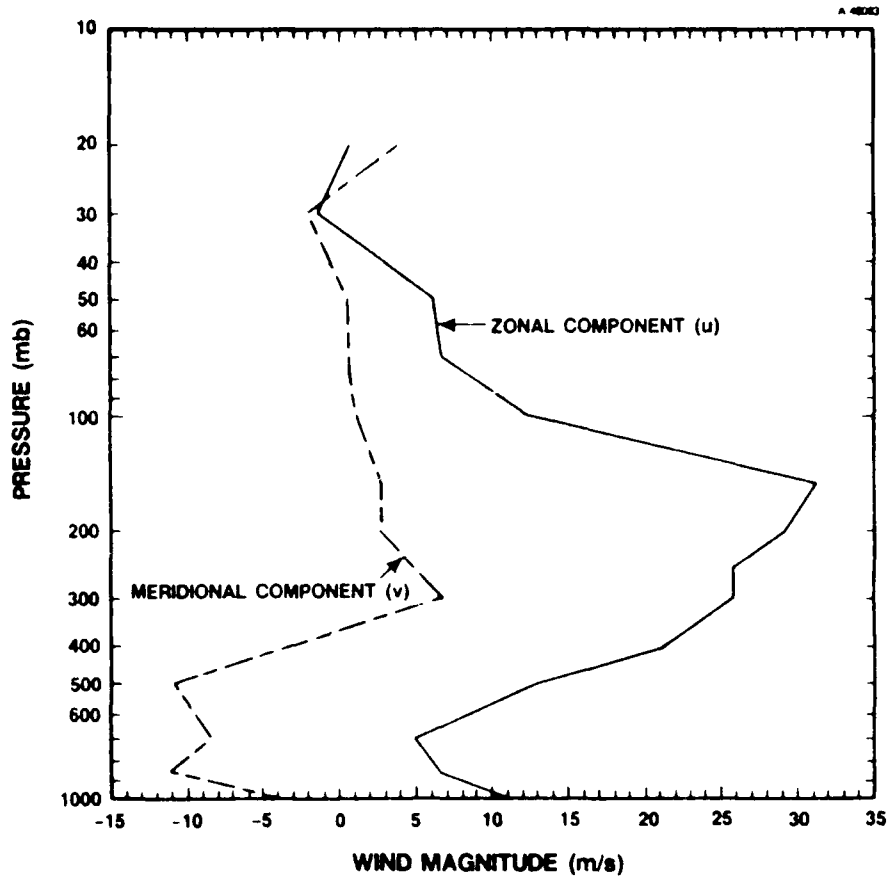


Figure 4.2-1 Gibraltar Rawinsonde Wind Data

4.3 TEMPERATURE FIELD DATA

Paper copies of 850, 700, 500, 300, 200 and 100 mb National Meteorological Center (NMC) height contour and temperature analyses were ordered from NCDC for 4 March 1982 1200 UTC. Wind speed analyses replaced temperature analyses for the 300 and 200 mb levels. Therefore, these temperature fields were subjectively analyzed over the area of interest. Temperatures were interpolated to a one degree by one degree grid for display and gradient calculation purposes. Figures 4.3-1 through 4.3-4 show the 850, 500, 200, and 100 mb temperature analyses.

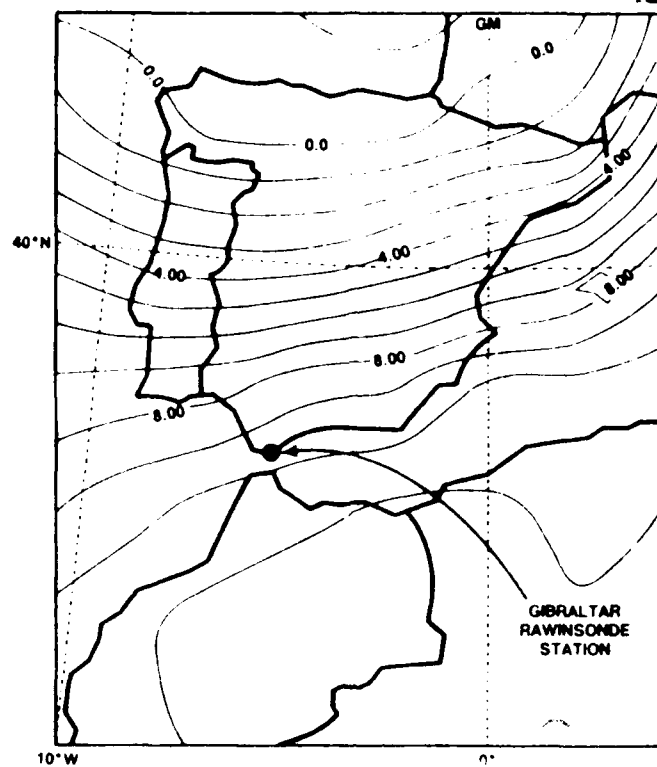


Figure 4.3-1 NMC Temperature Analysis (850 mb) (°C)

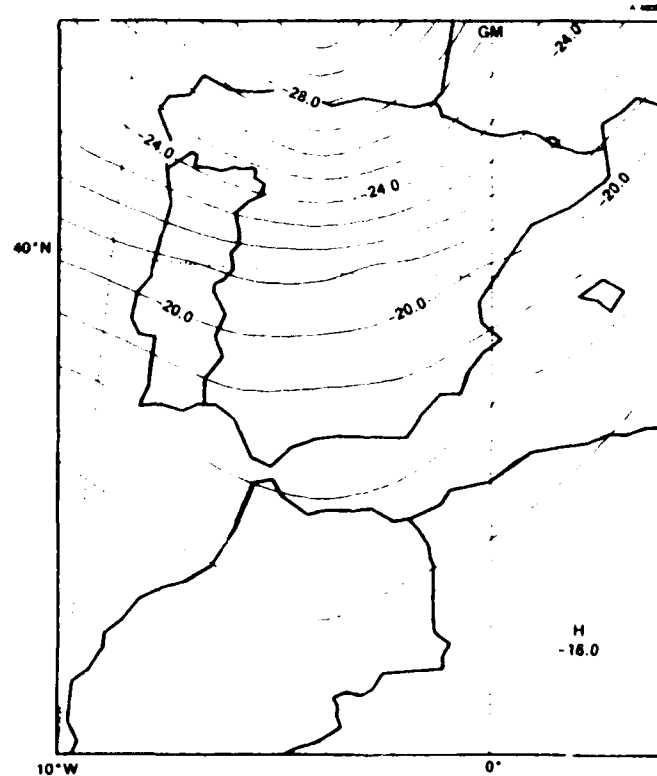


Figure 4.3-2 NMC Temperature Analysis (500 mb) (°C)

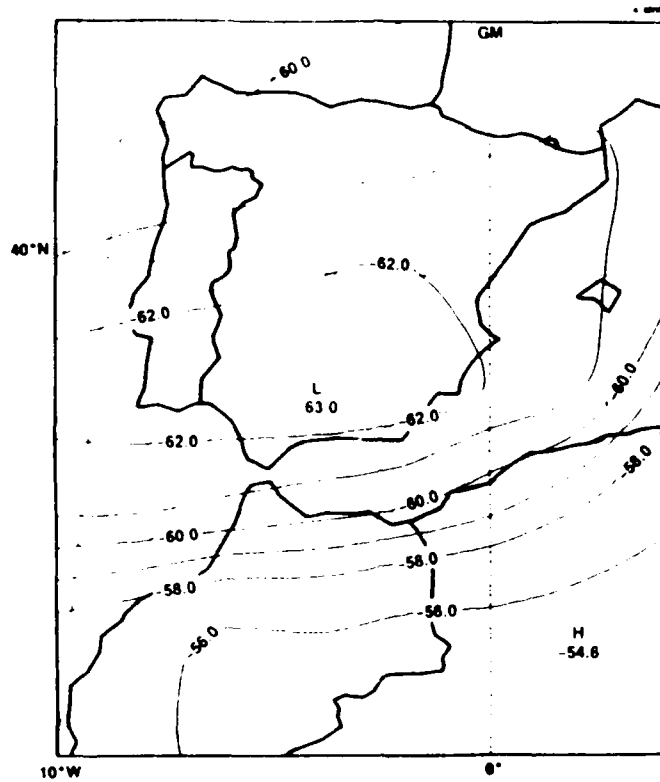


Figure 4.3-3 NMC Temperature Analysis (200 mb) (°C)

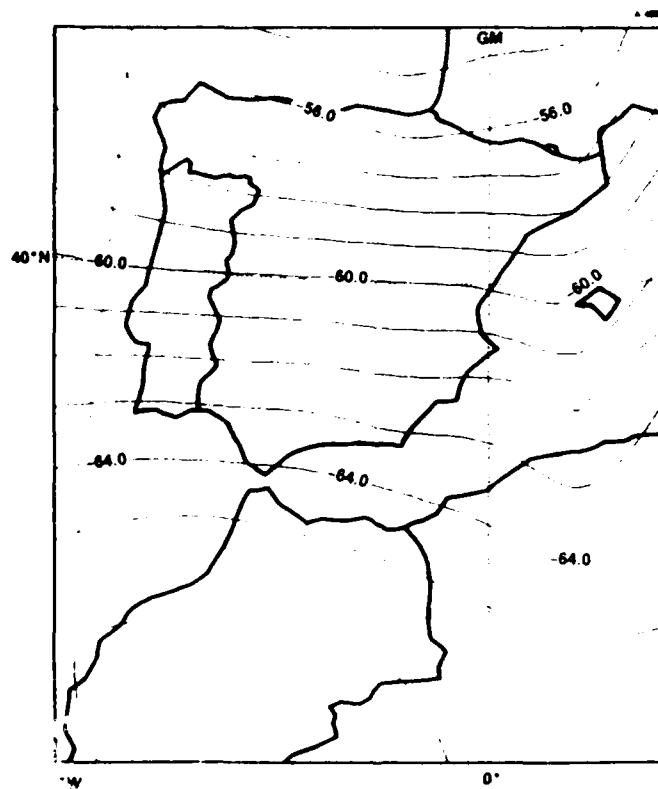


Figure 4.3-4 NMC Temperature Analysis (100 mb) (°C)

The 850 mb temperature analysis (Fig. 4.3-1) indicates a strong temperature gradient oriented north-south over the Iberian Peninsula. The isotherm pattern corresponds to a "dry" cold front oriented northeast to southwest. The 500 mb isotherms (Fig. 4.3-2) indicate a strong gradient over the northern half of Spain; the gradient weakens southward. At 200 mb (Fig. 4.3-3), an interesting temperature pattern develops. A cold area is noted near Gibraltar with a weak temperature gradient to the north and strong gradient over Morocco and Algeria. Finally, the 100 mb isotherm pattern (Fig. 4.3-4) reveals a reversal in the direction of the gradient with cold air to the south and warmer air to the north. This pattern is expected due to the increasingly higher level of the tropopause with decreasing latitude. These analyses along with the 700 and 300 mb analyses (not shown) are used to compute temperature gradients near and around Gibraltar.

BASELINE SIMULATION RESULTS

For purposes of algorithm and software verification, simulation results have been generated using the baseline algorithm (Section 3.1). The objective here is to analytically compute radiance gradients from a simple, prescribed temperature field and the satellite weighting function models, exercise the algorithm with these simulated data, and compare the computed thermal wind estimates with the 'true' values computed directly from the thermal wind equation. The simulation procedure for the zonal wind component is detailed below, followed by simulation results.

For simplicity, but with no loss in generality, the temperature field is prescribed with a horizontal gradient which does not vary with altitude. That is,

$$T(y, z) = \beta y + \gamma z \quad (5-1)$$

where

$$\beta = \overline{\frac{\partial T}{\partial y}} = \text{CONSTANT} \quad (5-2)$$

The overbar emphasizes the constancy of the derivative. The zonal thermal wind for the layer (z_l, z_u) is computed from Eq. 3.1-6 as

$$u_T = \frac{-R}{f} \overline{\frac{\partial T}{\partial y}} \Delta z \quad (5-3)$$

where

$$\Delta z = z_u - z_l \quad (5-4)$$

This u_T represents the true value for comparison with simulation results.

Radiance gradients are computed from the prescribed temperature field and the satellite weighting functions (which depend on the vertical temperature profile) using Eq. 3.1-4. The computation is simplified as a result of the vertically constant temperature gradient. At each relevant wave number,

$$\frac{\partial R_i}{\partial y} = \frac{\partial T}{\partial y} \int_0^{z_T} K_i dz \quad (5-5)$$

Since the K_i are represented as analytic forms (see Section 2.1), an IMSL routine (DCADRE) readily computes the integrals to a specified accuracy. The computed gradients at selected frequencies, along with the prescribed temperature information, are the inputs to the baseline algorithm.

To show that the baseline algorithm will produce the correct wind estimate in the absence of noise and numerical error (due to using the trapezoid rule), let

$$\underline{L} = \begin{bmatrix} \int_0^{z_T} K_1 dz \\ \int_0^{z_T} K_2 dz \\ \vdots \\ \vdots \\ \vdots \end{bmatrix} \quad \underline{g} = \begin{bmatrix} \frac{\partial R_1}{\partial y} \\ \frac{\partial R_2}{\partial y} \\ \vdots \\ \vdots \\ \vdots \end{bmatrix} \quad (5-6)$$

and use Eq. 5-5 to get

$$\underline{g} = \frac{\partial \overline{T}}{\partial y} \underline{L} \quad (5-7)$$

The zonal thermal wind estimate is given by (see Eq. 3.1-15)

$$\dot{u}_T = \frac{-R}{f} \underline{g}^T \underline{c} \quad (5-8)$$

where, following the treatment of Section 3.1,

$$\underline{c} = P^{-1} \underline{q} \quad (5-9)$$

$$P = \Gamma + \underline{\theta} \underline{\theta}^T \quad (5-10)$$

$$\underline{q} = a \underline{\theta} \quad (5-11)$$

and, for this case,

$$\underline{\theta} = \frac{\partial \overline{T}}{\partial y} \underline{L} \quad (5-12)$$

$$a = \frac{\partial \overline{T}}{\partial y} \Delta z \quad (5-13)$$

Using Eqs. 5-7, 5-8, 5-9 and 5-12, the thermal wind estimate for vanishing radiance gradient errors becomes

$$\lim_{\Gamma \rightarrow 0} \{\dot{u}_T\} = \lim_{\Gamma \rightarrow 0} \left\{ \frac{-R}{f} \underline{\theta}^T P^{-1} \underline{q} \right\} \quad (5-14)$$

Applying the Sherman-Morrison formula (Ref. 9) to Eq. 5-10, P^{-1} is given by

$$P^{-1} = \Gamma^{-1} - \left(\frac{1}{1 + \underline{\theta}^T \Gamma^{-1} \underline{\theta}} \right) \Gamma^{-1} \underline{\theta} \underline{\theta}^T \Gamma^{-1} \quad (5-15)$$

Now Eq 5-14 can be expressed as

$$\begin{aligned} \lim_{\Gamma \rightarrow 0} \{\dot{u}_T\} &= \\ \lim_{\Gamma \rightarrow 0} \left\{ \frac{-R}{f} \underline{\theta}^T \left[\Gamma^{-1} - \left(\frac{1}{1 + \underline{\theta}^T \Gamma^{-1} \underline{\theta}} \right) \Gamma^{-1} \underline{\theta} \underline{\theta}^T \Gamma^{-1} \right] a \underline{\theta} \right\} &\quad (5-16) \end{aligned}$$

which becomes

$$\lim_{\Gamma \rightarrow 0} \{\dot{u}_T\} = \lim_{\Gamma \rightarrow 0} \left\{ \frac{-R}{f} \left(1 - \frac{\underline{\theta}^T \Gamma^{-1} \underline{\theta}}{1 + \underline{\theta}^T \Gamma^{-1} \underline{\theta}} \right) a \underline{\theta}^T \Gamma^{-1} \underline{\theta} \right\} \quad (5-17)$$

$$= \lim_{\Gamma \rightarrow 0} \left\{ \frac{-R}{f} \left(\frac{a}{1 + \underline{\theta}^T \Gamma^{-1} \underline{\theta}} \right) \underline{\theta}^T \Gamma^{-1} \underline{\theta} \right\} \quad (5-18)$$

$$= \frac{-R}{f} a = \frac{-R}{f} \frac{\partial \bar{T}}{\partial y} \Delta z = u_T \quad (5-19)$$

Thus the thermal wind estimate \dot{u}_T approaches the true value u_T as the radiance gradient error covariance matrix approaches zero. This result not only provides theoretical justification for the baseline algorithm but also enables a check for vertical discretization and numerical integration errors.

Using a vertically constant meridional temperature gradient of -0.0065 deg K/km and estimating the zonal thermal wind for the layer 850-700 mb, simulation results have been generated and are summarized in Table 5-1. It is clearly shown that as the radiance gradient error covariance matrix, Γ , approaches zero, the estimates approach the correct value, as dictated by the theoretic treatment above. Since radiance gradient errors are the only random errors presently modeled in the baseline algorithm, the estimate root-mean-square-error also vanishes as Γ decreases.

The simulation procedure not only serves to verify the algorithm and implementation, but also provides a useful tool for sensitivity studies. For example, estimate and estimate error sensitivities to the following quantities can be determined

- Radiance measurement error model parameter
- Radiance gradient errors
- Satellite weighting functions

TABLE 5-1
BASELINE ALGORITHM SIMULATION RESULTS

	ZONAL WIND, u_T (m/s)	ROOT-MEAN-SQUARE-ERROR (m/s)
TRUE VALUE	3.5	—
BASELINE RADIANCE GRADIENT ERROR MODEL, Γ	2.5	1.6
$\Gamma/10$	3.3	0.7
$\Gamma/100$	3.4	0.2

-
- Temperature errors
 - Temperature gradient errors
 - Channels selected

Further work in this area will assist in error model development, particularly for the satellite weighting functions and temperature and temperature gradient errors.

The simulation results are encouraging, but in processing actual radiance data the wind estimates may deviate from observed values for the following reasons

- nonzero radiance gradient estimation (i.e., calculation) errors
- inexact satellite weighting functions
- differences between true winds and geostrophic winds
- observation errors
- temperature and temperature gradient errors

Demonstration results using the data sets described in Section 4, among others, will be presented in the final report.

SUMMARY

An optimal thermal wind estimation procedure directly utilizing frequency-dependent spatial radiance gradients has been described herein. The procedure is optimal with respect to the models developed for radiance gradient errors and satellite kernel functions. A nominal temperature profile and temperature gradient profile, to be provided operationally from a forecast, are key elements of the procedure. This interim report presents both a baseline formulation and an extension of that approach based on iteratively updating the temperature data along with the thermal wind estimates.

The baseline algorithm and software was verified using simulated radiance gradients. Simulation results were shown to be consistent with baseline algorithm theoretical calculations. Actual HIRS/2 radiance data, described herein, will be used for algorithm demonstration later in the contract period, and results presented in a final report.

REFERENCES

1. Ohring, G., et. al., "Direct Determination of Wind Shears from the Gradients of Satellite Radiance Observations," Journal of Applied Meteorology, v. 20, November 1981, pp. 1336-1343.
2. Fleming, H.E., "Determination of Vertical Wind Shear from Linear Combinations of Satellite Radiance Gradients: A Theoretical Study," Technical Report NPS63-79-4, Naval Postgraduate School, September 1979.
3. Panofsky, H.A., et. al., "Estimation of Vertical Wind Shear from Infrared and Microwave Radiances," Final Report CR 82-01, Department of Meteorology, The Pennsylvania State University, January 1982.
4. "Proposal for a Statistical Wind Profile Estimation Procedure," The Analytic Sciences Corporation, Technical Proposal TP-7055, January 1987.
5. Weinreb, M.P., "Atmospheric Transmission for Remote Temperature Sounding," SPIE Vol. 195, 1979.
6. "Comparison of the Defense Meteorological Satellite Program (DMSP) and the NOAA Polar-Orbiting Operational Environmental Satellite (POES) Program," ENVIROSAT-2000 Report, NESDIS, National Oceanic and Atmospheric Administration, Washington, D.C.
7. Smith, W.L., et. al., "The Physical Retrieval TOVS Export Package," The Technical Proceedings of the First International TOVS Study Conference, March 1984, pp. 227-278.
8. deBoor, Carl, A Practical Guide to Splines, Springer-Verlag, N.Y. 1978.
9. Golub, G.H. and Van Loan, C.F., Matrix Computations, The Johns Hopkins University Press, Baltimore, MD, 1983.

APPENDIX A-1
TRANSFORMING RADIANCE MEASUREMENTS INTO RADIANCE GRADIENTS

The objective of this appendix is to find a $2 \times N_x \times N_y$ matrix, $F_{j,k}$, such that the radiance gradient at grid point (j,k) can be obtained by multiplying the vector \underline{r} of all radiance measurements over the grid (as defined by Eq. 2.2-2) by $F_{j,k}$. This form is useful in developing the radiance gradient error model.

Figure A-1 illustrates an N_x by N_y radiance grid with horizontal separation distance parameters Δx and Δy . The partial derivative of radiance r at point (j,k) with respect to x is calculated using r values along the j^{th} row of the grid; the partial derivative of r with respect to y is calculated using r values along the k^{th} column of the grid. The cubic spline routine passes a set of cubics through the radiance values of either row or column, using a new cubic in each subinterval. In order for both the slope and the curvature to be the same for the pair of cubics that join at each point, the following equations must be satisfied for $i = 2, 3, \dots, N_x - 1$ (see Ref. 8)

$$-\Delta x \left(\frac{\partial r_{j,i-1}}{\partial x} + 4 \frac{\partial r_{j,i}}{\partial x} + \frac{\partial r_{j,i+1}}{\partial x} \right) = 3r_{j,i-1} - 3r_{j,i+1} \quad (\text{A-1})$$

and, for $i = 2, 3, \dots, N_y - 1$:

$$-\Delta y \left(\frac{\partial r_{i-1,k}}{\partial y} + 4 \frac{\partial r_{i,k}}{\partial y} + \frac{\partial r_{i+1,k}}{\partial y} \right) = 3r_{i-1,k} - 3r_{i+1,k} \quad (\text{A-2})$$

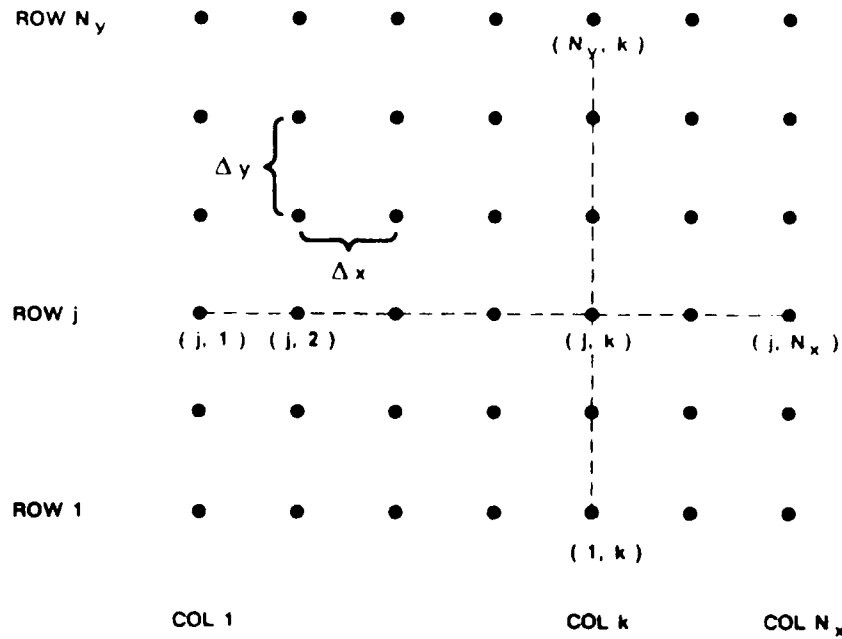


Figure A-1 Radiance Grid

Boundary conditions (known as "not-a-knot" conditions) are given by:

$$-\Delta x \left(2 \frac{\partial r_{j,1}}{\partial x} + 4 \frac{\partial r_{j,2}}{\partial x} \right) = 5r_{j,1} - 4r_{j,2} - r_{j,3} \quad (\text{A-3})$$

$$-\Delta x \left(4 \frac{\partial r_{j,N_x-1}}{\partial x} + 2 \frac{\partial r_{j,N_x}}{\partial x} \right) = r_{j,N_x-2} + 4r_{j,N_x-1} - 5r_{j,N_x} \quad (\text{A-4})$$

$$-\Delta y \left(2 \frac{\partial r_{1,k}}{\partial y} + 4 \frac{\partial r_{2,k}}{\partial y} \right) = 5r_{1,k} - 4r_{2,k} - r_{3,k} \quad (\text{A-5})$$

$$-\Delta y \left(4 \frac{\partial r_{N_y-1,k}}{\partial y} + 2 \frac{\partial r_{N_y,k}}{\partial y} \right) = r_{N_y-2,k} + 4r_{N_y-1,k} - 5r_{N_y,k} \quad (\text{A-6})$$

Equations A-1 through A-6 permit calculation of the transformation matrix $F_{j,k}$. Define N_x by N_x matrices Q_x and P_x as the coefficient matrices of the left hand sides and right hand sides, respectively of Eqs. A-1, A-3, and A-4. Equivalently,

$$-\Delta x Q_x \begin{pmatrix} \frac{\partial r_{j,1}}{\partial x} \\ \vdots \\ \frac{\partial r_{j,N_x}}{\partial x} \end{pmatrix} = P_x \begin{pmatrix} r_{j,1} \\ \vdots \\ r_{j,N_x} \end{pmatrix} \quad (A-7)$$

For instance, if $N_x = 7$, then

$$Q_x = \begin{pmatrix} 2 & 4 & 0 & 0 & 0 & 0 & 0 \\ 1 & 4 & 1 & 0 & 0 & 0 & 0 \\ 0 & 1 & 4 & 1 & 0 & 0 & 0 \\ 0 & 0 & 1 & 4 & 1 & 0 & 0 \\ 0 & 0 & 0 & 1 & 4 & 1 & 0 \\ 0 & 0 & 0 & 0 & 1 & 4 & 1 \\ 0 & 0 & 0 & 0 & 0 & 4 & 2 \end{pmatrix} \quad (A-8)$$

$$P_x = \begin{pmatrix} 5 & -4 & -1 & 0 & 0 & 0 & 0 \\ 3 & 0 & -3 & 0 & 0 & 0 & 0 \\ 0 & 3 & 0 & -3 & 0 & 0 & 0 \\ 0 & 0 & 3 & 0 & -3 & 0 & 0 \\ 0 & 0 & 0 & 3 & 0 & -3 & 0 \\ 0 & 0 & 0 & 0 & 3 & 0 & -3 \\ 0 & 0 & 0 & 0 & 1 & 4 & -5 \end{pmatrix} \quad (A-9)$$

The boundary conditions are captured in the first and last rows of Q_x and P_x , with the remaining conditions occurring in-between. Define N_y by N_y matrices Q_y and P_y similarly. Then, if

$$\underline{v}^T = j^{\text{th}} \text{ row of } \frac{-1}{\Delta x} Q_x^{-1} P_x \quad (\text{A-10})$$

$$\underline{w}^T = k^{\text{th}} \text{ row of } \frac{-1}{\Delta y} Q_y^{-1} P_y \quad (\text{A-11})$$

it follows that

$$\begin{pmatrix} \frac{\partial r_{j,k}}{\partial x} \\ \frac{\partial r_{j,k}}{\partial y} \end{pmatrix} = \begin{pmatrix} \underline{v}^T & \underline{0}^T \\ \underline{0}^T & \underline{w}^T \end{pmatrix} \begin{pmatrix} r_{j,1} \\ r_{j,2} \\ \vdots \\ r_{j,N_x} \\ r_{1,k} \\ r_{2,k} \\ \vdots \\ r_{N_y,k} \end{pmatrix} \quad (\text{A-12})$$

The final step consists of defining an $(N_x + N_y)$ by $(N_x * N_y)$ matrix $H_{j,k}$ such that

$$\begin{pmatrix} r_{j,1} \\ r_{j,2} \\ \vdots \\ r_{j,N_x} \\ r_{1,k} \\ r_{2,k} \\ \vdots \\ r_{N_y,k} \end{pmatrix} = H_{j,k} \underline{r} \quad (\text{A-13})$$

It can be easily shown that

$$H_{j,k} = \begin{pmatrix} \underline{e}_{(j-1)N_x+1}^T \\ \vdots \\ \underline{e}_{jN_x}^T \\ \underline{e}_k^T \\ \vdots \\ \underline{e}_{(N_y-1)N_x+k}^T \end{pmatrix} \quad (A-14)$$

where \underline{e}_i denotes the i^{th} unit vector in $(N_x * N_y)$ dimensional space. Hence

$$F_{j,k} = \begin{pmatrix} \underline{v}^T & \underline{0}^T \\ \underline{0}^T & \underline{w}^T \end{pmatrix} H_{j,k} \quad (A-15)$$

is the desired transformation matrix and

$$\underline{\nabla} \underline{r}_{j,k} = F_{j,k} \underline{r} \quad (A-16)$$

as was to be shown.

REFERENCES

1. Ohring, G., Neeman, B., and Duncan, L.D., *Direct Determination of Wind Shears from the Gradients of Satellite Radiance Observations*, Journal of Applied Meteorology, v. 20, November 1981, pp. 1336-1343.
2. *Proposal for a Statistical Wind Profile Estimation Procedure*, The Analytic Sciences Corporation, **Technical Proposal TP-7055**, January 1987.
3. Golub, G.H., and Van Loan, C.F., *Matrix Computations*, The Johns Hopkins University Press, Baltimore, MD, 1983.